

NASA/TM-2011-214528



# Cavity Heating Experiments Supporting Shuttle Columbia Accident Investigation

*Joel L. Everhart, Karen T. Berger, Kim S. Bey, N. Ronald Merski, and William A. Wood  
Langley Research Center, Hampton, Virginia*

---

March 2011

## NASA STI Program . . . in Profile

Since its founding, NASA has been dedicated to the advancement of aeronautics and space science. The NASA scientific and technical information (STI) program plays a key part in helping NASA maintain this important role.

The NASA STI program operates under the auspices of the Agency Chief Information Officer. It collects, organizes, provides for archiving, and disseminates NASA's STI. The NASA STI program provides access to the NASA Aeronautics and Space Database and its public interface, the NASA Technical Report Server, thus providing one of the largest collections of aeronautical and space science STI in the world. Results are published in both non-NASA channels and by NASA in the NASA STI Report Series, which includes the following report types:

- **TECHNICAL PUBLICATION.** Reports of completed research or a major significant phase of research that present the results of NASA programs and include extensive data or theoretical analysis. Includes compilations of significant scientific and technical data and information deemed to be of continuing reference value. NASA counterpart of peer-reviewed formal professional papers, but having less stringent limitations on manuscript length and extent of graphic presentations.
- **TECHNICAL MEMORANDUM.** Scientific and technical findings that are preliminary or of specialized interest, e.g., quick release reports, working papers, and bibliographies that contain minimal annotation. Does not contain extensive analysis.
- **CONTRACTOR REPORT.** Scientific and technical findings by NASA-sponsored contractors and grantees.
- **CONFERENCE PUBLICATION.** Collected papers from scientific and technical conferences, symposia, seminars, or other meetings sponsored or co-sponsored by NASA.
- **SPECIAL PUBLICATION.** Scientific, technical, or historical information from NASA programs, projects, and missions, often concerned with subjects having substantial public interest.
- **TECHNICAL TRANSLATION.** English-language translations of foreign scientific and technical material pertinent to NASA's mission.

Specialized services also include creating custom thesauri, building customized databases, and organizing and publishing research results.

For more information about the NASA STI program, see the following:

- Access the NASA STI program home page at <http://www.sti.nasa.gov>
- E-mail your question via the Internet to [help@sti.nasa.gov](mailto:help@sti.nasa.gov)
- Fax your question to the NASA STI Help Desk at 443-757-5803
- Phone the NASA STI Help Desk at 443-757-5802
- Write to:  
NASA STI Help Desk  
NASA Center for AeroSpace Information  
7115 Standard Drive  
Hanover, MD 21076-1320

NASA/TM-2011-214528



# Cavity Heating Experiments Supporting Shuttle Columbia Accident Investigation

*Joel L. Everhart, Karen T. Berger, Kim S. Bey, N. Ronald Merski, and William A. Wood  
Langley Research Center, Hampton, Virginia*

National Aeronautics and  
Space Administration

Langley Research Center  
Hampton, Virginia 23681-2199

March 2011

## Acknowledgments

The authors gratefully acknowledge the contributions of the following individuals to this research effort: Buddy Stotler, Grace Gleason, Roland Hatten, Kevin Hollingsworth, and Teck-Seng Kwa for operation of the 20-Inch Mach 6 Air Tunnel and data acquisition support; Gary Wainwright and Steve Nevins for model CAD design and fabrication of the stereolithography models; Michael Powers, Mark Griffith, Hayward C. Glaspell for fabrication of the ceramic test models; Ed Covington, Kathryn Kuykendoll, and Pete Veneris for model fidelity measurements and fiducial mark placement; and, Gregory M. Buck for the model oil flow visualization runs.

The use of trademarks or names of manufacturers in this report is for accurate reporting and does not constitute an official endorsement, either expressed or implied, of such products or manufacturers by the National Aeronautics and Space Administration.

Available from:

NASA Center for AeroSpace Information  
7115 Standard Drive  
Hanover, MD 21076-1320  
443-757-5802

# TABLE OF CONTENTS

	<b>PAGE</b>
List of Tables .....	6
List of Figures .....	7
Abstract .....	9
Introduction .....	10
Nomenclature .....	12
Approach .....	13
Supersonic/Hypersonic Cavity Flow Physics .....	14
Flight-to-Tunnel Scaling Methodology .....	15
Experimental Methods .....	16
Test Facility .....	17
Test Model Description .....	18
Oil Flow Visualization Technique .....	19
Phosphor Thermography Technique .....	19
Experimental Results .....	20
Oil Flow Visualization .....	20
Surface Heating Data .....	22
Phosphor Uncertainty Analysis .....	26
Summary .....	28
References .....	30
Tables .....	37
Figures .....	52
Appendix: Derivation of Pressure Gradient Surface Geometry .....	104

## LIST OF TABLES

	<b>PAGE</b>
TABLE 1.- Flight Scaled Cavities and Conditions.....	37
TABLE 2.- Nominal flow conditions in the 20-Inch Mach 6 Air Tunnel. ....	37
TABLE 3.- Cavity models for Test 6857 - Columbia accident investigation.....	38
TABLE 4.- Cavity models for Test 6868 - Closed cavity geometry parameters.....	39
TABLE 5.- Test matrix for Test 6857 - Oil flow runs. ....	40
TABLE 6.- Test matrix for Test 6857 - Baseline model heating runs. ....	41
TABLE 7.- Test matrix for Test 6857 - Cavity heating runs. ....	42
TABLE 8.- Test matrix for Test 6868 – Baseline model heating runs.....	46
TABLE 9.- Test matrix for Test 6868 - Cavity heating runs. ....	47
TABLE 10.- Test matrix for Test 6868 - Pressure gradient effects on heating using SLA models.....	50
TABLE 11.- Test matrix for Test 6868 - Cross-flow effect on heating using SLA models. ....	51
TABLE 12.- Phosphor uncertainty estimates.....	51

## LIST OF FIGURES

	<b>PAGE</b>
Figure 1.- Combined experimental and computational simulation approach.....	52
Figure 2.- Classification of supersonic/hypersonic cavity flows.....	52
Figure 3.- Sketch of model coordinate system. ....	53
Figure 4.- LAURA predictions for $M_e$ versus $a$ for baseline model. ....	53
Figure 5.- LAURA predictions for $Re_\theta$ versus $a$ for baseline model. ....	54
Figure 6.- LAURA predictions for boundary layer thickness for baseline model.....	54
Figure 7.- Langley 20-Inch Mach 6 Air Tunnel.....	55
Figure 8.- Baseline model - 4-in. by 6-in. inserts used in Test 6857. ....	55
Figure 9.- Baseline model - 4-in. by 18-in. inserts used in Test 6868. ....	55
Figure 10.- Model fabrication process. ....	56
Figure 11. – Cavity insert photographs for Test 6857 .....	57
Figure 12. – Cavity insert model photographs for Test 6868.....	61
Figure 13.- Oil flow images for Test 6857.....	68
Figure 14.- Oil flow visualization of cavity width effect - $L/H=14$ , $H/\delta=1.1$ . ....	70
Figure 15.- Baseline heating runs for Test 6857. ....	71
Figure 16.- Open flow cavity heating runs for Test 6857.....	73
Figure 17.- Cavity alignment effect on open flow cavity heating for Test 6857. ....	79
Figure 18.- Closed flow cavity heating runs for Test 6857.....	81
Figure 19.- Baseline heating runs for Test 6868. ....	88
Figure 20.- Open (short) cavity heating runs for Test 6868.....	90
Figure 21.- Length effect on closed cavity heating for Test 6868 – $Re_\theta=300$ , $H/\delta=1.1$ .....	91
Figure 22.- Length effect on closed cavity heating for Test 6868 – $Re_\theta=300$ , $H/\delta=2.39$ .....	93
Figure 23.- Length effect on closed cavity heating for Test 6868 – $Re_\theta=500$ , $H/\delta=1.1$ .....	94
Figure 24.- Length effect on closed cavity heating for Test 6868 – $Re_\theta=500$ , $H/\delta=2.39$ .....	95

Figure 25.- Depth effect on closed cavity heating for Test 6868 – Re <sub>θ</sub> =503, H/δ=2.39.....	96
Figure 26.- Depth effect on closed cavity heating for Test 6868 – Re <sub>θ</sub> =503, H/δ=5.20.....	98
Figure 27.- Depth effect on closed cavity heating for Test 6868 – Re <sub>θ</sub> =260, H/δ=0.65.....	99
Figure 28.- Depth effect on closed cavity heating for Test 6868 – Re <sub>θ</sub> =260, H/δ=2.7.....	100
Figure 29.- Pressure gradient effect on closed cavities for Test 6868.....	101
Figure 30.- Cross flow effect on closed cavities for Test 6868 – Re <sub>θ</sub> =300, H/δ=1.1.....	102
Figure 31.- Cross flow effect on closed cavities for Test 6868 – Re <sub>θ</sub> =500, H/δ=2.39.....	103



## Abstract

*The two-color thermographic phosphor method has been used to map the local heating augmentation of scaled idealized cavities at conditions simulating the windward surface of the Shuttle Orbiter Columbia during flight STS-107. Two experiments initiated in support of the Columbia Accident Investigation were conducted in the Langley 20-Inch Mach 6 Tunnel. Generally, the first test series evaluated open (length-to-depth less than 10) rectangular cavity geometries proposed as possible damage scenarios resulting from foam and ice impact during launch at several discrete locations on the vehicle windward surface, though some closed (length-to-depth greater than 13) geometries were briefly examined. The second test series was designed to parametrically evaluate heating augmentation in closed rectangular cavities. The tests were conducted under laminar cavity entry conditions over a range of local boundary layer edge-flow parameters typical of re-entry. Cavity design parameters were developed using laminar computational predictions, while the experimental boundary layer state conditions were inferred from the heating measurements. An analysis of the aeroheating caused by cavities allowed exclusion of non-breaching damage from the possible loss scenarios being considered during the investigation.*

# Introduction

On February 1, 2003 the Space Shuttle Columbia, flight STS-107, was lost during re-entry. Many possible damage scenarios were examined during the ensuing accident investigation, among them the creation of impact-induced cavities in the tile thermal protection system (TPS), resulting in local augmentation of the heating and eventual burn through of the aluminum substructure. The purpose of this report is to document two wind tunnel cavity heating experiments conducted in the NASA Langley 20-Inch Mach 6 Wind Tunnel to support the Columbia Accident Investigation Board (CAIB) and to present foundational cavity heating information supporting the follow-on Return-to-Flight (RTF) program established to implement CAIB recommendations. This document will outline the adopted testing approach and the flight-to-tunnel scaling philosophy. Data presented herein are in image format; accordingly, only qualitative observations are made concerning their behavior.

Defining the heating environment of a damage-scenario cavity presents a significant challenge – how is the cavity defined? Particularly when few (if any) direct measurements of the cavity geometry are available and when the exact location of the cavity (implying local flow conditions) may be unknown. Many possible variables and parameters exist. The gross geometric parameter space includes: length (L), width (W), and depth (H), and planform, cross-sectional, and profile variations. Sidewall and upstream endwall entry angles may play an important role on the flow expansion into the cavity, while sidewall and endwall exit angles may affect recompression on the downstream wall and further expansion around the end-wall corner – all parameters having a direct influence on the heating. The depth distribution along the cavity profile may potentially affect how or if the flow enters the cavity and impinges on the floor. The impact of roughness caused by irregular surfaces, protuberances, gap fillers between tiles (present or missing), embedded objects, etc. is unknown, but the roughness may significantly impact the shear layer/boundary layer transition process. Local boundary layer edge-flow conditions include Mach number ( $M_e$ ), momentum thickness Reynolds number ( $Re_\theta$ ), boundary layer thickness ( $\delta$ ), stream direction with respect to the cavity major axis, chemistry effects reflected in the ratio of specific heats ( $\gamma$ ), wall temperature ratio ( $T_w/T_{aw}$ ), and boundary layer state (laminar, transitional, or turbulent) entering and leaving the cavity.

The supersonic/hypersonic cavity flow literature (particularly that for laminar test conditions), while helpful, is particularly sparse on both the local and downstream effects of many fundamental flow parameters. Fletcher, et al. published the survey paper “A Review of Heat Transfer in Separated and Reattached Flows” in 1970. Nestler updated this survey with more recent work in 1985 in “The Effects of Surface Discontinuities on Convective Heat Transfer in Hypersonic Flow.” Together, these papers include much of the existing, pertinent cavity flow literature. They cited theoretical models of

cavity flow developed by Burggraf (1965), Chapman (1956), Carlson (1959), Chang (1966), and Lamb (1967); however, none of the theories adequately capture the physics of laminar and turbulent three-dimensional cavity flows as will be demonstrated via global surface heating distributions presented herein, though they offer a framework for experimental studies. Numerical studies were conducted by Adams (1974), Morgens-tern and Chokani (1994), and Zhang, et al. (2001). More recently, additional numerical studies have been added for the CAIB and the Shuttle RTF program by Wood, et al. (2004) and Pulsonetti, et al. (2005). Experimentally, laminar two-dimensional flows were addressed by Galenter (1975) and Nestler (1966); laminar axisymmetric flows were addressed by Nestler (1970), Nicoll (1963, 1964), and Wyborny, et al. (1967); and, laminar three-dimensional flows were examined by Cheatwood, et al. (2001), Hahn (1969), and Nestler (1981). Experimental studies with cavities tested in transitional boundary layers or to determine the onset of transition were presented by Charbonnier and Boerrigter (1993), Boerrigter and Charbonnier (1996), Hollis and Liechty (2002, 2006), Larson and Keating (1960), Liechty, et al. (2006a), and Rhudy and Magnan (1964). Turbulent two-dimensional experiments were presented by Charwat, et al. (1961a, 1961b), Chin and Seban (1972), Emery (1969), Hunt (1977), Lamb (1968, 1980a, 1980b), Nestler (1968, 1969, 1970a, 1970b), Shchukin, et al. (1980), and Stallings and Wilcox (1987); turbulent axisymmetric experiments were conducted by Hunt (1974) and Netterfield (1989); and turbulent three-dimensional experiments were published by Wilcox (1990, 1991). In general, the heating measurements were obtained with sparsely spaced discrete sensors, the exception being those global phosphor thermography measurements presented by Cheatwood, et al., and Hollis and Liechty for circular cavities. Because of this spatial measurement sparseness, much of the three-dimensional nature of the surface heating profile is missed, as is in many cases the important peak heating value. While most of the idealized cavity geometries are rectangular with a flat bottom profile (a few have an arc bottom), the paper by Emery is of particular significance because heating profiles are presented for models with notched, cutback profile geometries that may be more representative of potential impact damage conditions. Two papers by Blair and Stallings (1986) and Stallings, et al. (1991) are significant because they present oil flow visualizations in and around the cavity and vapor screen visualizations of the cavity crossflow plane, clearly showing the growth and development of the cavity vortex structure. Similar, limited oil flow results for the current experiments will be presented herein. The important class of cavities known as gaps (i.e., cavities with length-to-depth ratio less than 1) has been examined by Coats, et al. (1970), Johnson (1973), Throckmorton (1974), and Weinstein, et al. (1975). In-gap heating measurements were not acquired during the current experiments, though a limited number of runs were made with gaps extending downstream of the cavity to simulate the loss of gap fillers to evaluate their impact on the cavity heating levels.

As discussed above, there exists only a limited amount of laminar flow experimental data for evaluating heating effects in supersonic/hypersonic cavities. Additionally, most of the existing parametric variations and correlations have been developed using turbulent heating measurements. Accordingly, turbulent methods have typically been

used for thermal assessments of damage on the Space Shuttle, even though much of the re-entry trajectory provides laminar edge conditions on the vehicle. The use of these turbulent methods may be overly conservative. An objective of these experiments is to develop a cavity-heating database with laminar entry and exit conditions that will, hopefully, provide an additional thermal assessment capability for possible damage scenarios. Because of the unknowns existing in the flow physics, a fundamental question is whether the cavity flow definitions presented in the literature are even valid for the hypersonic laminar cavity. An objective of these experiments is to provide information to enable an assessment of this question. Finally, computational modeling of chemically reacting hypersonic flows is difficult; for potential damage scenarios it becomes extremely challenging to separate the flow physics effects, and then validate the solution. A further objective of these experiments is to provide parametric information to reduce the risks associated with numerical simulations.

## Nomenclature

$B$	<i>bias uncertainty</i>
$BF$	<i>Bump Factor</i>
$BF_{max}$	<i>maximum Bump Factor on the cavity end wall</i>
$C_p$	<i>pressure coefficient</i>
$c$	<i>specific heat (BTU/lbm-°F)</i>
CAIB	<i>Columbia Accident Investigation Board</i>
$h$	<i>heat transfer coefficient, <math>h=q/(H_{aw}-H_w)</math>, (lbm/ft<sup>2</sup>/s)</i>
$H$	<i>enthalpy (btu/lbm)</i>
$H, W, L$	<i>cavity depth, width, length (in)</i>
$k$	<i>thermal conductivity (BTU/hr-ft-°F)</i>
$M$	<i>Mach number</i>
$P$	<i>precision uncertainty</i>
$p$	<i>pressure (psi)</i>
$Re$	<i>Reynolds number per foot (1/ft)</i>
$Re_\theta$	<i>momentum thickness Reynolds number</i>
RTF	<i>Return-to-Flight</i>
$T$	<i>temperature (°R)</i>
$t$	<i>time (s)</i>
TGP	<i>thermographic phosphor</i>
TPS	<i>thermal protection system</i>
$x$	<i>axial distance from nose of model (in)</i>
$y$	<i>spanwise distance from centerline of model (in)</i>
$z$	<i>distance normal to model surface (in)</i>
$\alpha$	<i>angle-of-attack, nose up is positive (deg)</i>
$\beta$	<i>thermal product, <math>(\rho ck)^{1/2}</math></i>
$\gamma$	<i>ratio of specific heats</i>

$\delta$	<i>boundary layer thickness</i>
$\Theta$	<i>Normalized temperature in heating equation</i>
$\theta$	<i>boundary layer momentum thickness (in)</i>
$\rho$	<i>density (lbm/ft<sup>3</sup>)</i>
$\Lambda$	<i>Normalized time in heating equation</i>
$\lambda$	<i>cavity rotation angle (deg)</i>

### **Subscripts**

$\infty$	<i>freestream conditions</i>
<i>avg</i>	<i>average</i>
<i>aw</i>	<i>adiabatic wall conditions</i>
<i>e</i>	<i>boundary layer edge conditions</i>
<i>FR</i>	<i>conditions from Fay-Riddell calculation for a hemisphere</i>
<i>init</i>	<i>initial</i>
<i>ref</i>	<i>reference condition</i>
<i>t1</i>	<i>reservoir conditions</i>
<i>w</i>	<i>wall conditions</i>

## **Approach**

The combined computational and experimental approach taken for this program is presented in Figure 1. Since fluid physics and flow chemistry dominated the hypersonic accident environment, full computational simulation using even a simplified Orbiter geometry is difficult because of uncertainties inherent in viscous flow phenomena (i.e. separation, transition, shock-boundary layer interactions, etc.). High-temperature chemical interactions that define aerothermodynamics further compound the simulation process, particularly when structural combustion may be occurring. Issues such as actual damage site geometry and location, and computational grid resolution and convergence introduce a multitude of other uncertainties. Ground-based facilities are incapable of replicating the required energy levels with full geometric and fluid dynamic simulation. However, they can be used to conduct building block experiments wherein the fluid phenomena are simulated on simplified, scaled geometries. These experiments may then be used to develop an empirical understanding, ultimately leading to mathematical relationships and correlations for modeling the heating augmentation produced by a possible damage scenario, and they may also be used to assess and improve the ability of computer codes to suitably capture the flow physics. An assessment of flow chemistry effects can be made after validation of the flow physics model, which lends credence to flight scenario computations.

# Supersonic/Hypersonic Cavity Flow Physics

Based on the literature survey, the following overview of cavity flow physics is presented. Length-to-depth ratio ( $L/H$ ) is typically used to distinguish between and classify different cavity flow regimes, as depicted in Figure 2. Very short or deep cavities with  $L/H < 1$  are known as gaps. In this case, shearing induced by the main stream flow causes the development within the gap of a column of counter-rotating vortices numbering approximately  $H/L$ . Alternating hot spots are developed in the gap when the vortices directionally align and impinge on the sidewall.

Two stable flow conditions exist for cavities with length  $L/H > 1$ . The first is a *short cavity* in the length range  $1 \leq L/H \leq 10$ , known as an *open cavity* in the literature. The mainstream flow does not enter the cavity directly, though there may be some mass interchange with the low-energy vortical flow inside the cavity. Physically, the short cavity has insufficient length to support the required entry and exit turning angles, therefore it skims the cavity. In this case, the pressure in the cavity is typically above the ambient and climbs to a peak at the downstream lip. The heating drops to values significantly below the undisturbed value and rises slowly to a peak value on the downstream lip. The other stable solution is a *long cavity*, also known as a *closed cavity*, with length  $L/H \geq 14$ . In this case, three distinct flows may develop if the cavity is long enough. First, the upstream flow is now able to turn into the cavity and impinge on the floor, creating an aft-facing-step flow field. Next, a boundary layer on the floor may develop and recover to the ambient level outside the cavity. Finally, as the flow approaches the end wall it will turn outward and create a forward-facing-step flow field. For long, deep cavities, the pressure gradients may be severe where the flow turns and strong expansion and shock waves will be generated. Viscous shearing generated by this flow turning will augment the heating to levels significantly higher than the ambient levels on both the cavity floor and the end wall. The pressure in these long cavities will decrease below the ambient and steadily increase downstream, reaching large values of over-pressure behind the shocks. Vortices will develop on the cavity sidewalls as the flow expands around the corner into the cavity and on the floor after flow impingement, further augmenting the heating, which may extend laterally around the cavity in the most severe cases. These vortices will interact with the cavity end wall and spill into the downstream region beyond the cavity. Given laminar inflow, analysis of the heating profiles indicates that most any type of outflow may occur, depending on the cavity and its environmental state. The in-cavity flow may remain laminar, become transitional, or transition to fully turbulent flow; the downstream possibilities are equally varied and are currently the subject of extensive analysis and testing (Liechty 2006a) in support of Shuttle RTF.

Cavities in the range  $10 \leq L/H \leq 14$  are typically unsteady as the flow alternates between the two bounding conditions; these are known as transitional cavities. Oil flow visualization of both open and closed conditions occurring in the same cavity has been presented by Stallings, et. al. (1991). Transitional cavities are avoided where possible in

the present tests because of the complexity of the required instrumentation and test time necessary to address flow steadiness.

The boundaries between the different cavity flow regimes are nominal, at best. For example, different researchers have measured  $L/H$  values ranging from 9 to 11 as the upper limit for open cavities and from 12 to 15 as the lower limit for closed cavity flow. These limits should therefore be taken only as a guide. Also, it is important to note that most of the reported cavity data were acquired in air ( $\gamma=1.4$ ) with some in helium ( $\gamma=1.67$ ). Since turning angle is a function of both Mach number and  $\gamma$ , it is conceivable that the open/closed cavity boundaries will vary during re-entry as vehicle boundary layer edge conditions change. At present, experimental data are insufficient to estimate the strength of this effect on the aeroheating. At the time of these experiments, the effects of pressure gradient on the local heating had not been addressed in the published literature. Some indication regarding this effect can be found in a recent paper by Everhart, et. al. (2006).

## Flight-To-Tunnel Scaling Methodology

The procedure adopted for scaling a cavity from the flight environment to the wind tunnel is straightforward. Based on the literature survey, the cavity geometry is defined by its length ( $L$ ), width ( $W$ ), depth ( $H$ ), and orientation ( $\lambda$ ), while the pertinent flow conditions are the boundary layer edge conditions at the cavity entrance, i.e. the Mach number ( $M_e$ ), momentum thickness Reynolds number ( $Re_\theta$ ), boundary layer thickness ( $\delta$ ), wall temperature ratio ( $T_w/T_{aw}$ ), and the gas chemistry effects reflected in the ratio of specific heats ( $\gamma$ ). In flight, the cavity parameter space is given by  $(M_e, Re_\theta, T_w/T_{aw}, \gamma, H/\delta, W/H, L/H, \lambda)_{\text{FLIGHT}}$ . Similarly, in the wind tunnel the cavity parameter space is given by  $(M_e, Re_\theta, T_w/T_{aw}, \gamma, H/\delta, W/H, L/H, \lambda)_{\text{Tunnel}}$ . The challenge becomes one of matching the parameter spaces. The flight chemistry is difficult to match in a conventional wind tunnel, as is the wall temperature ratio. So, for modeling the effects of fluid physics these two parameters are excluded from the experiments, relying on future computational fluid simulations for their assessment, leaving

$$(M_e, Re_\theta, H/\delta, W/H, L/H, \lambda)_{\text{FLIGHT}} = (M_e, Re_\theta, H/\delta, W/H, L/H, \lambda)_{\text{Tunnel}}$$

The accident investigation team prescribed two original candidate damage geometries (length by width by depth) as a missing carrier panel of 24x4x3 inches and missing/damaged tiles 18x6x2.5 inches (equivalent to 3 tiles) near the Main Landing Gear Door. The boundary layer edge conditions for the shuttle-accident flight environment were computationally determined at different possible damage sites by Pulsonetti and Thompson (2004). The flight scaling and conditions at these prescribed locations are presented in Table 1. As presented in the table, the largest variations occur in the values of  $Re_\theta$  and  $H/\delta$  with the  $M_e$  and  $L/H$  variations remaining relatively small. Fur-

thermore, since the values of  $L/H$  correspond to those in the open-cavity flow regime, the effect of this parameter on the heating was expected to be small. The local influence of  $W/H$  was unknown. The procedure for matching these conditions in the wind tunnel is as follows. First, computational solutions of the boundary layer flow on a flat plate baseline model were determined by Wood, et al. (2004) using the LAURA Navier-Stokes code (Gnoffo 1990). Referring to the model sketch provided in Figure 3 for the coordinate system, the resulting variations of  $M_e$ ,  $Re_\theta$ , and  $\delta$  as a function of plate incidence,  $\alpha$ , for several freestream Reynolds numbers for several locations along the plate are presented in Figures 4 through 6. To design the test environment, including test conditions and cavity geometry, the model angle of attack was set to yield the prescribed  $M_e$ , which was approximately constant along the plate at a given a setting. Next, the position on the plate yielding the required  $Re_\theta$  was determined from the boundary layer solution. Plate boundary layer thickness ( $\delta$ ) at this position was then used as a multiplier on the flight scaling of  $(H/\delta)$  to determine the required depth of the cavity,  $H_{\text{Tunnel}}$ , to be installed on the wind tunnel model. The model-scaled cavity length and width follow by multiplying  $(W/H)_{\text{Flight}}$  and  $(L/H)_{\text{Flight}}$  by  $H_{\text{Tunnel}}$ , respectively. It is important to note that each resulting cavity represents a point design for the selected conditions because the plate boundary layer changes as the tunnel test conditions change. As seen in Table 1, the parameter variation is limited; therefore, a family of models was designed for Test 6857 to allow a limited parametric variation about the prescribed damage geometry. All of the prescribed cases are for open cavity flow conditions, so additional models were used during Test 6868 to address the heating issues related to closed cavity flows.

## Experimental Methods

This section presents the experimental methods and apparatus, beginning with a description and operational characteristics of the wind tunnel facility. This is followed with a detailed discussion of the baseplate model, the fabrication process used for the 50 different cavity model inserts, a model geometry description, and photographic documentation. Next, an overview is given of the fluorescent oil flow technique. This qualitative measurement method combined with heating measurements on the baseplate is used to qualify the testing environment. Finally, the phosphor thermography method used to provide global heating measurements of the cavity flow field is presented.



## Test Facility

The 20-Inch Mach 6 Air Tunnel (Fig. 7) is a blowdown facility in which heated, dried and filtered air is used as the test gas. It has a two-dimensional, contoured nozzle, which opens into a 20.5-in. by 20-in. test section, and it is equipped with a bottom-mounted injection system that can transfer a model from the sheltered model box to the tunnel centerline in less than 0.5 seconds. Run times of up to 15 minutes are possible in this facility, although for the current aeroheating study run times of only a few seconds were required. The nominal reservoir conditions of this facility are stagnation pressures of 30 psi to 500 psi with stagnation temperatures of 760°R to 1000°R, which very nearly produce perfect gas ( $\gamma = 1.4$ ) freestream flows with Mach numbers between 5.8 and 6.1 and Reynolds numbers of  $0.5 \times 10^6/\text{ft}$  to  $7.3 \times 10^6/\text{ft}$ . The nominal flow conditions in this facility can be seen in Table 2. Micol (1995) presented a more detailed description of this facility.

## Test Model Description

The baseline model used for this study (Figs. 8 and 9) was a strut-mounted, rectangular 10-inch wide by 28-inch long flat plate. The model is also shown in Figure 7 below the tunnel in the model injection box. Two different nose geometries were available, including a sharp leading edge and a blunted leading edge with a radius of 0.125 inches. Model station 0 was measured in all cases from the origin of the sharp nose configuration. The blunt nose model was used in all cases because it resulted in edge Mach numbers of approximately 2.9 at zero incidence as required to match the test conditions. Test article surface conditions on the model centerline were determined using the LAURA code. Test articles were inserted into a 4-inch wide by 18-inch long test bay beginning at station 7.5 inches downstream of the nose. During Test 6857 (T6857), the first entry, three 4-in. by 6-in. solid surface test articles were used to create the baseline surface (see Fig. 8), following the original design specifications. Installation, alignment, steps, and gap sealing issues were resolved (though not quite as well as desired) with 0.003-inch thick kapton tape as shown in Figure 8. The test process was greatly improved during Test 6868 (T6868) where a single-piece model insert of dimension 4-in. by 18-in. was used (see Fig. 9). The model was equipped with surface pressure orifices; however, these were sealed from the backside to prevent leakage and disturbance tripping of the boundary layer. Additionally, there exists a provision for installation of boundary layer trips near the leading edge. This can be seen as a rectangular insert paralleling the leading edge in Figure 9

Fabrication of the ceramic cavity models was a significant task, initially requiring a total of 50 different geometries to be developed. However, since model testing was performed concurrently with model manufacturing, many of the early designs used in T6857 were deemed unnecessary and were not built, though multiple copies of several

configurations were developed to address specific testing and fluid dynamic effects issues. Buck (2005) presented a detailed description of the cavity-model fabrication process. The first step in the process was developing the model geometry definition as required by the test conditions (recall that each model is a point design). Coordinates for these models were electronically transferred to the rapid-prototyping facility where an appropriate CAD model description was developed. Stereolithographic Array process (SLA) resin models (Fig. 10a) were then fabricated as patterns used for the casting of the silica ceramic insert models. An aluminum backing plate (Fig. 10b) was bonded to backside of each ceramic insert for mounting in the flat plate model. Models used to perform the oil flow investigations were the SLA patterns painted with a black high-temperature paint to enhance photographic contrast (Fig. 10c). This figure shows geometry details of the backside of the model without the aluminum backing plate. The ceramic models were spray coated with a mixture of phosphors suspended in a silica-based colloidal binder (Fig. 10d). Fiducial marks were next applied to the model surface at critical reference locations, such as the corners of the cavity on both the floor and the surrounding edges, and on the plate surface around the cavity. They can be seen as small, circular marks and they are used to aid in data reduction and model orientation. Erroneous heating measurements are realized at a fiducial mark because the inking process changes the calibration of the phosphor. Therefore, results at these locations should be excluded from all measurements. The locations of these marks can be seen in Fig. 10d. The fiducial marks used in T6857 were laboriously applied by hand because of time constraints imposed by the wide-ranging demands of the accident investigation on the Quality Assurance Laboratory; accordingly, the locations are not as precise and cleanly defined as normally desired. Subsequently, in the T6868 investigations when more time was available the fiducial marks were applied by the normal method using the direct computer controlled (DCC) coordinate measuring machine (CMM). The geometry description of each cavity model built for T6857 is presented in Table 3 and photographs of the painted SLA model insert and a close-up photograph of the ceramic cavity are presented in Figure 11. Similarly, T6868 models are presented in Table 4 and Figure 12.

Two special case models of Configuration 3 were built, namely 3-Gap and 3-Gouge (see Fig. 11). Gap fillers are shim material placed between the shuttle tiles for thermal and vibration isolation. Loss of the gap fillers can allow pressure relief in the cavity, leading to a change in the heating. Configuration 3-Gap was designed to assess this change by cutting spanwise and longitudinal 0.0143-inch wide by 0.536-inch deep gaps on each side of the cavity on the downstream end. The scaled width  $G/H=0.0267$  is similar to that on the Orbiter. Configuration 3-Gouge was a fortuitous mistake during fabrication that occurred when the mold improperly released during casting, providing a more realistic impact-damage geometry.

## Oil Flow Visualization Technique

A new in-situ fluorescent oil flow technique developed at Langley Research Center (Buck, Pulsonetti, and Weilmeunster, 2005) was used to qualify the model surface flow and examine several of the cavities prior to initiating the heating measurements. Before each run, the model surface was cleaned and two coats of oil were applied. The first coat was a heavy weight oil used to reduce the surface tension; the second was a sprayed coating of a light weight oil that caused oil beads to form. Finally, the green fluorescent powder was sprinkled over the oil. During the run, an ultraviolet bandpass filtered mercury arc lamp (365 nanometers wavelength) was used to excite the fluorescent powder, which emits a visible light pattern. The emitted brightness is a function of the powder density, therefore accumulations of the powder on oil beads and along separation lines and other such features are particularly visible. The oil flow was then recorded during the run using a digital video camera. Post-run digital pictures of the run were also recorded.

## Phosphor Thermography Technique

Global surface heating distributions were calculated using the two-color relative-intensity, phosphor-thermography aeroheating measurement method (Merski 1999). This is the standard method for obtaining aeroheating data in NASA Langley's hypersonic wind tunnels, and it can be used to identify the surface heating effects of complex three-dimensional flow phenomena, which are difficult to examine using conventional discrete-sensor methods. With this method, ceramic wind tunnel models are coated with phosphor crystals that fluoresce in the red and green regions of the visible light spectrum when illuminated by ultraviolet (UV) light. During a wind tunnel run, the phosphor-coated model is exposed to the heated flow of the tunnel, and the resulting changes in fluorescence intensity of the model are recorded and digitized through a 640 by 480 resolution color CCD (charge coupled device) camera and a state-of-the-art video acquisition system. The fluorescence intensity is dependent on both the intensity of the incident UV light and the local model surface temperature. The UV dependence is removed by taking the ratio of the green to red intensity images, from which surface temperature distributions are determined through prior calibrations. Images are acquired before the wind tunnel run and after injection of the model to the tunnel centerline during a run. Data are acquired, reduced and analyzed using the IHEAT code (Merski 1999) and may be mapped onto a 3-dimensional CAD representation of the test article using the MAP3D code (Merski 1999). During the current experiments, phosphor Batch 9 was used for T6857, while an improved lower-temperature formulation denoted phosphor Batch 10 was used for T6868. Results are presented herein in terms of a non-dimensional heat transfer coefficient ratio,  $h/h_{FR}$ , where  $h_{FR}$  is the theoretical heating computed with the Fay-Riddell (1958) method for a 0.025-in. radius sphere, which is the radius of the nose of the test models, at 540°R

## Experimental Results

This section includes a discussion of the measurements acquired for both T6857 and T6868. Only image data will be presented; hence, only qualitative statements are made concerning their behavior. All required digital data have been transferred electronically to the Entry Aerothermodynamics Damage Assessment Team at Johnson Space Center. First presented are observations from oil flow visualizations used to assess the surface flow over the base model and around select cavity configurations. Next, global surface heating distributions acquired using phosphor thermography are introduced. Base plate heating combined with the oil flow visualizations allows general statements regarding the state of the cavity entry conditions. Future analysis will allow assessment of the exit conditions. Heating measurements acquired during geometry screening studies of various parameters when combined with the oil flow visualizations allows generalized statements regarding the importance of the parameter variation prior to establishing an extensive testing program.

### Oil Flow Visualization

Test conditions for the oil flow visualizations conducted in T6857 are presented in Table 5 and the corresponding post-run images are presented in Figure 13. In all cases, flow is from left to right. The base plate surface flow is characterized in Runs 13-18 for a series of angles of attack and stream Reynolds numbers covering the anticipated test envelope. The side vortices caused by finite-plate width effects that are emanating from the plate leading edge are particularly evident in runs 17 and 18. The bounding track of these disturbances indicates that flow between is predominantly two-dimensional down the plate length. Run 17 is particularly revealing in that the Kapton tape sealing upstream pressure orifices has lifted at its corners, generating two vortices that track straight downstream through the test region with little divergence until the aft end of the model, as desired. This run and, also, the nonuniform flow shown in Run 16 highlight the required care that must be exercised with this model in the tape-sealing process at each joint to ensure clean undisturbed flow over the test region.

Oil flow visualizations for several of the cavity geometries are presented in Figure 13 for Runs 19-27. Run 19 is a deep cavity of  $L/H=8$  and  $H/\delta=1.76$ , while Run 23 is a medium-depth cavity of  $L/H=7.2$  and  $H/\delta=1.1$ . In both of these cases, the movement of the oil on the floor is almost non-existent, indicating open cavity flow. Downstream of each cavity endwall, the flow wipes the oil longitudinally away from the cavity with little lateral disturbance. The near-field impact of flow misalignment with the major axis of an open cavity is shown by comparing Runs 23, 26, and 24 for rotation angles of 0, 10, and 90 degrees, respectively. The cavity geometry in each case is  $L/H=7.2$ ,  $W/H=2.4$ , and

$H/\delta=1.1$  as measured along the major axis. Here, the flow approaches the cavity uniformly and leaves the cavity with little disturbance to the local surrounding flow field. Again the floor reveals no motion in the oil. It should also be highlighted again that as the cavity is rotated, its width changes with little local impact on the surrounding flow field. All of these oil flow visualizations support previously published observations that open cavity flows skip the cavity.

Length effects for closed flow cavities can be examined using Runs 20 and 27 for  $L/H=14$  and  $17$ , respectively. Each of these cavities has  $W/H=2.4$  and  $H/\delta=1.1$ . According to published information the lower bound for closed flow is  $L/H\approx 13-14$ , therefore only minimal movement of the oil would be expected for Run 20 and more disturbance should occur with increasing length, as it does in Run 27. Though not as apparent in the reduced resolution of the image, the originals do indicate increased motion on the cavity floor, particularly near the end wall as the flow turns to exit the cavity. Movies of the developing oil motion acquired during the test even reveal upstream movement of the oil in the cavity corners. Compared to the open cavity cases, the closed geometries have augmented wiping and spreading of the oil downstream as the flow exits the cavity near field, indicating the occurrence of stronger interactions. A downstream view of the disturbance generated by the  $L/H=17$  cavity of Run 27 is also shown, indicating two, strong persistent vortices tracking to the end of the plate, implying concern for possible heating augmentation due to boundary layer transition. These observations are, again, in accordance with published information concerning longer, closed cavities.

Some closed flow cavity width effects are shown using images for Runs 22, 20, and 21 for  $L/H=14$  cavities of depth  $H/\delta=1.1$ . These cavities have widths,  $W/H$ , of 3.6, 2.4, and 1.2, respectively, i.e. a range of  $\pm 50$  percent about the baseline width. The images are consistently scaled, notated, and presented in Figure 14 for discussion. Surface flow external to the cavities is remarkably similar in all cases. First, the oil streaks above (and below) each cavity bend toward the cavity, reflecting the reduced pressure generated in the cavity as flow expands into it. As indicated by the solid red line marked "A", these streaks reach a minimum point at approximately the same location. Next, the external flow then diverges and spreads at approximately the same angle as indicated by the dashed blue line marked "B". Internal to the cavity, little movement of the oil is apparent upstream of dotted teal line marked "C", which is a flow separation line between the main flow in the central region of the cavity and the endwall forward-facing-step flow field. Downstream of "C" the flow is a recirculation away from the endwall toward "C". The near-field effects of the cavity appear insensitive to width, probably until the two sidewalls are of such proximity that their independent viscous effects can interact – then, they become a longitudinally oriented gap.

## Surface Heating Data

Figures 15-18 present the heating data acquired for T6857, the open cavity experiment. The geometry for the models in this test series are presented in Table 3 and photographically in Figure 11, and the test matrix for this test series are presented in Tables 6-10. Figures 19-30 present the heating data for T6868, the closed cavity experiment. The model geometries for this test series are presented in Table 4 and photographically in Figure 12, and the test matrix for this test series is presented in Tables 11-16, where the runs are grouped according to objective. In each case, the heating images are unmapped, i.e. they are the two-dimensional view obtained during each run. The narrowing (perspective) and skew of the heating image is a result of the camera angle with respect to the plate. For T6857, the three different 4-inch wide by 6-inch long inserts are readily discerned. Even though the overall length is 18 inches, the phosphor fluorescence is undetectable through the Kapton tape used to seal the joints and gaps on the model upstream, downstream and between each insert. The phosphor-imaging camera was typically focused to capture the entire 4-inch by 18-inch ceramic insert region; however, for select runs the camera was focused on the immediate cavity region. These runs are indicated in the **Test-Run** column of figure by the addition of an “f” to the value (ex. 6857-096 f indicates Test 6857 Run 096 focused). For select “screening” runs, the SLA models were painted with an insulating coating and sprayed with the phosphor. Therefore, these runs offer only a qualitative thermal foot print (analogous to an oil flow footprint), because the thermal properties of the model are unavailable for determining the heating. These runs are denoted in the **Config** column by appending an “s” the configuration identifier (ex. 9 s indicates Configuration 9 SLA). For this section, only qualitative remarks are presented regarding the image data.

For the T6857 baseline plate cases presented in Figure 15, fairly uniform heating is observed, even though very small levels are realized because the thermal driving potential for grazing flows on a plate are small for this facility. Accordingly, larger uncertainties and scatter will be evident in all of the data acquired in lower temperature regions of the flow.

The open (short) cavity heating images for T6857 are presented in Figure 16, and they are ordered first according to configuration number (note the color coding) and then according to test condition. Recalling from Table 1, the target depth  $H/\delta$  range of 0.72 to 1.76 and the target  $Re_\theta$  range of 136 to 241, it is obvious that none of the Configuration 3 or 5 cases develop any appreciable rise in the end wall or floor heating until considerably beyond expected limits on the vehicle, as is evident in Run 49, where the  $H/\delta=3.37$  and  $Re_\theta=461$ . In all cases, the heating drops on the cavity floor, as anticipated from the literature and flow physics discussions. The effect of increasing the cavity depth,  $H/\delta$ , at matched  $Re_\theta$  is to increase the heat load on the cavity floor. For example, compare Configuration 5 Runs 60, 61, and 62 with Configuration 3 Runs 47, 48, and 49, respectively. Several special cases of Configuration 3 were developed: namely, 3-

Gouge, 3-Gap, and 3-Slot. The Gouge configuration offers a “more damage-like” effect of the ragged bottom and sides appears to reduce the average depth of the cavity, thereby reducing the heating (see Runs 42, 43, 44, and 45) compared to the standard Configuration 3. The Gap configuration examines the impact of removing the gap fillers from the end of the cavity, allowing some flow relief inside the cavity. These runs are 51, 52, 57, 58, and 59. Test Runs 93 through 96 were focused views of the gap region, allowing enhanced viewing of the cavity. Finally, an attempt was made to examine the floor heating when a slot exists along the bottom side of the cavity, as would exist behind a carrier panel. Here, a slot was cut along the bottom side of the cavity and in-cavity flow was directed into a plenum attached to the back of the model. The plenum was evacuated into a large dump tank maintained at near vacuum. This test series includes runs 102 through 106.

Oil flow visualizations presented in Figures 13-14 indicated that external flow skipped over open cavities with little effect, whether aligned with or skewed from the main flow. This same no-significant-effect observation can be applied to the heating of open cavities in Figure 17 where Configuration 8 at  $0^\circ$  rotation (i.e. aligned with the stream) is compared with Configuration 11 at  $10^\circ$  rotation for a large range of depths (1.1 to 2.11) and  $Re_\theta$  (205 to 394).

A series of screening experiments was conducted during T6857 to preview the effects of closed (long) cavities. Unlike the skimming flow over open cavities that displayed only minor heating augmentation with changes near the target conditions, closed cavities are long enough to allow sufficient turning for flow entry. The turning into the cavity, along the floor, and out of the cavity creates substantial high shear regions that generate increases in the heating. Corners offer the possible development of vortices that, again, create high shear regions. These effects are presented in Figure 18 for  $L/H=14$  and  $17$  cavities. Typically, stronger interactions occur with longer cavities, thereby enhancing the heating. Figure 18 also offers a width-effect series for heating of  $L/H=14$  at matched entry conditions. As with the oil flow visualizations, these were conducted at  $W/H$  values of 1.2, 2.4, and 3.6. An example of this variation at matched conditions can be observed in Runs 91f, 81f, and 82f, respectively. As the cavity is widened, the major effect appears to be a spreading of the vortices exiting the cavity region (e.g. compare Runs 81f with 82f). The largest variations appear for the narrowest cavity (e.g.  $W/H=1.2$ , Run 91f) where the sidewalls may be close enough for the occurrence of side-to-side vortical interactions.

The baseline heating runs for T6868 are presented in Figure 19 over the range of expected test conditions. As with T6857, fairly uniform spanwise heating is observed and a uniform drop in the heating occurs, as would be expected of laminar flow conditions. A significant exception occurs with Run 123 acquired at conditions where transition to turbulence would not be unexpected on the aft end of the plate, and this indeed appears to be the case. Two baseline cases, Runs 30 and 31, were acquired at  $Re=0.5 \times 10^6/ft$ . These two runs display a high degree of scatter in the heating and extremely

low heating for Run 31, again highlighting the low thermal driving potential of the facility. Accordingly, larger uncertainties and scatter will be evident in all of the data acquired in lower temperature regions of the flow.

Figure 20 presents the results from a limited number of open cavity runs that were made to check the consistency of the test process and to verify consistency of observations between T6857 and T6868. Note that Configuration 5 is a standard ceramic model and Configuration 9s is an SLA insert.

Cavity length effects are presented as shown in Figures 21 through 24 for lengths  $L/H=14$  to 30.

	$H/\delta$	$L/H$	$Re_\theta$	$Me$
	Range			
<b>Figure 21</b>	1.1	14-30	300	2.90
<b>Figure 22</b>	2.4	14-25	300	2.90
<b>Figure 23</b>	1.1	14-25	500	2.90
<b>Figure 24</b>	2.4	14-20	500	2.90

Generally, longer cavities produce greater effects on the cavity floor and on the downstream. This is in direct response to the increase of high-energy fluid entering the cavity. The longer cavities enable the development of stronger vortices on the top outside edges as the flow rolls into the lower-pressure regions, and development of corner vortices in the junction between the sidewall and floor. These stronger interactions increase the shearing with the cavity structure providing increased resistance to maintaining laminar flow, and transitional or turbulent flow may occur in the cavity.

Deeper, long cavities greatly enhance the heating and the possibility of transition to turbulence. These effects are presented in Figures 25 through 28 as follows:

	$H/\delta$	$L/H$	$Re_\theta$	$Me$
	Range			
<b>Figure 25</b>	2.39	14-30	500	2.25
<b>Figure 26</b>	5.20	14-30	500	2.25
<b>Figure 27</b>	0.65	14-25	260	2.25
<b>Figure 28</b>	2.70	14-30	260	2.25

The effects are strongly demonstrated by comparing Figures 25 and 26 where the depth,  $H/\delta$ , increases from 2.4 to 5.2 and then in Figures 28 and 27 where depth decreases from a deep 2.70 to a shallow 0.65. In this latter case, it becomes difficult to see the cavity foot print in the heating image because of the lower-disturbance shallow cavity.



The effect of edge Mach number,  $M_e$ , can be evaluated by comparing Figures 24 and 25. These Figures have the following conditions:

	H/ $\delta$	L/H Range	$Re_\theta$	$M_e$
<b>Figure 24</b>	2.4	14-20	500	2.90
<b>Figure 25</b>	2.4	14-30	500	2.25

Care should be exercised to ensure that the transitional-turbulent flow has not occurred and that a proper comparison is being conducted.

Pressure gradient effects are examined in Figure 29. The derivation of the surface geometry is presented in the Appendix. Since these are SLA models coated, first, with an insulating paint and, then, with the phosphor, only the qualitative observations can be provided regarding their behavior, since the thermal properties of the SLA resin are unknown. The data are presented with caveats. First, all cavity-entry conditions were determined using the  $dc_p/dx=0$  results from the laminar LAURA CFD solutions — no CFD solutions were developed for the gradient surface. Though boundary layer edge conditions at the beginning of the insert plate (station 7.5) are the same for each model test set and though each model has a prescribed design pressure gradient, the actual conditions at the entry of the cavity will differ somewhat for the different gradient conditions. For example, the expansion surface will increase Mach number above the baseline while the compression surface will decrease Mach number. Without substantiation, this effect is believed minimal because the cavities are located upstream on the insert at station 10.5 before large changes in edge conditions occur. Next, spanwise gradients are also believed to be minimal at the cavity because the presence/absence of sidewall constraints at the insert edge is small (recall that the insert is only 4 inches wide); downstream the effect may be more pronounced. With these qualifiers, scaled dimensions (L/H, W/H, H/ $\delta$ ) of (20, 2.4, 1.1) are assigned to the first set of target test conditions of  $M_e=2.895$  and  $Re_\theta=300$  ( $\alpha=0^\circ$ ). Entry and exit boundary layer states for this case are laminar based on analysis of the heating levels. At the second set of conditions,  $M_e=2.245$  and  $Re_\theta=503$  ( $\alpha=-10^\circ$ ), the cavity depth is increased to 2.4. The entry boundary layer is laminar for this condition; however, the exit boundary layer is turbulent, indicating shear layer transition within the cavity. For the first set of test conditions, gradient effects are not obvious in the vicinity of the cavity with the possible exception of changes in vortex strength downstream. However, for the second set of test conditions, the gradient effects are definitely evident, particularly downstream for the negative gradient with  $dc_p/dx=-.005$  where a severe narrowing of the cavity wake occurs and where significant heating augmentation appears. As the gradient increases, the cavity wake spreads and the separation line between the wake and the surrounding “undisturbed” flow straightens. Also, heating augmentation appears to decrease near the cavity for increasing  $dc_p/dx$ . Unfortunately, the available data are insufficient to independently assess the influences of the longitudinal and lateral gradients.

The impact of flow misalignment with the cavity major axis is examined in Figures 30 and 31 for L/H=20 cavities. Since these are SLA models, only the impact of the rotation angle on the flow field and qualitative levels can be evaluated. Four angles are available 0° (the baseline case), 15°, 30°, and 45°. The conditions of these tests are:

	H/δ	L/H	Re <sub>θ</sub>	Me
<b>Figure 30</b>	1.1	20	300	2.90
<b>Figure 31</b>	2.4	20	500	2.25

As is evident in the figures, a skewed cavity can have a significant impact on the heating levels and on the downstream transition process. A skewed/rotated cavity allows an increase in the high-energy mass flowing into the cavity, and it develops a non-axial velocity component that enhances mixing and shearing. A closed-flow, rectangular cavity will increase in length as it is rotated until the cavity diagonal is aligned with the stream, after which it will decrease and the flow will ultimately become that of an open-flow, rectangular cavity with significantly reduced heating, if the W/H<10.

## Phosphor Uncertainty Analysis

Merski published the uncertainties for the phosphor thermography method as a whole in 1999. Uncertainties in that report were determined under conditions where much larger temperature increases were experienced. For the present test, conditions on the grazing-flow models presented here generate a much smaller temperature change from the pre-run value, implying the existence of larger uncertainties. Typically, the analysis metric of choice has been the heating augmentation above/below the undisturbed ambient condition for both the experimental data and computational simulations. This metric is known as Bump Factor (*BF*) and it is the uncertainty in this parameter that is actually desired. *BF* is defined as a local normalization of  $h/h_{ref}$  by a reference average heating value obtained upstream of the cavity,  $h_{avg}/h_{ref}$ . Thus,

$$BF = (h/h_{ref})/(h_{avg}/h_{ref}) = (h/h_{avg})$$

When presented and analyzed in this format the disturbance field introduced by the cavity is readily discernable, because the undisturbed state has a nominal value of unity. *BF* uncertainty levels were presented in Everhart, et al. (2006) by adding phosphor heat-transfer bump-factor uncertainty algorithms to the MAP3D code, resulting in global uncertainty surface maps similar to the three-dimensional heat transfer maps. The process from that publication is outlined below.

The solution of the heat conduction equation (i.e. the data reduction equation) used in the IHEAT code is given by

$$\frac{\Theta}{h_{aw}(T_w / h_w) - T_{init}} = 1 - e^{\Lambda^2} \operatorname{erfc} \Lambda$$

where

$$\Theta(x, y, t) = T(x, y, t) - T(x, y, 0) = T(x, y, t) - T_{init}$$

and

$$\Lambda = \frac{h(h_{aw} / T_w)\sqrt{t}}{\beta}$$

Also,  $h$  is the convective heat transfer coefficient,  $h_{aw}$  is the adiabatic wall enthalpy,  $h_w$  is the wall enthalpy,  $T_w$  is the corresponding wall temperature, and  $t$  is the effective time of data acquisition.  $\beta$  is the thermal product of the substrate materials and it is the square root of the product of the material density, specific heat, and thermal conductivity. Bias and precision uncertainty values developed at the 95 percent confidence level for each parameter appearing in the data reduction equation are given in Table 12.

Each of these individual parameter uncertainties was individually inserted into the data reduction equation to determine a component uncertainty in heat transfer coefficient. The bias uncertainty,  $B$ , and the precision uncertainty,  $P$ , for the heat transfer coefficient were determined by obtaining the root-sum-square (RSS) from each of the component uncertainties using

$$B = \left( \sum B_j^2 \right)^{\frac{1}{2}} \quad \text{and} \quad P = \left( \sum P_j^2 \right)^{\frac{1}{2}}$$

where  $j$  is the number of component uncertainties. Total uncertainties are obtained by taking the RSS of the bias and precision uncertainties. Bias and total uncertainties of the heat transfer coefficients are determined at every pixel point imaged on the model.

Bump factors extracted from the mappings were used in two ways: 1) as line cuts when selecting specific data, and 2) as regions of interest over which all of the data were averaged. In the first case, the total uncertainties are applicable. In the latter case, bias uncertainties are applicable because precision uncertainties are removed during averaging, since they are primarily due to random pixel scatter. Accordingly, the average heat transfer coefficient  $h_{avg}$  used to compute bump factors was assumed to have only a bias uncertainty. Typically, total uncertainties are determined using the quotient rule by adding the total uncertainty in  $h_{local}$  to the bias uncertainty in  $h_{avg}$ . For nominally flat models of this type, very low heating rates are obtained during a run and the resulting uncertainties were initially very high. Yet, comparisons of line cuts were more consistent than the uncertainty analysis seemed to suggest. While conservatism is important, excessive conservatism is undesirable. Therefore, the phosphor temperature lookup table data were re-examined and it was determined that since there was minimal variation of incident UV intensities on the models during the tunnel runs, and because of the low heating measurements, the data were typically confined to one very small segment of the temperature range. Thus, the bias uncertainties for the data used in calculating  $h_{local}$  and  $h_{avg}$  were uni-directional and determinate. Therefore, the bias uncertainties in  $h_{local}$  and the bias uncertainties in  $h_{avg}$  had to be subtracted via the quotient rule,

instead of added, when computing bias uncertainties for the augmentation factors. Similarly, total uncertainties in augmentation factors were then obtained simply by taking the RSS of the bias and precision uncertainties in  $h_{local}$  and by subtracting the bias uncertainties in  $h_{avg}$  (since the precision uncertainties were negligible).

Following this procedure, representative within-run total and bias uncertainties for open cavity flows are typically less than 10% over the plate surface. In the cavity where the lowest temperatures are experienced, the bias uncertainties are about 10%, while the total uncertainties approach 20%. For the closed conditions, the temperature rise is generally greater, resulting in lower within-run bias uncertainties (3-4 percent or lower) with the exception of the low temperature regions on the cavity floor. Total within-run uncertainties are in the 10-20 percent range. An assessment of the within-test uncertainties, including run-to-run, model-to-model, etc. can be found in the "The Cavity Heating Tool" documentation OEAN-0305-001 by Anderson, *et al.* (2005).

## Summary

Two cavity heating experiments have been conducted in support of the Columbia Accident Investigation Board in the NASA Langley 20-Inch Mach 6 Tunnel at laminar-entry fluid-dynamic boundary-layer edge conditions typical of the Columbia Orbiter vehicle at Mach 18. The first experiment concentrated on open (short) cavity geometries, while the second focused on closed (long) cavity geometries. Rectangular planform geometries with flat bottoms and nearly vertical side walls and end walls were used in the modeling, representing what is believed to be a worst case, missing tile(s), non-breeching, damage configuration. Global surface heating distributions were acquired for each test configuration via the two-color thermographic phosphor method and oil flow visualizations were used to assess the surface flow characteristics of select configurations. The present report summarizes the philosophy developed to scale from flight-to-tunnel and testing processes used to acquire the data. Results are presented in image format and were provided during the test to the Aeroheating Damage Assessment Team for further analysis.

The traditional definitions for cavity flow regimes are  $L/H < 10$  for open cavities and  $L/H > 13-14$  for closed cavities. These definitions appear consistent with the present observations in hypersonic flow, though insufficient data are available to assess the validity of the regime limits. The present cavities of  $L/H = 7.2$  and 8 with depths ranging from  $H/\delta = 0.92$  to 3.37 exhibit characteristics prescribed to open flows where the mainstream flow skips over the top of the cavity. Both oil flow and heating observations of these geometries indicate little disturbance to the surrounding environment with only a heating peak and recovery zone on the downstream endwall top edge. This is further supported by the observation that rotation of the cavity off the stream axis has little impact on sur-

rounding surface flow. Virtually no oil-flow motion was observed on the cavity floor, implying a low shear region and accordingly a drop in the surface heating. Since the flow skips over the cavity, the cavity floor is isolated from the high-energy external stream.

Closed cavities of lengths  $L/H=14$  to  $30$  were tested over a depth range  $H/\delta=0.65$  to  $5.2$ . Global phosphor thermography of closed cavities has revealed highly three-dimensional surface heating details and vortical interactions in both the near-field and far-field that would have been impossible to observe using discrete-sensor measurement techniques. These cavities are highly vortical; they have large regions of high shear and significant energy may be transferred not only to the cavity floor from the external stream, but also to the endwall and the surrounding side and downstream surfaces. Longer cavities allow sidewall and floor vortex strengths to increase. These enhanced vortices increase the shearing and energy transfer to the cavity surfaces. The increased vortical mixing enhances the possibility of transition-to-turbulence within the cavity and downstream. Deeper closed cavities allow more backflow in the cavity in separation regions and allow greater flow-turning angles to be realized. The increased flow-turning promotes stronger shock and expansion waves, thereby augmenting the heating in these regions. When cavity width was increased the major local effect was to spread the vortices that develop on the sidewalls and their impingement points on the endwall. The major flow features in the cavity and on the endwall, and the resulting heating does not appear to be affected to first order with these width changes. Significant heating changes due to decreasing the width will probably appear only when the sidewall vortices are close enough to mutually interact.

The effects of external pressure gradient on the cavity heating and cavity misalignment with the main stream were screened for closed cavities using phosphor-coated SLA models. These tests allow only a thermal footprint of the disturbance to be examined, much like an oil flow visualization. Longitudinal and lateral pressure gradient effects were observed in the images, but because of model constraints their individual effects can not be separated in the data. Rotating the closed cavity to create a misalignment with the stream introduces a lateral velocity in the cavity, increases the shearing and vorticity, and results in augmented heating and flow disturbance and increased the probability of transition-to-turbulence with and downstream of the cavity.

## References

Adams, J.C., Jr.: "Numerical Calculation of Hypersonic Laminar Cavity Flows," AIAA Paper 74-707, ASME 74-HT-27, AIAA/ASME 1974 Thermophysics and Heat Transfer Conference, Boston, Mass., July 1974.

Anderson, John D., Jr.: "Hypersonic and High Temperature Gas Dynamics," McGraw-Hill Book Co., New York, 1989.

Anderson, Brian, Hyatt, Jay, Wang, K.C., Everhart, Joel, Greene, Frank, Pulsonetti, Maria, Wood, Bill, Bourland, Gary, and Cassady, Amy: "The Cavity Heating Tool," OE-AN 0305-001, Johnson Space Center, March 15, 2005.

Berry, S.A.; Difulvio, Michael; and, Kowalkowski, Matthew K., "Forced boundary-Layer Transition on X-43 (Hyper-X) in NASA LaRC 20-Inch Mach 6 Air Tunnel." NASA TM-2000-210316, Aug. 2000.

Berry, S.A.; Auslender, A.H.; Dilley, A.D.; and Calleja, J.F., "Hypersonic Boundary-Layer Trip Development for Hyper-X," Journal of Spacecraft and Rockets, Volume 38, Number 6, pp. 853-864, 2001.

Blair, A.B., Jr. and Stallings, R.L., Jr.: "Supersonic Axial-Force Characteristics of a Rectangular-Box Cavity with Various Length-to-Depth Ratios in a Flat Plate," NASA TM-87659, 1986.

Boerrigter, Herman and Charbonnier, Jean-Marc: "Roughness-induced transition in hypersonic flow," Space Scientific Research in Belgium, Volume 4; 51-52; D/1996/1191/5-Vol-4/ (SEE 19970005230)

Buck, G.M., and Vasques, P.: "An Investment Ceramic Slip-Casting Technique for Net-Form, Precision, Detailed Casting of Ceramic Models," U.S. Patent 5,266,252, November 1993.

Buck, Gregory M., Pulsonetti, Maria V., and Weilmuenster, K. James: "Downstream Effects on Orbiter Leaside Flow Separation for Hypersonic Flows," AIAA Paper 2005-5138, 38th AIAA Thermophysics Conference, Toronto, Canada, June 6-9, 2005.

Buck, G.M., Powers, M.A., Nevins, S.C., Griffith, M.S., Verneris, P.H., and Wainwright, G.A.: "Rapid Fabrication of Flat Plate Cavity Phosphor Thermography Test Models for Shuttle Return-to-Flight Aero-Heating," NASA/TM-2006-214508, November 2006.

Burggraf, O.R.: "A Model of Steady Separated Flow in Rectangular Cavities at High Reynolds Number," Proceedings of the 1965 Heat Transfer and Fluid Mechanics Conference, Stanford University Press, 1965, pp. 190-229.

Carlson, W.O.: "A Solution to Heat Transfer in Laminar Separated and Wake Flow Regions," General Electric R59 SD-356, March 1959.

Chang, P.K.: "The Reattachment of Laminar Cavity Flow with Heat Transfer at Hypersonic Speed," AFOSR-66-0135, 1966.

Chapman, D.: "A Theoretical Analysis of Heat Transfer in Separated Flow," NACA TN-3792, October 1956.

Charbonnier, J.-M., and Boerrigter, H.L.: "Contribution to the study of gap induced boundary layer transition in hypersonic flow," AIAA Paper 93-5111, presented at AIAA and DGLR, 5th International Aerospace Planes and Hypersonic Technologies Conference, Munich, Germany, November 30-December 3, 1993.

Charwat, A.F., Roos, J.N., Dewey, C.F., Jr., and Hitz, J.A.: "An Investigation of Separated Flows – Part I: The Pressure Field," *Journal of Aerospace Sciences*, Vol. 28, No. 6, June 1961, pp. 457-470.

Charwat, A.F., Dewey, C.F., Roos, J.N., and Hitz, J.A.: "An Investigation of Separated Flows – Part II: Flow in the Cavity and Heat Transfer," *Journal of Aerospace Sciences*, Vol. 28, No. 7, pp. 513-527, July 1961.

Chin, E., Rafiinejad and Seban, R.A.: "Prediction of the Flow and Heat Transfer in a Rectangular Wall Cavity with Turbulent Flow," Transactions of the ASME, *Journal of Applied Mechanics*, Vol. 39, Series E, No. 2, pp. 351-358, June 1972.

Cheatwood, F. McNeil, Merski, N. Ronald, Jr., Riely, Christopher J., and Mitcheltree, Robert A.: "Aerothermodynamic Environment Definition for the Genesis Sample Return Capsule," AIAA 2001-2889, Presented at 35th AIAA Thermophysics Conference, Anaheim, CA, June 11-14, 2001.

Coats, Jack D., Rhudy, R.W., and Edmunds, E.W.: "Effects of Surface Gaps and Steps on Laminar Heat-Transfer Rates at Local Mach Numbers from 3 to 10," AEDC-TR-70-17, February 1970.

Dye, Thomas P., Everhart, Joel L., Hodge, J.A.: "Blockage Induced by Large Test Technique Demonstrator Models with Propulsion Simulation in the NASA Langley 31-Inch Mach 10 Tunnel," NASP Technical Memorandum 1163, 1992.

Emery, A.F.: "Recompression Step Heat Transfer Coefficients for Supersonic Open Cavity Flow," *Journal of Heat Transfer*, 1969, pp. 168-170.

Everhart, Joel L., Alter, Stephen J., Merski, N. Ronald, Wood, William A., and Prabhu, Ramadas K.: "Pressure Gradient Effects on Hypersonic Cavity Flow Heating," AIAA 2006-0185, Presented at 44<sup>th</sup> AIAA Aerospace Sciences Meeting and Exhibit, Reno, CA, January 9-12, 2006.

Fay, J.A. and Riddell, F.R.: "Theory of Stagnation Point Heat Transfer in Dissociated Air," *Journal of Aeronautical Sciences*, Vol. 25, No. 2, 1958, pp. 73-85.

Fletcher, L.S., Briggs, D.G., and Page, R.H.: "A Review of Heat Transfer in Separated and Reattached Flows," AIAA-70-767, July 1970.

Galenter, S.A.: "An Experimental Summary of Plasma Arc Exposures of Space Shuttle High-Temperature Reusable Surface Insulation Tile Array with a Single Missing Tile (Conducted at the Ames Research Center)," NASA SP-379, Paper 18, 1975.

Gnoffo, P.A., Gupta, R.N., and Shinn, J.L.: "Conservation Equations and Physical Models for Hypersonic Air Flows in Thermal and Chemical Nonequilibrium," NASA TP 2867, February 1989.

Gnoffo, P.A.: "An Upwind-Biased, Point-Implicit Relaxation Algorithm for Viscous, Compressible Perfect Gas Flows," NASA TP 2953, February 1990.

Hahn, Mansop: "Experimental Investigation of Separated Flows over a Cavity at Hypersonic Speed," AIAA No. 68-672, *AIAA Journal*, Vol. 7, No. 6, June 1969, pp. 1092-1098.

Hollis, B.R.: "Real-Gas Flow Properties for NASA Langley Research Center Aerothermodynamic Facilities Complex Wind Tunnels," NASA CR 4755, September 1996.

Hollis, Brian R. and Liechty, Derek S.: "Boundary Layer Transition Correlations and Aeroheating Predictions for Mars Smart Lander," AIAA 2002-2745, Presented at 32nd AIAA Fluid Dynamics Conference and Exhibit, St. Louis, Missouri, 24-26 June 2002.

Hollis, Brian R. and Liechty, Derek S.: "Correlations for Boundary Layer Transition on Mars Science Laboratory Entry Vehicle due to Heat-Shield Cavities," NASA/TP-2008-215317, June 2008.

Hunt, L.R.: "Aerodynamic Heating and Loading within Large Open Cavities in Cone and Cone-Cylinder-Flare Models at Mach 6.7," NASA TN D-7403, March 1974.

Hunt, L.R.: "Aerodynamic Heating in Large Cavities in an Array of RSI Tiles," NASA TN D-8400, 1977.



Johnson, C.B.: "Heat Transfer Data to Cavities between Simulated RSI Tiles at Mach 8," NASA CR 128770, June 1973.

Lamb, J.P.: "An Approximate Theory for Developing Turbulent Free Shear Layers," *Trans. ASME*, Series D, Vol. 89, No. 3, 1967, pp. 633-642.

Lamb, J.P. and Bass, R.L.: "Some Correlations of Theory and Experiment for Developing Turbulent Free Shear Layers," *Trans. ASME*, Series D, Vol. 90, No. 4, pp. 572-580, 1968.

Lamb, J.P.: "Convective Heat Transfer Correlations for Planar, Supersonic, Separated Flows", *Trans. ASME*, Series C, Vol. 102, No. 2, May 1980, pp. 351-356.

Lamb, J.P.: "Analysis and Correlation of Convective Heat Transfer Measurements for Open Cavities in Supersonic Flow," AIAA 80-1526, July 1980.

Larson, H.K. and Keating, Jr., S.L.: "Transition Reynolds Numbers of Separated Flows at Supersonic Speeds," NASA TN D-349, December 1960.

Liechty, Derek S., Berry, Scott A., Hollis, Brian R., and Horvath, Thomas J.: "Comparison of Methods for Determining Boundary Layer Edge Conditions for Transition Correlations," AIAA Paper No 2003-3590, Presented at 33rd AIAA Fluid Dynamics Conference and Exhibit, Orlando, FL, June 23-26, 2003.

Liechty, Derek S., Horvath, Thomas J., and Berry, Scott A.: "Shuttle Return to Flight Experimental Results: Cavity Effects on Boundary Layer Transition," NASA TM-2006-214305, June 2006.

Liechty, Derek S., Berry, Scott A., and Horvath, Thomas J.: "Shuttle Return to Flight Experimental Results: Protuberance Effects on Boundary Layer Transition," NASA TM-2006-214306, June 2006.

Merski, N.R.: "Global Aeroheating Wind Tunnel Measurements Using Improved Two-Color Phosphor Thermography Method," *Journal of Spacecraft and Rockets*, Vol. 36, No. 2, 1999, pp. 160-170.

Merski, N.R.: "An Improved Two-Color Relative-Intensity Phosphor Thermography Method for Hypersonic Wind Tunnel Aeroheating Measurements," NASA CDTP-1017, February 2001.

Micol, J.R.: "Hypersonic Aerodynamic/Aerothermodynamic Testing Capabilities at Langley Research Center: Aerothermodynamic Facilities Complex," AIAA Paper 95-2107, June 1995.

Morgenstern, A. and Chokani, N.: "Hypersonic Flow Past Open Cavities," *AIAA Journal*, Vol. 32, pp. 2387-2393, 1994. (Computational).

Nestler, D.E.: "Laminar Heat Transfer to Cavities in Hypersonic Low Density Flow," Proceedings 3rd International Heat Transfer Conference, Chicago, IL, Vol. 2, 1966.

Nestler, D.E., Saydah, A.R., and Auxer, W.L.: "Heat Transfer to Steps and Cavities in Hypersonic Turbulent Flow," AIAA Paper No. 68-673, 1968.

Nestler, D.E., Saydah, A.R., and Auxer, W.L.: "Heat Transfer to Steps and Cavities in Hypersonic Turbulent Flow," *AIAA Journal*, Vol. 7, No. 7, July 1969, pp. 1368-1370.

Nestler, D.E.: "Hypersonic Boundary Layers and Selected Heat Flux Problems," Short Course on Technology of Space Shuttle Vehicles and Space Stations at the University of Tennessee Space Institute, April 1970.

Nestler, D.E.: "Hypersonic Laminar Cavity Heat Transfer," Presented at 4th International Heat Transfer Conference, August 31-September 5, 1970, Versailles, France.

Nestler, D.E.: "An Engineering Analysis of Reattaching Shear Layer Heat Transfer," AIAA Paper 72-717, Presented at 5th AIAA Fluid and Plasma Dynamics Conference, Boston, Mass., June 26-28, 1972.

Nestler, D.E.: "An Experimental Study of Cavity Flow on Sharp and Blunt Cones at Mach 8," AIAA-81-0335, AIAA 19th Aerospace Sciences Meeting, St. Louis, Missouri, January 12-15, 1981.

Nestler, D.E.: "The Effects of Surface Discontinuities on Convective Heat Transfer in Hypersonic Flow," AIAA Paper 85-0971, AIAA 20th Thermophysics Conference, Williamsburg, VA, June 1985.

Netterfield, M.P. and Hilier, R.: "Experiment and computation in hypersonic cavity flows," AIAA Paper 89-1842, Presented at, 20<sup>th</sup> AIAA Fluid Dynamics, Plasma Dynamics and Lasers Conference, Buffalo, NY, June 12-14, 1989.

Nicoll, K.M.: "An Experimental Investigation of Laminar Hypersonic Cavity Flows Part II: Heat Transfer and Recovery Factors Measurements," ARL 63-73.

Nicoll, K.M.: "A Study of Laminar Hypersonic Cavity Flows," *AIAA Journal*, Vol. 2, No. 9, September 1964.

Pulsonetti, M. and Thompson, R.: "LAURA Aerothermodynamic Computations for Space Shuttle Columbia STS-107 Baseline and Damage Scenarios," AIAA Paper 2004-

2278, Presented at 37th AIAA Thermophysics Conference, Portland OR, June 28-July 1, 2004.

Pulsonetti, M.V. and Wood, W.A.: "Computational Aerothermodynamic of Space Shuttle Orbiter Tile Damage – Open Cavities", AIAA-2005-4679, 38th AIAA Thermophysics Conference, Toronto, Canada, June 6-9, 2005.

Reuther, J., McDaniel, R., Brown, J., Prabhu, D., and Saunders, D.: "External Computational Aerothermodynamic Analysis of the Space Shuttle Orbiter at STS-107 Flight Conditions," 37<sup>th</sup> AIAA Thermophysics Conference, Portland, OR, June 28-1, 2004.

Rhudy, J.P. and Magnan, Jr., J.D.: "Investigation of Heat-Transfer Distribution in Several Cavity and Step Configurations at Mach 10," AEDC Technical Documentary Report No. AEDC-TDR-64-220, October 1964.

Shchukin, V.K., Gortyshov, Yu. F., Varfolomeev, I.M., and Nadyrov, N.A.: "Influence of Relative Depth and Reynolds Number on Heat Transfer in Cavities in Compressible Gas Flow," Soviet Aeronaut., Vol. 23, No. 3, 1980, pp. 83-86.

Stallings, Robert L., Jr. and Wilcox, Floyd J., Jr.: "Experimental Cavity Pressure Distributions at Supersonic Speeds", NASA TP 2683, June 1987.

Stallings, Robert L., Jr., Wilcox, Floyd J., Jr., and Forrest, Dana K.: "Measurements of Forces, Moments, and Pressures on a Generic Store Separating From a Box Cavity at Supersonic Speeds," NASA TP 3110, September 1991.

Throckmorton, D.A.: "Heat Transfer to Surface and Saps of RSI Tile Arrays in Turbulent Flow at Mach 10.3," NASA-TM-X-71945, April 1974.

Weinstein, Irving, Avery, Don E., and Chapman Andrew J.: "Aerodynamic Heating to the Gaps and Surfaces of Simulated Reusable-Surface-Insulation Tile Arrays in Turbulent Flow at Mach 6.6," NASA TM X-3225, November 1975.

Wilcox, Floyd J., Jr.: "Experimental Investigation of Porous-Floor Effects on Cavity Flow Fields at Supersonic Speeds," NASA TP 3032, November 1990.

Wilcox, Floyd J., Jr.: "Tangential, Semi-submerged, and Internal Store Carriage and Separation at Supersonic Speeds," AIAA Paper 91-0198, Presented at 29th Aerospace Sciences Meeting, Reno NV., January 1991 (Cavity passive-venting effects.)

Wood, William A., Pulsonetti, Maria V., Everhart, Joel L., and Bey, Kim S.: "Assessment of Laura for Laminar Supersonic Shallow Cavities," Presented at 34th AIAA Fluid Dynamics Conference, Portland OR, June 28-July 1, 2004.

Wright, M.J., Candler, G., and Bose, D.: "Data-Parallel Line Relaxation Method for the Navier-Stokes Equations," *AIAA Journal*, Vol. 36, No. 9, 1998, pp. 1603-1609.

Wyborny, W., Kabelitz, H.P. and Schepers, H.J.: "Hypersonic Investigation on the Local and Average Heat Transfer in Cavities and after Steps of Bodies of Revolution," AGARD Conference Proceedings No. 19, Fluid Physics of Hypersonic Wakes, 1967.

Zhang, J., Morishita, E., Okunuki, T., and Itoh H.: "Experimental and Computational Investigation of Supersonic Cavity Flows," AIAA Paper 2001-1755, Presented at AA/NAL-NASDA-ISAS 10th International Space Planes and Hypersonic Systems and Technologies Co.

## Tables

**Table 1.- Flight Scaled Cavities and Conditions.**

Location	$M_e$	$Re_\theta$	$\delta$ (inch)	$H/\delta$	W/H	L/H
Carrier Panel 6	3.0713	136.2	1.7643	1.70	1.33	8.0
Carrier Panel 7	3.1107	132.9	1.7084	1.76	1.33	8.0
Tile PT-T	3.1376	163.4	2.2742	1.10	2.40	7.2
Tile PT-O	3.0591	172.6	2.3628	1.06	2.40	7.2
Tile PT-M	3.0417	219.9	3.2046	0.78	2.40	7.2
Tile PT-I	3.0122	241.3	3.4737	0.72	2.40	7.2

**Table 2.- Nominal flow conditions in the 20-Inch Mach 6 Air Tunnel.**

$Re_\infty \times 10^{-6}$ (1/ft)	$M_\infty$	$p_{t1}$ (psi)	$T_{t1}$ (°R)
.56	5.93	30.63	856.33
.84	5.91	46.20	863.70
1.08	5.94	61.10	874.65
1.39	5.95	81.33	886.94
1.72	5.96	101.73	859.87
2.09	5.98	126.52	903.14
2.49	5.98	151.40	903.82
2.98	5.99	181.96	904.78
3.46	6.00	212.63	905.85
4.12	6.00	252.61	905.93
4.65	6.01	292.75	920.01
5.41	6.02	343.57	924.47
6.13	6.02	393.28	929.03
6.98	6.03	450.89	933.62
7.38	6.03	476.62	933.80

**Table 3.- Cavity models for Test 6857 - Columbia accident investigation.**

Config	X <sub>1</sub> model (inch)	X <sub>2</sub> cavity (inch)	M <sub>e</sub>	Re <sub>θ</sub>	δ (inch)	H/δ	W/H	L/H	H (inch)	W (inch)	L (inch)	Rotation (deg)	dCp/dX (per ft)
1						0.0	0.0	0.0					
3	14.4	6.858	2.895	241	0.305	1.8	1.3	8.0	0.536	0.714	4.285	0	0
3	14.4	6.858	2.895	241	0.305	1.8	1.3	8.0	0.536	0.714	4.285	0	0
Gouge 3	14.4	6.858	2.895	241	0.305	1.8	1.3	8.0	0.536	0.714	4.285	0	0
Gaps 3	14.4	6.858	2.895	241	0.305	1.8	1.3	8.0	0.536	0.714	4.285	0	0
5	15.4	7.883	2.895	461	0.159	1.8	1.3	8.0	0.279	0.372	2.234	0	0
8	9.6	2.050	2.895	205	0.240	1.1	2.4	7.2	0.264	0.633	1.900	0	0
11	9.6	2.050	2.895	205	0.240	1.1	2.4	7.2	0.264	0.633	1.900	10	0
15	9.6	2.050	2.895	205	0.240	1.1	2.4	7.2	0.264	0.633	1.900	90	0
16	8.7	1.153	2.895	205	0.240	1.1	1.2	14.0	0.264	0.317	3.694	0	0
17	8.7	1.153	2.895	205	0.240	1.1	2.4	14.0	0.264	0.633	3.694	0	0
18	8.7	1.153	2.895	205	0.240	1.1	3.6	14.0	0.264	0.950	3.694	0	0
19	8.3	0.757	2.895	205	0.240	1.1	2.4	17.0	0.264	0.633	4.485	0	0

**Table 4.- Cavity models for Test 6868 - Closed cavity geometry parameters.**

Config	X, model (inch)	X, cavity (inch)	$M_e$	$Re_\theta$	$\delta$ (inch)	H/ $\delta$	W/H	L/H	H (inch)	W (inch)	L (inch)	Rotation (deg)	dCp/dX (per ft)
27b	7.5	-	-	-	-	-	-	-	-	-	18.000	-	0
28	10.5	3.00	2.895	300	0.148	1.1	2.4	14.0	0.163	0.391	2.279	0	0
29	10.5	3.00	2.895	300	0.148	1.1	2.4	17.0	0.163	0.391	2.768	0	0
30	10.5	3.00	2.895	300	0.148	1.1	2.4	20.0	0.163	0.391	3.256	0	0
31	10.5	3.00	2.895	300	0.148	1.1	2.4	25.0	0.163	0.391	4.070	0	0
32	10.5	3.00	2.895	300	0.148	1.1	2.4	30.0	0.163	0.391	4.884	0	0
33	10.5	3.00	2.895	300	0.148	1.1	2.4	20.0	0.163	0.391	3.256	15	0
34	10.5	3.00	2.895	300	0.148	1.1	2.4	20.0	0.163	0.391	3.256	30	0
35	10.5	3.00	2.895	300	0.148	1.1	2.4	20.0	0.163	0.391	3.256	45	0
36	10.5	3.00	2.895	300	0.148	2.4	2.4	14.0	0.354	0.849	4.952	0	0
37	10.5	3.00	2.895	300	0.148	2.4	2.4	17.0	0.354	0.849	6.013	0	0
38	10.5	3.00	2.895	300	0.148	2.4	2.4	20.0	0.354	0.849	7.074	0	0
39	10.5	3.00	2.895	300	0.148	2.4	2.4	25.0	0.354	0.849	8.843	0	0
40	10.5	3.00	2.895	300	0.148	2.4	2.4	30.0	0.354	0.849	10.612	0	0
41	18.0	10.50	2.895	500	0.139	1.1	2.4	14.0	0.153	0.367	2.143	0	0
42	18.0	10.50	2.895	500	0.139	1.1	2.4	17.0	0.153	0.367	2.602	0	0
43	18.0	10.50	2.895	500	0.139	1.1	2.4	20.0	0.153	0.367	3.061	0	0
44	18.0	10.50	2.895	500	0.139	1.1	2.4	25.0	0.153	0.367	3.826	0	0
45	10.5	3.00	2.895	300	0.148	1.1	2.4	20.0	0.163	0.391	3.256	0	-0.005
46	10.5	3.00	2.895	300	0.148	1.1	2.4	20.0	0.163	0.391	3.256	0	0.005
47	10.5	3.00	2.895	300	0.148	1.1	2.4	20.0	0.163	0.391	3.256	0	0.011
48	18.0	10.50	2.895	500	0.139	2.4	2.4	14.0	0.333	0.798	4.655	0	0
49	18.0	10.50	2.895	500	0.139	2.4	2.4	17.0	0.333	0.798	5.653	0	0
50	18.0	10.50	2.895	500	0.139	2.4	2.4	20.0	0.333	0.798	6.650	0	0

Table 5.- Test matrix for Test 6857 - Oil flow runs.

Run	Config.	$\alpha$ (deg)	$Re_{\infty} \times 10^{-6}$ (ft <sup>-1</sup> )	X, cavity (inch)	$M_e$	$Re_{\theta}$	$\delta$ (inch)	H/ $\delta$	W/H	L/H	Rot (deg)	BL State	Objective
13	1	0	1		2.895							L	Baseline
14	1	-5	1		2.569							L	Baseline
15	1	-5	1		2.569							L	Baseline
16	1	3	1		3.100							L	Baseline
17	1	0	4		2.895							L	Baseline
18	1	0	4		2.895							L	Baseline
19	3	0	1	14.358	2.895	241	0.305	1.76	1.33	8.0	0	L	Large H/ $\delta$
20	17		1	8.653	2.830	205	0.240	1.10	2.40	14.0	0	L	W/H, L/H
21	16	0	1	8.653	2.895	205	0.240	1.10	1.20	14.0	0	L	W/H, L/H
22	18	0	1	8.653	2.895	205	0.240	1.10	3.60	14.0	0	L	W/H, L/H
23	8	0	1	9.550	2.895	205	0.240	1.10	2.40	7.2	0	L	Mid-Range H/ $\delta$
24	15	0	1	9.550	2.895	205	0.240	1.10	2.40	7.2	90	L	Rotation
26	11	0	1	9.550	2.895	205	0.240	1.10	2.40	7.2	10	L	Rotation
27	19	0	1	8.257	2.895	205	0.240	1.10	2.40	17.0	0	L	W/H, L/H



Table 6.- Test matrix for Test 6857 - Baseline model heating runs.

Run	Config.	$\alpha$ (deg)	$Re_{\infty} \times 10^{-6}$ (ft <sup>-1</sup> )	X0, cavity (inch)	$M_e$	$Re_{\theta}$	$\delta$ (inch)	H/ $\delta$	W/H	L/H	Rot (deg)	BL State	Objective
28	1	0	4		2.895							L	Baseline
29	1	0	4		2.895							L	Baseline
30	1	0	2		2.895							L	Baseline
31	1	0	2		2.895							L	Baseline
32	1	0	2		2.895							L	Baseline
33	1	0	2		2.895							L	Baseline
34	1	0	2		2.895							L	Baseline
35	1	0	2		2.895							L	Baseline
36	1	0	2		2.895							L	Baseline
37	1	0	2		2.895							L	Baseline
38	1	0	1		2.895							L	Baseline

Table 7.- Test matrix for Test 6857 - Cavity heating runs.

Run	Config.	$\alpha$ (deg)	$Re_{\infty} \times 10^{-6}$ (ft <sup>-1</sup> )	X0, cavity (inch)	$M_e$	$Re_{\theta}$	$\delta$ (inch)	H/ $\delta$	W/H	L/H	Rot (deg)	BL State	Objective
42	3-Gouge	0	4	14.358	2.895	461	0.159	3.37	1.33	8.0	0	L	Gouge
43	3-Gouge	0	2	14.358	2.895	337	0.220	2.43	1.33	8.0	0	L	Gouge
44	3-Gouge	0	1	14.358	2.895	241	0.305	1.76	1.33	8.0	0	L	Gouge
45	3-Gouge	0	0.5	14.358	2.895	193	0.348	1.54	1.33	8.0	0	L	Gouge
46	3	0	0.5	14.358	2.895	193	0.348	1.54	1.33	8.0	0	L	Large H/d
47	3	0	1	14.358	2.895	241	0.305	1.76	1.33	8.0	0	L	Large H/d
48	3	0	2	14.358	2.895	337	.220	2.43	1.33	8.0	0	L	Large H/d
49	3	0	4	14.358	2.895	461	0.159	3.37	1.33	8.0	0	L	Large H/d

Table 7.- Test matrix for Test 6857 - Cavity heating runs (continued).

Run	Config.	$\alpha$ (deg)	$Re_{\infty} \times 10^{-6}$ (ft <sup>-1</sup> )	X0, cavity (inch)	$M_e$	$Re_{\theta}$	$\delta$ (inch)	H/ $\delta$	W/H	L/H	Rot (deg)	BL State	Objective
50	3-Gap	0	1	14.358	2.895	241	0.305	1.76	1.33	8.0	0	L	Filler Gaps
51	3-Gap	0	2	14.358	2.895	337	0.220	2.43	1.33	8.0	0	L	Filler Gaps
52	3-Gap	0	4	14.358	2.895	461	0.159	3.37	1.33	8.0	0	L	Filler Gaps
57	3-Gap	0	1	14.358	2.895	241	0.305	1.76	1.33	8.0	0	L	Filler Gaps
58	3-Gap	0	2	14.358	2.895	337	0.220	2.43	1.33	8.0	0	L	Filler Gaps
95f	3-Gap	-5	2	14.358	2.569	337	0.220	2.43	1.33	8.0	0	L	Filler Gaps
96f	3-Gap	0	2	14.358	2.895	337	0.220	2.43	1.33	8.0	0	L	Filler Gaps
59	3-Gap	0	4	14.358	2.895	461	0.159	3.37	1.33	8.0	0	L	Filler Gaps
93f	3-Gap	0	4	14.358	2.895	461	0.159	3.37	1.33	8.0	0	L	Filler Gaps
94f	3-Gap	-5	4	14.358	2.569	461	0.159	3.37	1.33	8.0	0	L	Filler Gaps
60	5	0	1	15.383	2.895	241	0.305	0.92	1.33	8.0	0	L	Large H/d
61	5	0	2	15.383	2.895	337	0.220	1.27	1.33	8.0	0	L	Large H/d
62	5	0	4	15.383	2.895	461	0.159	1.76	1.33	8.0	0	L	Large H/d
101f	3-Slot	0	0	14.358	0	0	0.159	3.37	1.33	8.0	0	L	No Flow
102f	3-Slot	0	1	14.358	2.895	241	0.305	1.76	1.33	8.0	0	L	No Suction
103f	3-Slot	0	1	14.358	2.895	241	0.305	1.76	1.33	8.0	0	L	Suction
106f	3-Slot	0	4	14.358	2.895	461	0.159	3.37	1.33	8.0	0	L	No Suction
105f	3-Slot	-5	4	14.358	2.569	461	0.159	3.37	1.33	8.0	0	L	No Suction
104f	3-Slot	-5	4	14.358	2.569	461	0.159	3.37	1.33	8.0	0	L	Suction
53	16	0	1	8.653	2.895	205	0.240	1.10	1.20	14.0	0	L	W/H, L/H
54	16	0	4	8.653	2.895	394	0.125	2.11	1.20	14.0	0	L	W/H, L/H
88f	16	-5	4	8.653	2.569	394	0.125	2.11	1.20	14.0	0	L	W/H, L/H

Table 7.- Test matrix for Test 6857 - Cavity heating runs (continued).

Run	Config.	$\alpha$ (deg)	$Re_{\infty} \times 10^{-6}$ (ft <sup>-1</sup> )	X0, cavity (inch)	$M_e$	$Re_{\theta}$	$\delta$ (inch)	H/ $\delta$	W/H	L/H	Rot (deg)	BL State	Objective
89f	16	-3	4	8.653	2.690	394	0.125	2.11	1.20	14.0	0	L	W/H, L/H
90f	16	-1	4	8.653	2.830	394	0.125	2.11	1.20	14.0	0	L	W/H, L/H
91f	16	0	4	8.653	2.895	394	0.125	2.11	1.20	14.0	0	L	W/H, L/H
55	16	0	2	8.653	2.895	288	0.173	1.53	1.20	14.0	0	L	W/H, L/H
92f	16	0	2	8.653	2.895	288	0.173	1.53	1.20	14.0	0	L	W/H, L/H
56	16	0	0.5	8.653	2.895	164	0.274	0.96	1.20	14.0	0	L	W/H, L/H
66	17	0	1	8.653	2.895	205	0.240	1.10	2.40	14.0	0	L	W/H, L/H
67	17	0	2	8.653	2.895	288	0.173	1.53	2.40	14.0	0	L	W/H, L/H
68	17	0	4	8.653	2.895	394	0.125	2.11	2.40	14.0	0	L	W/H, L/H
81f	17	0	4	8.653	2.895	394	0.125	2.11	2.40	14.0	0	L	W/H, L/H
69	18	0	1	8.653	2.895	205	0.240	1.10	3.60	14.0	0	L	W/H, L/H
70	18	0	2	8.653	2.895	288	0.173	1.53	3.60	14.0	0	L	W/H, L/H
71	18	0	4	8.653	2.895	394	0.125	2.11	3.60	14.0	0	L	W/H, L/H
82f	18	0	4	8.653	2.895	394	0.125	2.11	3.60	14.0	0	L	W/H, L/H
83f	18	-1	4	8.653	2.830	394	0.125	2.11	3.60	14.0	0	L	W/H, L/H
84f	18	-1	4	8.653	2.830	394	0.125	2.11	3.60	14.0	0	L	W/H, L/H
85f	18	1	4	8.653	2.960	394	0.125	2.11	3.60	14.0	0	L	W/H, L/H
87f	18	5	4	8.653	2.569	394	0.125	2.11	3.60	14.0	0	L	W/H, L/H
86f	18	-3	4	8.653	2.690	394	0.125	2.11	3.60	14.0	0	L	W/H, L/H
72	19	0	1	8.653	2.895	205	0.240	1.10	2.40	17.0	0	L	W/H, L/H
73	19	0	2	8.653	2.895	288	0.173	1.53	2.40	17.0	0	L	W/H, L/H

Table 7.- Test matrix for Test 6857 - Cavity heating runs (Concluded).

Run	Config.	$\alpha$ (deg)	$Re_{\infty} \times 10^{-6}$ (ft <sup>-1</sup> )	X0, cavity (inch)	$M_e$	$Re_{\theta}$	$\delta$ (inch)	H/ $\delta$	W/H	L/H	Rot (deg)	BL State	Objective
80f	19	0	2	8.653	2.895	288	0.173	1.53	2.40	17.0	0	L	W/H, L/H
74	19	0	4	8.653	2.895	394	0.125	2.11	2.40	17.0	0	L	W/H, L/H
79f	19	0	4	8.653	2.895	394	0.125	2.11	2.40	17.0	0	L	W/H, L/H
75	8	0	1	9.550	2.895	205	0.240	1.10	2.40	7.2	0	L	Mid-Range H/d
76	8	0	2	9.550	2.895	288	0.173	1.53	2.40	7.2	0	L	Mid-Range H/d
77	8	0	4	9.550	2.895	394	0.125	2.11	2.40	7.2	0	L	Mid-Range H/d
78f	8	0	4	9.550	2.895	394	0.125	2.11	2.40	7.2	0	L	Mid-Range H/d
63	11	0	1	9.550	2.895	205	0.240	1.10	2.40	7.2	10	L	Rotation
64	11	0	2	9.550	2.895	288	0.173	1.53	2.40	7.2	10	L	Rotation
65	11	0	4	9.550	2.895	394	0.125	2.11	2.40	7.2	10	L	Rotation

**Table 8.- Test matrix for Test 6868 – Baseline model heating runs.**

Run	Config.	$\alpha$ (deg)	$Re_{\infty} \times 10^{-6}$ (ft <sup>-1</sup> )	X0, cavity (inch)	$M_e$	$Re_{\theta}$	$\delta$ (inch)	H/ $\delta$	W/H	L/H	Rot (deg)	BL State	Objective
22	27	-10	4	7.5	2.245			0	0	0	0	L	Baseline
23	27	0	2	7.5	2.895			0	0	0	0	L	Baseline
24	27	0	4	7.5	2.895			0	0	0	0	L	Baseline
26	27	0	1	7.5	2.895			0	0	0	0	L	Baseline
27	27	-10	1	7.5	2.245			0	0	0	0	L	Baseline
28	27	-10	2	7.5	2.245			0	0	0	0	L	Baseline
30	27	-10	0.5	7.5	2.245			0	0	0	0	L	Baseline
31	27	0	0.5	7.5	2.895			0	0	0	0	L	Baseline
152	27	0	8	7.5	2.895			0	0	0	0	L	Baseline

**Table 9.- Test matrix for Test 6868 - Cavity heating runs.**

Run	Config.	$\alpha$ (deg)	$Re_{\infty} \times 10^{-6}$ (ft <sup>-1</sup> )	X0, cavity (inch)	$M_e$	$Re_{\theta}$	$\delta$ (inch)	H/ $\delta$	W/H	L/H	Rot (deg)	BL State	Objective
17	5	0	2	14.88	2.895	346	0.178	1.6	1.3	8	0	L	Short Cavity
131f	9s	0	2	9.82	2.895	288	0.148	1.3	2.4	7.2	0	L	Short Cavity
132f	9s	-10	2	9.82	2.245	368	0.094	2.0	2.4	7.2	0	L	Short Cavity
133f	9s	-10	4	9.82	2.227	503	0.068	2.8	2.4	7.2	0	L	Short Cavity
49	28	0	2	10.5	2.895	300	0.148	1.1	2.4	14	0	L	Cavity Length
140f	28	0	2	10.5	2.895	300	0.148	1.1	2.4	14	0	L	Cavity Length
53	29	0	2	10.5	2.895	300	0.148	1.1	2.4	17	0	L	Cavity Length
71	30	0	2	10.5	2.895	300	0.148	1.1	2.4	20	0	L	Cavity Length
83	30	0	2	10.5	2.895	300	0.148	1.1	2.4	20	0	L	Cavity Length
103	30	0	2	10.5	2.895	300	0.148	1.1	2.4	20	0	L	Cavity Length
124f	30	0	2	10.5	2.895	300	0.148	1.1	2.4	20	0	L	SLA vs. Ceramic
42	31	0	2	10.5	2.895	300	0.148	1.1	2.4	25	0	L	Cavity Length
66	32	0	2	10.5	2.895	300	0.148	1.1	2.4	30	0	L	Cavity Length
128f	32	0	2	10.5	2.895	300	0.148	1.1	2.4	30	0	L	Cavity Length
77	36	0	2	10.5	2.895	300	0.148	2.4	2.4	14	0	L	Cavity Length
99	37	0	2	10.5	2.895	300	0.148	2.4	2.4	17	0	L	Cavity Length
108	38	0	2	10.5	2.895	300	0.148	2.4	2.4	20	0	L	Cavity Length
146f	38	0	2	10.5	2.895	300	0.148	2.4	2.4	20	0	L	Cavity Length
94	39	0	2	10.5	2.895	300	0.148	2.4	2.4	25	0	L	Cavity Length
115f	40	0	2	10.5	2.895	300	0.148	2.4	2.4	30	0	L	Cavity Length
58	41	0	4	18	2.895	500	0.139	1.1	2.4	14	0	L	Cavity Length

Table 9.- Test matrix for Test 6868 - Cavity heating runs (Continued).

Run	Config.	$\alpha$ (deg)	$Re_{\infty} \times 10^{-6}$ (ft <sup>-1</sup> )	X0, cavity (inch)	$M_e$	$Re_{\theta}$	$\delta$ (inch)	H/ $\delta$	W/H	L/H	Rot (deg)	BL State	Objective
74	42	0	4	18	2.895	500	0.139	1.1	2.4	17	0	L	Cavity Length
63	43	0	4	18	2.895	500	0.139	1.1	2.4	20	0	L	Cavity Length
151f	43	0	4	18	2.895	500	0.139	1.1	2.4	20	0	L	Cavity Length
111	44	0	4	18	2.895	500	0.139	1.1	2.4	25	0	L	Cavity Length
60	48	0	4	18	2.895	500	0.139	2.4	2.4	14	0	L	Cavity Length
68	49	0	4	18	2.895	500	0.139	2.4	2.4	17	0	L	Cavity Length
80	50	0	4	18	2.895	500	0.139	2.4	2.4	20	0	L	Cavity Length
147f	50	0	4	18	2.895	500	0.139	2.4	2.4	20	0	L	Cavity Length
51	28	-10	4	10.5	2.245	503	0.068	2.4	2.4	14	0	L	Deep Cavity
142f	28	-10	4	10.5	2.245	503	0.068	2.4	2.4	14	0	L	Deep Cavity
52	29	-10	4	10.5	2.245	503	0.068	2.4	2.4	17	0	L	Deep Cavity
72	30	-10	4	10.5	2.245	503	0.068	2.4	2.4	20	0	L	Deep Cavity
84	30	-10	4	10.5	2.245	503	0.068	2.4	2.4	20	0	L	Deep Cavity
105	30	-10	4	10.5	2.245	503	0.068	2.4	2.4	20	0	L	Deep Cavity
126f	30	-10	4	10.5	2.245	503	0.068	2.4	2.4	20	0	L	Deep Cavity
41	31	-10	4	10.5	2.245	503	0.068	2.4	2.4	25	0	L	Deep Cavity
67	32	-10	4	10.5	2.245	503	0.068	2.4	2.4	30	0	L	Deep Cavity
127f	32	-10	4	10.5	2.245	503	0.068	2.4	2.4	30	0	L	Deep Cavity
78	36	-10	4	10.5	2.245	503	0.068	5.2	2.4	14	0	L	Deep Cavity
102	37	-10	4	10.5	2.245	503	0.068	5.2	2.4	17	0	L	Deep Cavity
107	38	-10	4	10.5	2.245	503	0.068	5.2	2.4	20	0	L	Deep Cavity
144f	38	-10	4	10.5	2.245	503	0.068	5.2	2.4	20	0	L	Deep Cavity



Table 9.- Test matrix for Test 6868 - Cavity heating runs (Concluded).

Run	Config.	$\alpha$ (deg)	$Re_{\infty} \times 10^{-6}$ (ft <sup>-1</sup> )	X0, cavity (inch)	$M_e$	$Re_{\theta}$	$\delta$ (inch)	H/ $\delta$	W/H	L/H	Rot (deg)	BL State	Objective
98	39	-10	4	10.5	2.245	503	0.068	5.2	2.4	25	0	L	Deep Cavity
113f	40	-10	4	10.5	2.245	503	0.068	5.2	2.4	30	0	L	Deep Cavity
79	36	-10	2.18	10.5	2.228	351	0.0883	4.0	2.4	14	0	L	Deep Cavity
101	37	-10	2.11	10.5	2.244	346	0.0883	4.0	2.4	17	0	L	Deep Cavity
106	38	-10	2.11	10.5	2.238	345	0.0897	3.9	2.4	20	0	L	Deep Cavity
143f	38	-10	2.11	10.5	2.238	345	0.0897	3.9	2.4	20	0	L	Deep Cavity
96	39	-10	2.11	10.5	2.226	347	0.089	4.0	2.4	25	0	L	Deep Cavity
114f	40	-10	2.11	10.5	2.26	347	0.089	4.0	2.4	30	0	L	Deep Cavity
56	41	-10	0.5	18	2.245	260	0.236	0.6	2.4	14	0	L	Shallow Cavity
73	42	-10	0.5	18	2.245	260	0.236	0.6	2.4	17	0	L	Shallow Cavity
62	43	-10	0.5	18	2.245	260	0.236	0.6	2.4	20	0	L	Shallow Cavity
112	44	-10	0.5	18	2.245	260	0.236	0.6	2.4	25	0	L	Shallow Cavity

**Table 10.- Test matrix for Test 6868 - Pressure gradient effects on heating using SLA models.**

Run	Config.	$\alpha$ (deg)	$Re_{\infty} \times 10^{-6}$ (ft <sup>-1</sup> )	X0, cavity (inch)	$M_e$	$Re_{\theta}$	$\delta$ (inch)	H/ $\delta$	W/H	L/H	Rot (deg)	BL State	Objective dp/dx
35	45s	0	2	10.5	2.895	300	0.148	1.1	2.4	20	0	L	-0.005
37	46s	0	2	10.5	2.895	300	0.148	1.1	2.4	20	0	L	0.005
45	47s	0	2	10.5	2.895	300	0.148	1.1	2.4	20	0	L	0.011
36	45s	-10	4	10.5	2.245	503	0.068	2.4	2.4	20	0	L	-0.005
38	46s	-10	4	10.5	2.245	503	0.068	2.4	2.4	20	0	L	0.005
46	47s	-10	4	10.5	2.245	503	0.068	2.4	2.4	20	0	L	0.011

**Table 11.- Test matrix for Test 6868 - Cross-flow effect on heating using SLA models.**

Run	Config.	$\alpha$ (deg)	$Re_{\infty} \times 10^{-6}$ (ft <sup>-1</sup> )	X0, cavity (inch)	$Me$	$Re_{\theta}$	$\delta$ (inch)	H/ $\delta$	W/H	L/H	BL State	Objective Rotation (deg)
117	33s	0	2	10.5	2.895	300	0.148	1.1	2.4	20	L	15
135f	33s	0	2	10.5	2.895	300	0.148	1.1	2.4	20	L	15
121	34s	0	2	10.5	2.895	300	0.148	1.1	2.4	20	L	30
136f	34s	0	2	10.5	2.895	300	0.148	1.1	2.4	20	L	30
120	35s	0	2	10.5	2.895	300	0.148	1.1	2.4	20	L	45
139f	35s	0	2	10.5	2.895	300	0.148	1.1	2.4	20	L	45
118	33s	-10	4	10.5	2.245	503	0.068	2.4	2.4	20	L	15
134f	33s	-10	4	10.5	2.245	503	0.068	2.4	2.4	20	L	15
122	34s	-10	4	10.5	2.245	503	0.068	2.4	2.4	20	L	30
137f	34s	-10	4	10.5	2.245	503	0.068	2.4	2.4	20	L	30
119	35s	-10	4	10.5	2.245	503	0.068	2.4	2.4	20	L	45
138f	35s	-10	4	10.5	2.245	503	0.068	2.4	2.4	20	L	45

**Table 12.- Phosphor uncertainty estimates.**

Uncertainty Type	Bias Uncertainty Value	Precision Un- certainty Value
Initial model wall temperature	1.43 °C	1.0 °C
Model run wall temperature at reference location	1.93 °C	n/a
Model run wall temperature	3.36 °C	1.0 °C
Effective time	0.02 s	0.05 s
Thermal properties	5.9%	n/a

# Figures

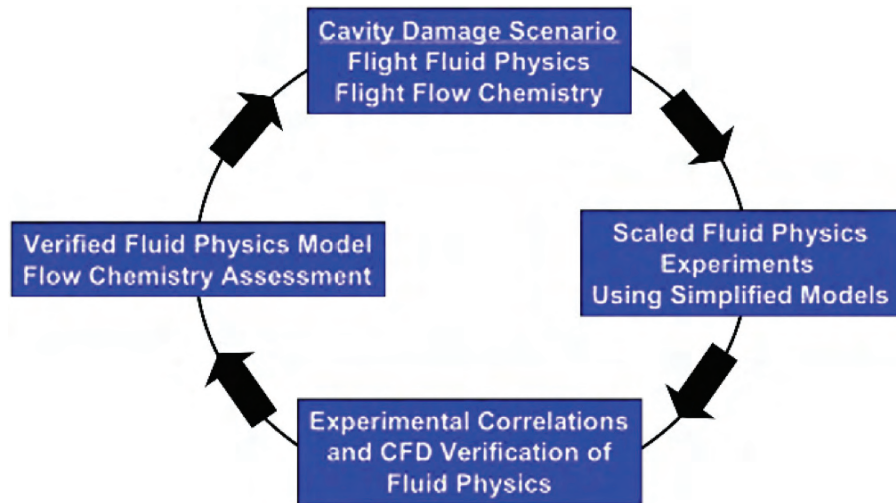


Figure 1.- Combined experimental and computational simulation approach.

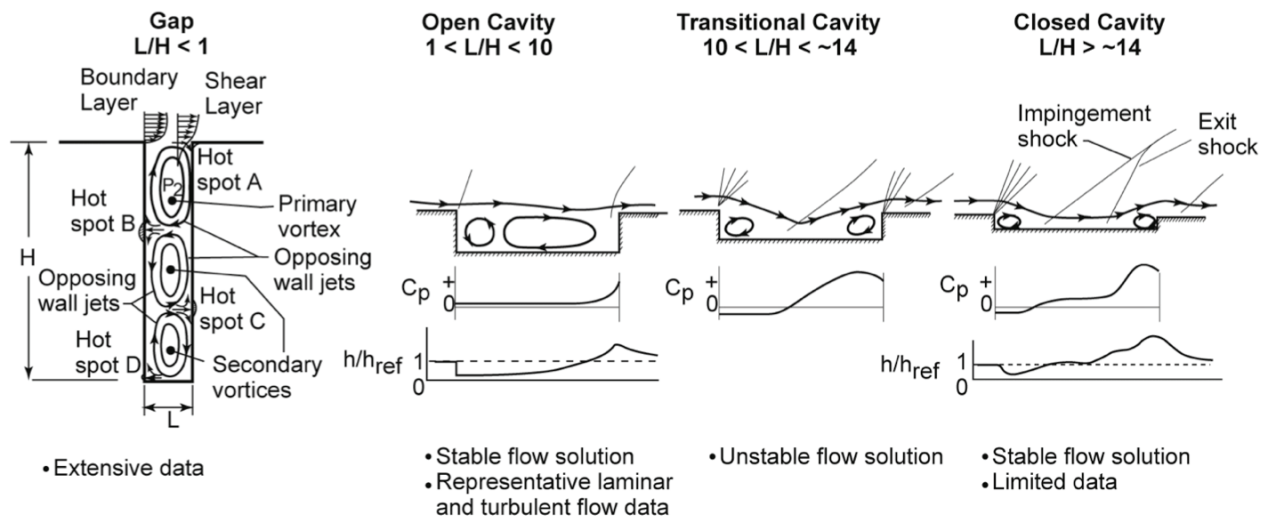


Figure 2.- Classification of supersonic/hypersonic cavity flows.

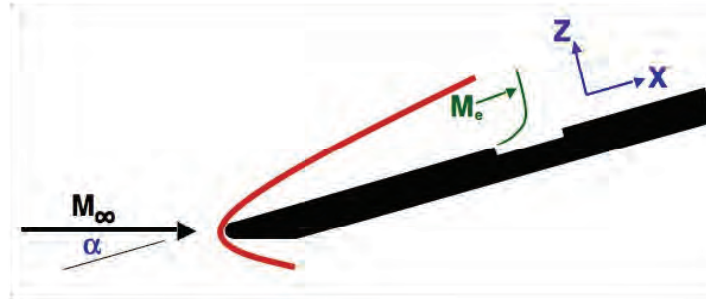


Figure 3.- Sketch of model coordinate system.

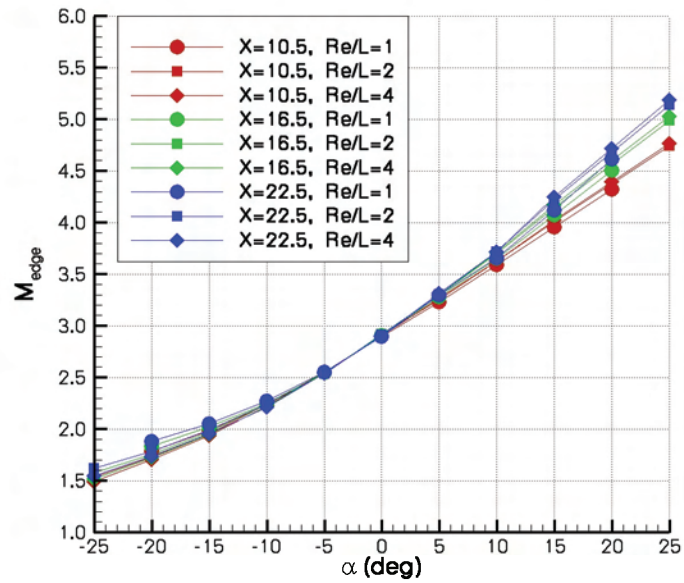


Figure 4.- LAURA predictions for  $M_e$  versus  $\alpha$  for baseline model.

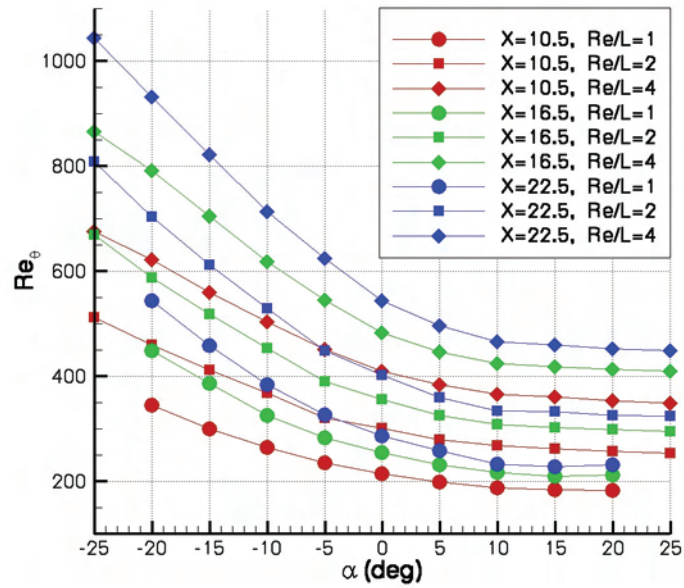


Figure 5.- LAURA predictions for  $Re_\theta$  versus  $\alpha$  for baseline model.

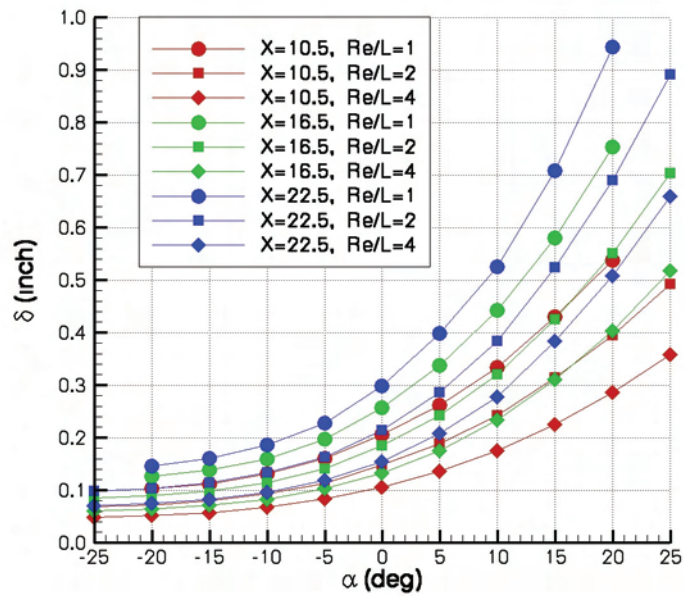
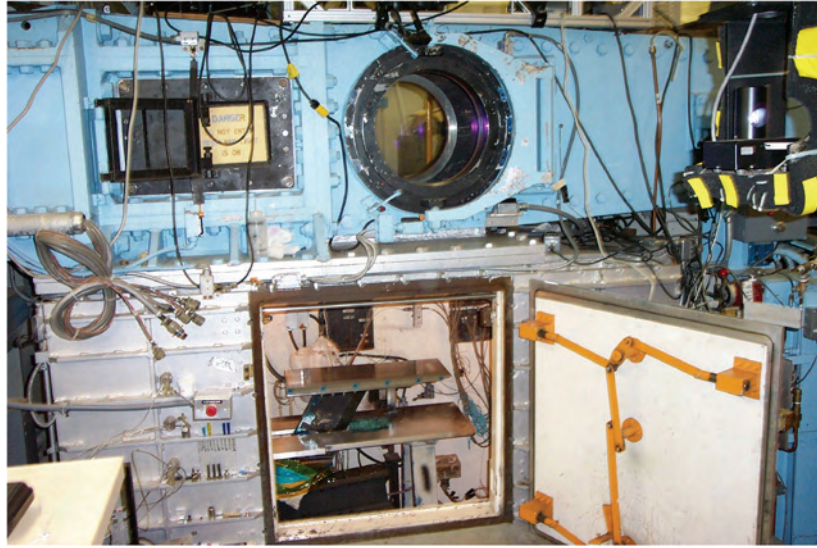
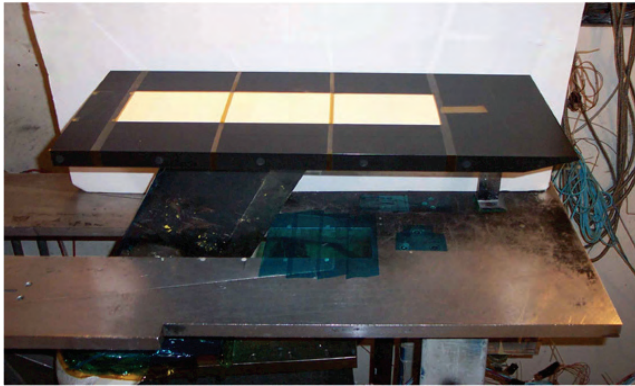


Figure 6.- LAURA predictions for boundary layer thickness for baseline model.



**Figure 7.- Langley 20-Inch Mach 6 Air Tunnel.**



**Figure 8.- Baseline model - 4-in. by 6-in. inserts used in Test 6857.**



**Figure 9.- Baseline model - 4-in. by 18-in. inserts used in Test 6868.**



a) Cavity model patterns were fabricated using stereolithographic array process (SLA).

b) Ceramic castings were fabricated using the SLA models and an aluminum mounting plate was bonded to the back side of the model

c) SLA patterns were spray painted black for oil flow visualizations (typical backside shown without mounting plate).

d) Ceramic castings were spray coated with thermographic phosphors and marked with fiducial indicators for wind tunnel testing.

**Figure 10.- Model fabrication process.**





Figure 11. – Cavity insert photographs for Test 6857.


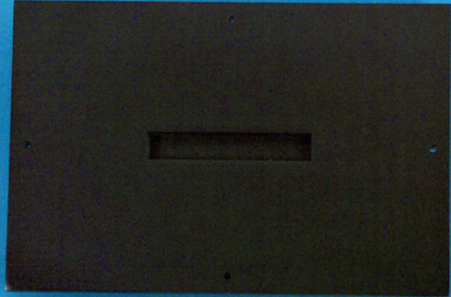
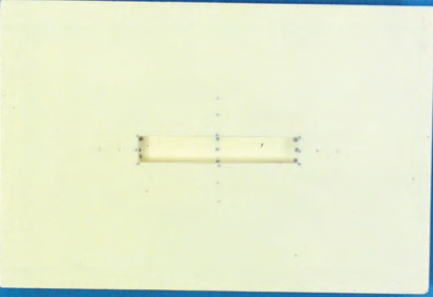

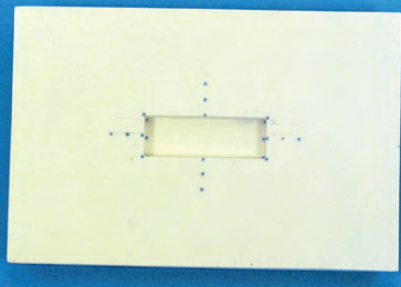
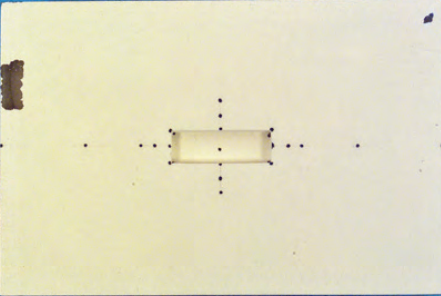
Config	View 1	View 2
4		
5		
8		
9	<p data-bbox="389 1459 706 1501"><i>No comparable model</i></p>	

Figure 11. – Cavity insert photographs for Test 6857 (Continued).

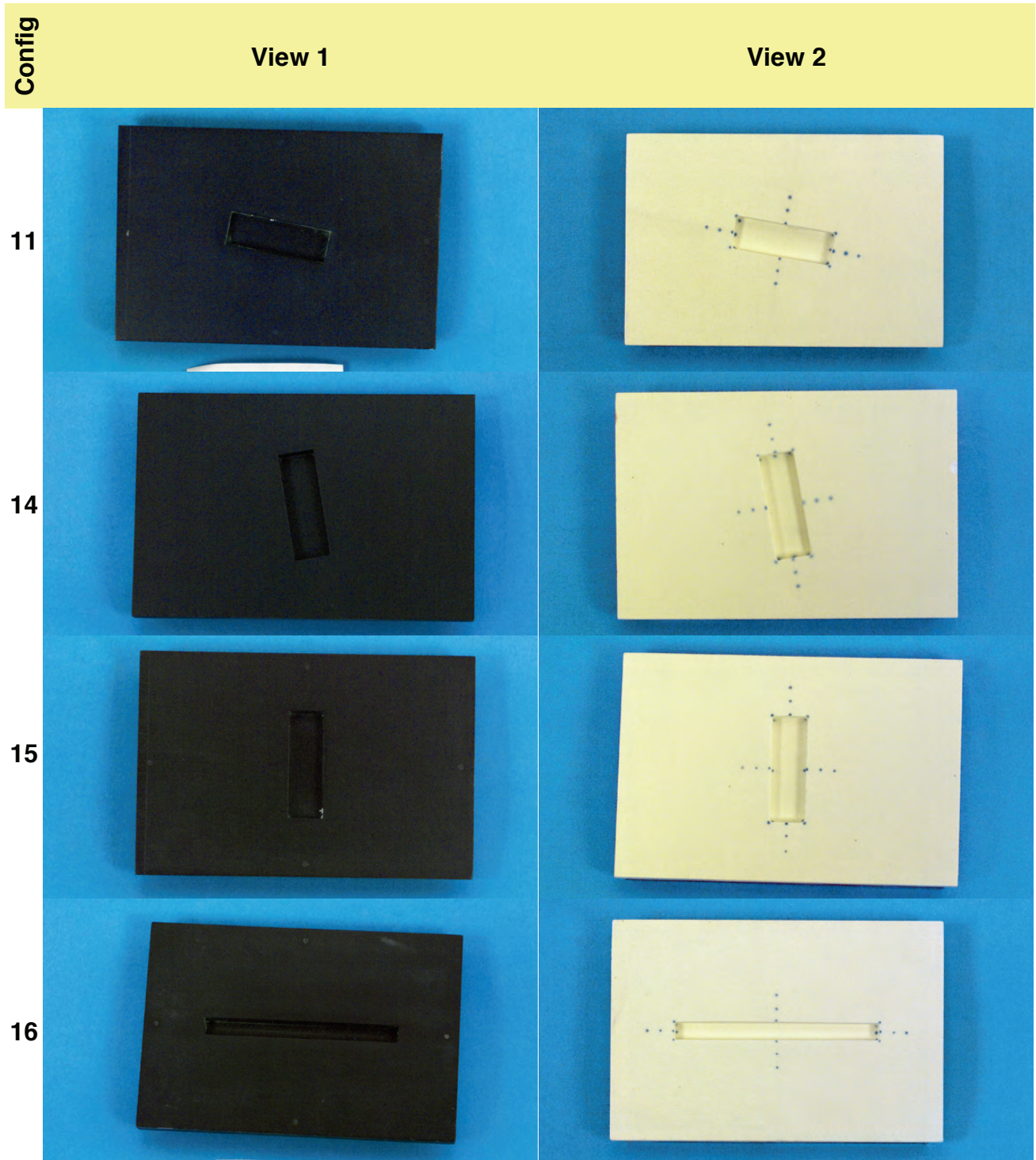


Figure 11. – Cavity insert photographs for Test 6857 (Continued).

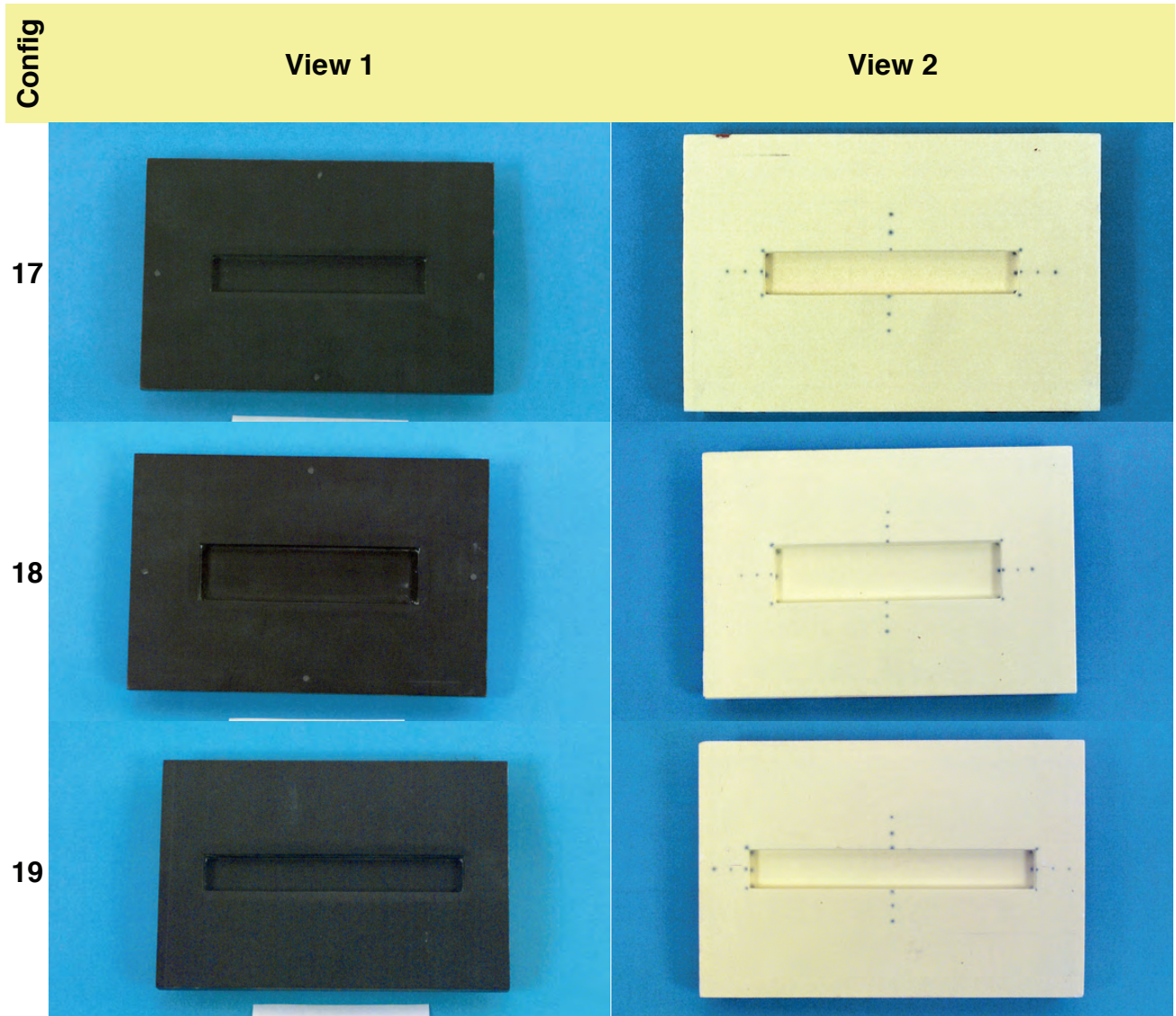


Figure 11. – Cavity insert photographs for Test 6857 (Concluded).

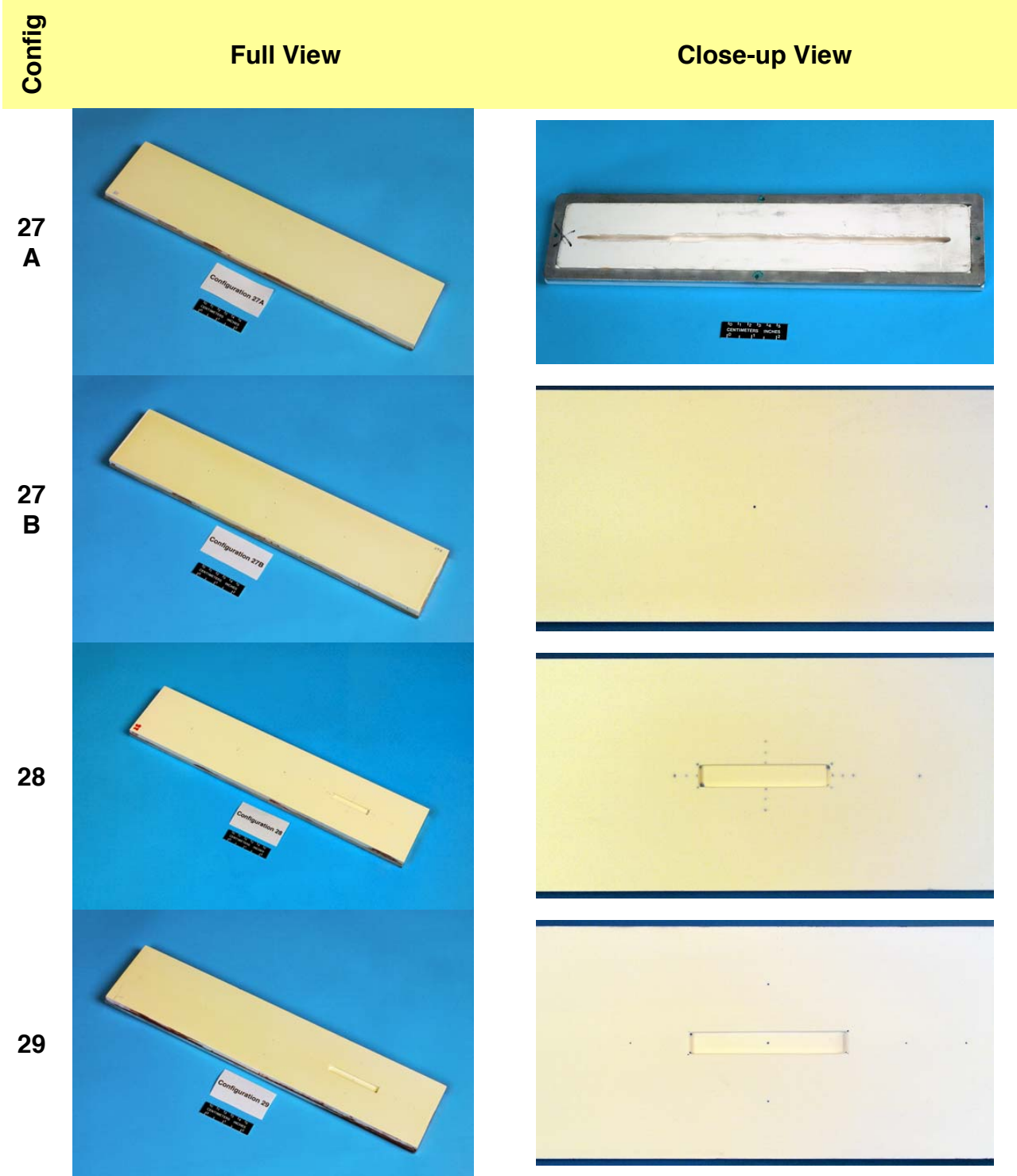


Figure 12. – Cavity insert model photographs for Test 6868.

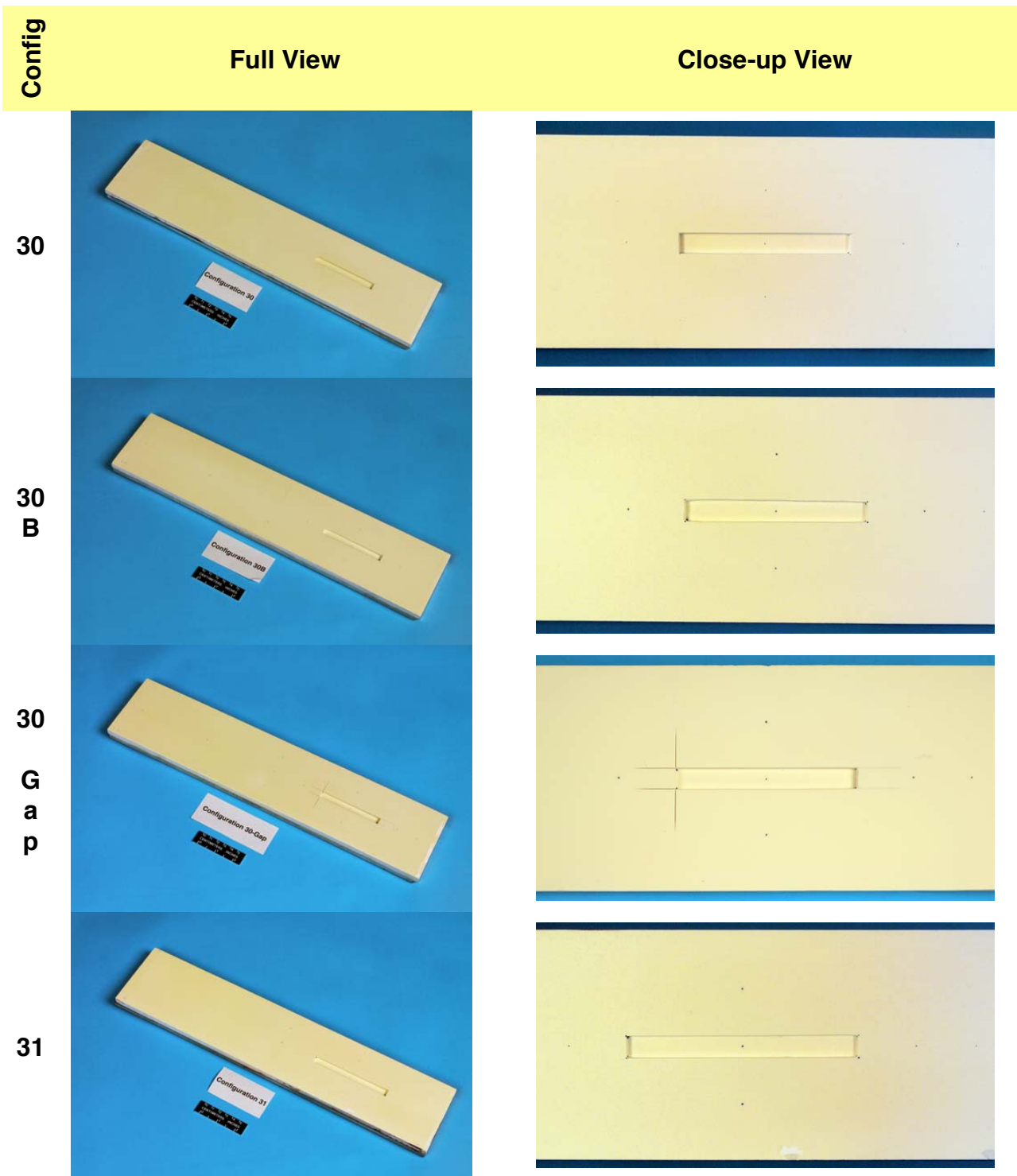


Figure 12. – Cavity insert model photographs for Test 6868 (Continued).

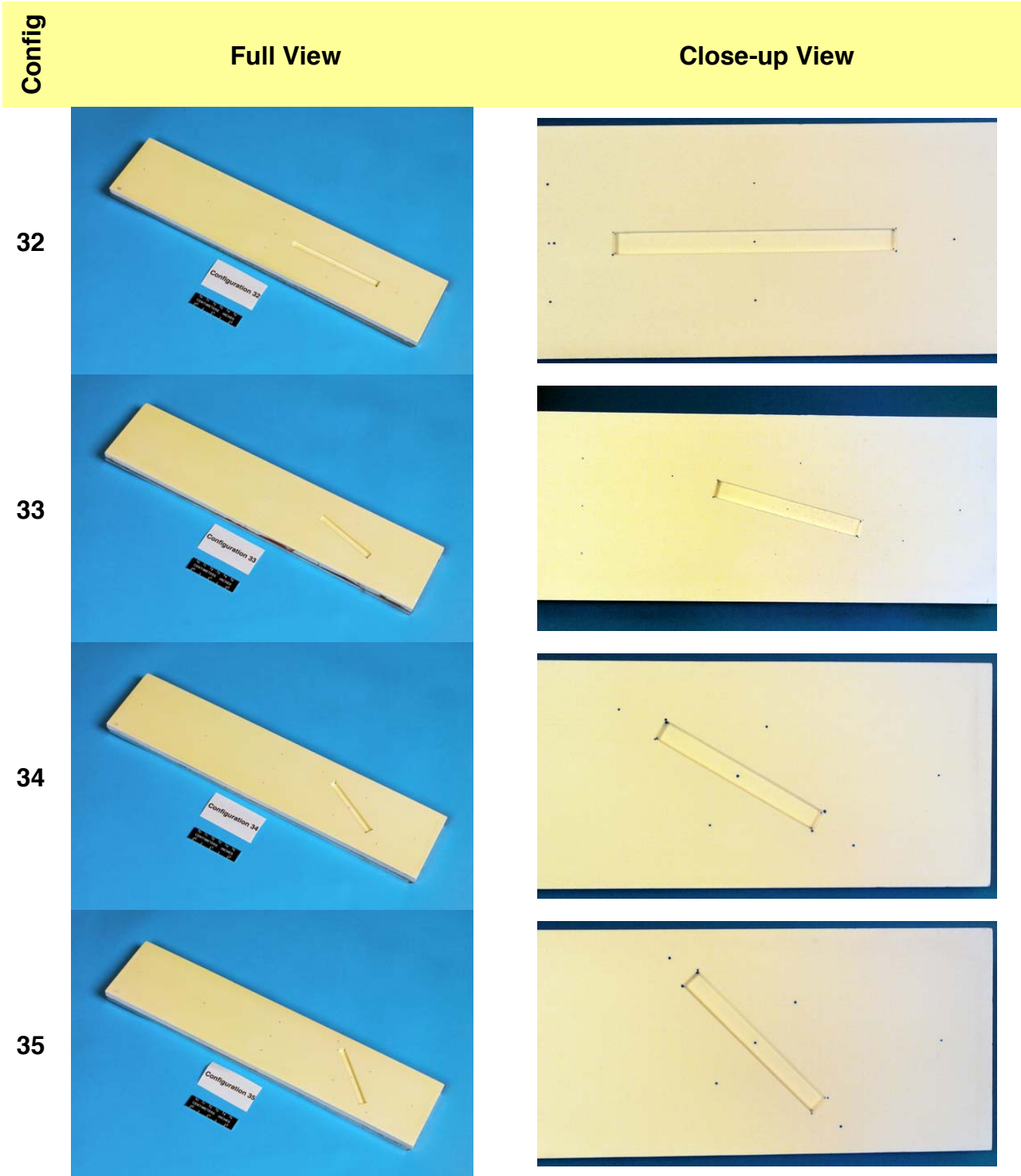


Figure 12. – Cavity insert model photographs for Test 6868 (Continued).


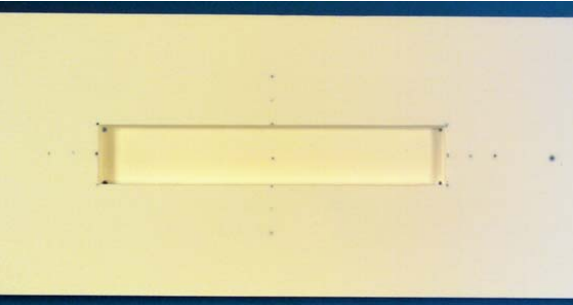

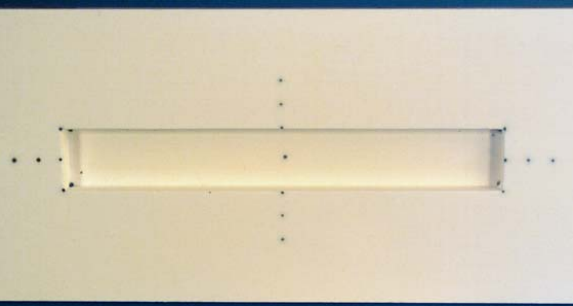
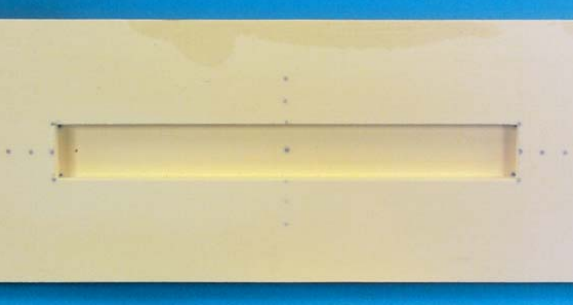


Config	Full View	Close-up View	
36	 <p>Configuration 36</p>		
37	 <p>Configuration 37</p>		
38	<i>Not available.</i>		
39	 <p>Configuration 39</p>		

Figure 12. – Cavity insert model photographs for Test 6868 (Continued).



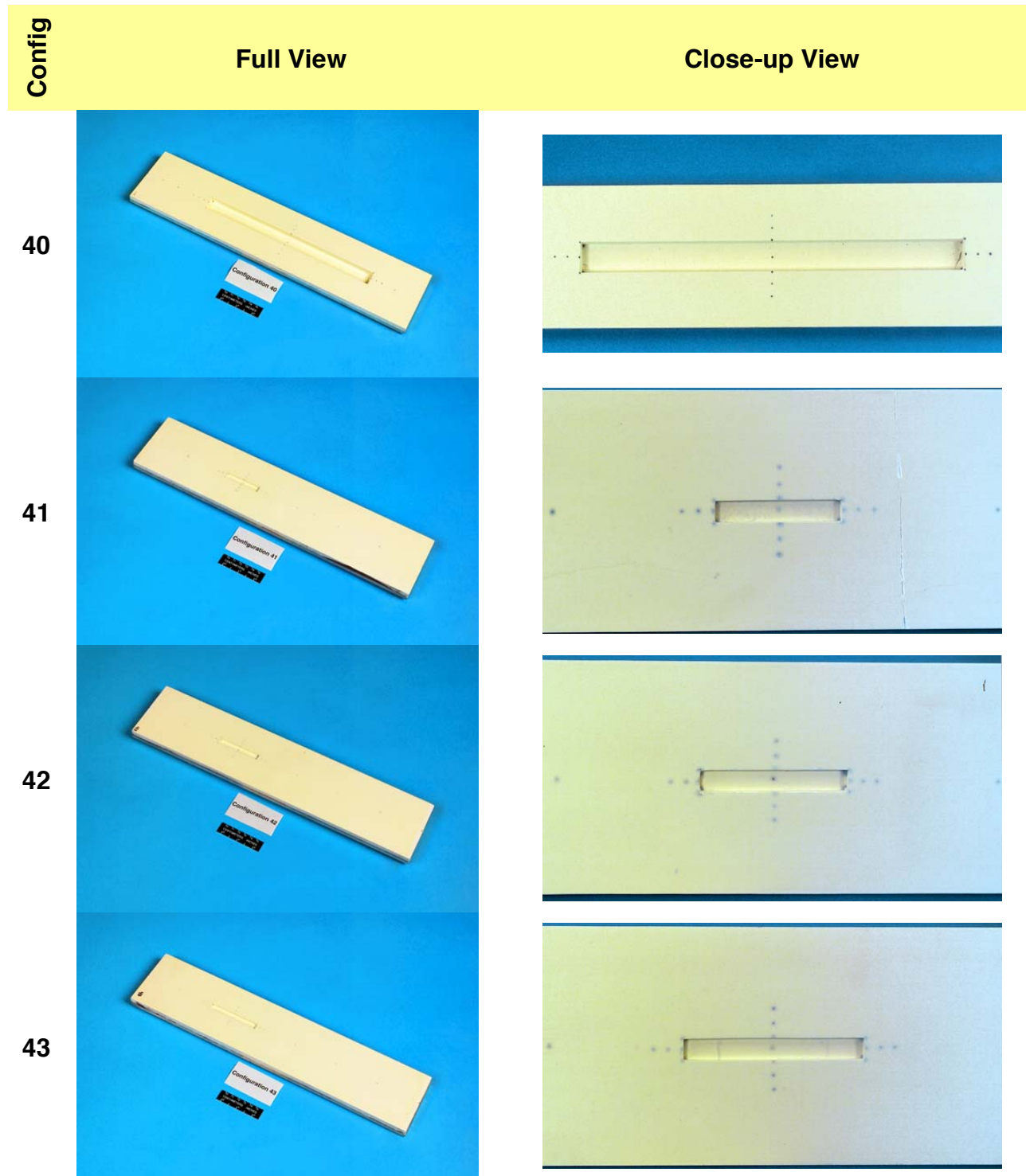


Figure 12. – Cavity insert model photographs for Test 6868 (Continued).

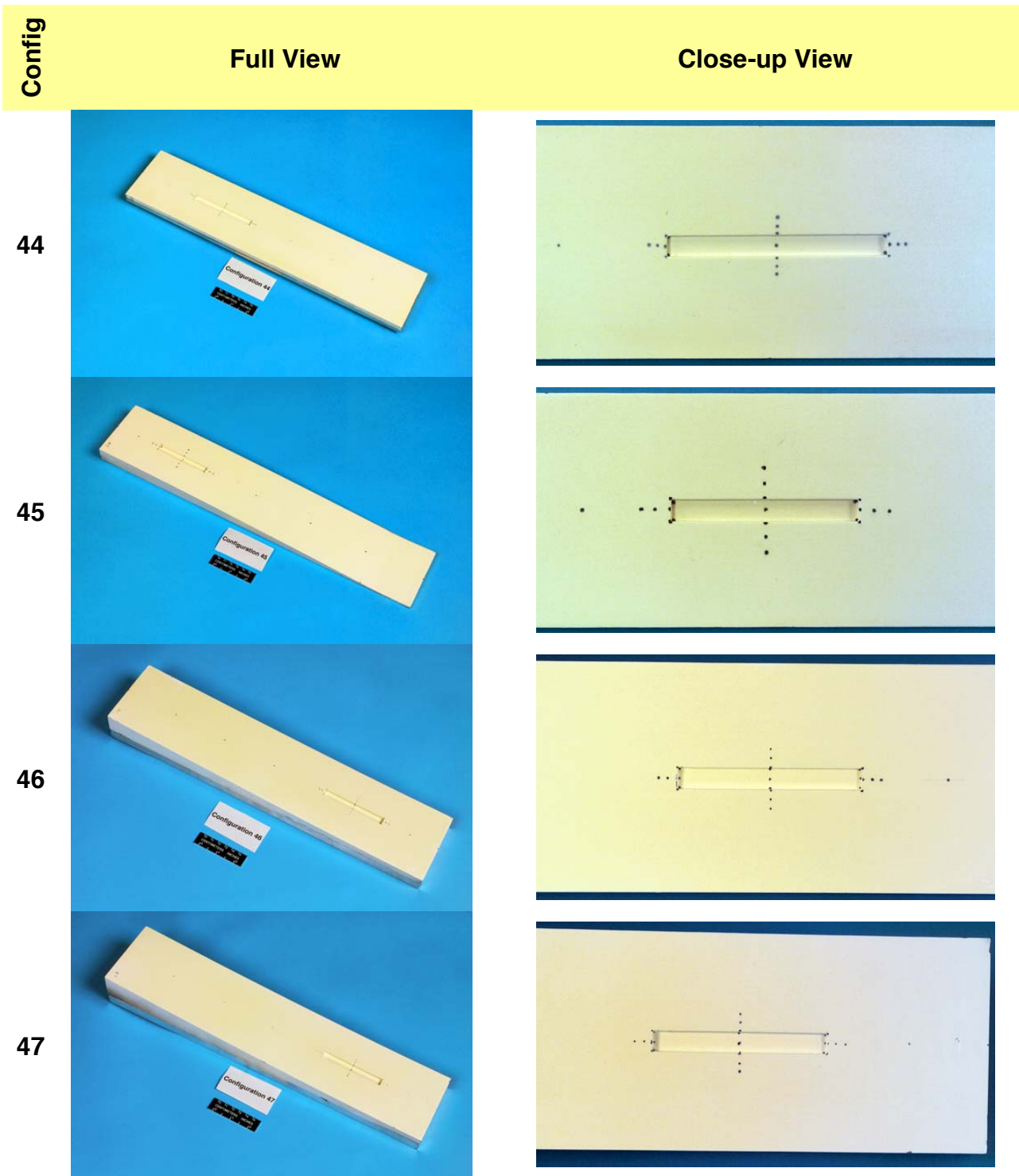


Figure 12. – Cavity insert model photographs for Test 6868 (Continued).

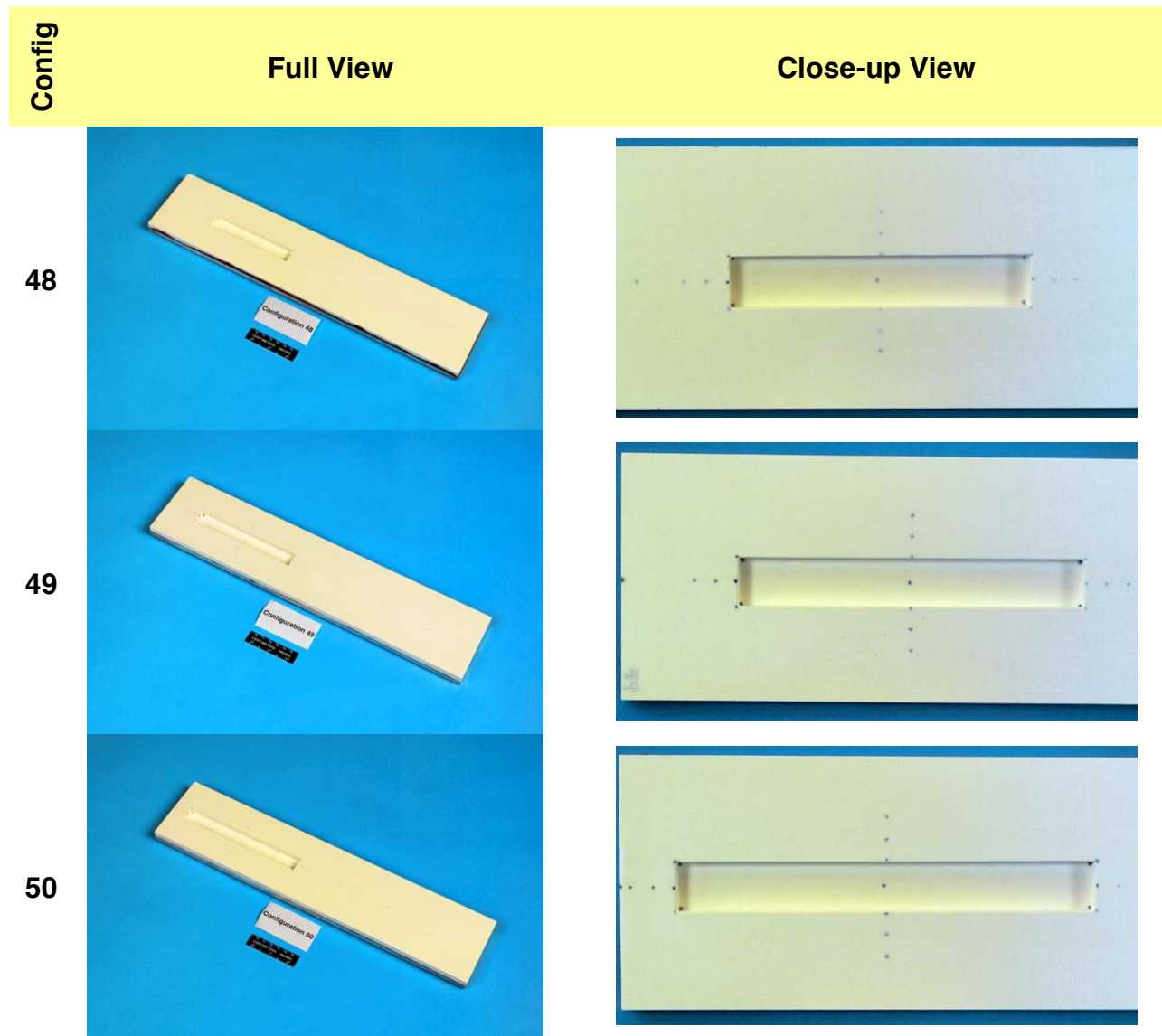


Figure 12. – Cavity insert model photographs for Test 6868 (Concluded).

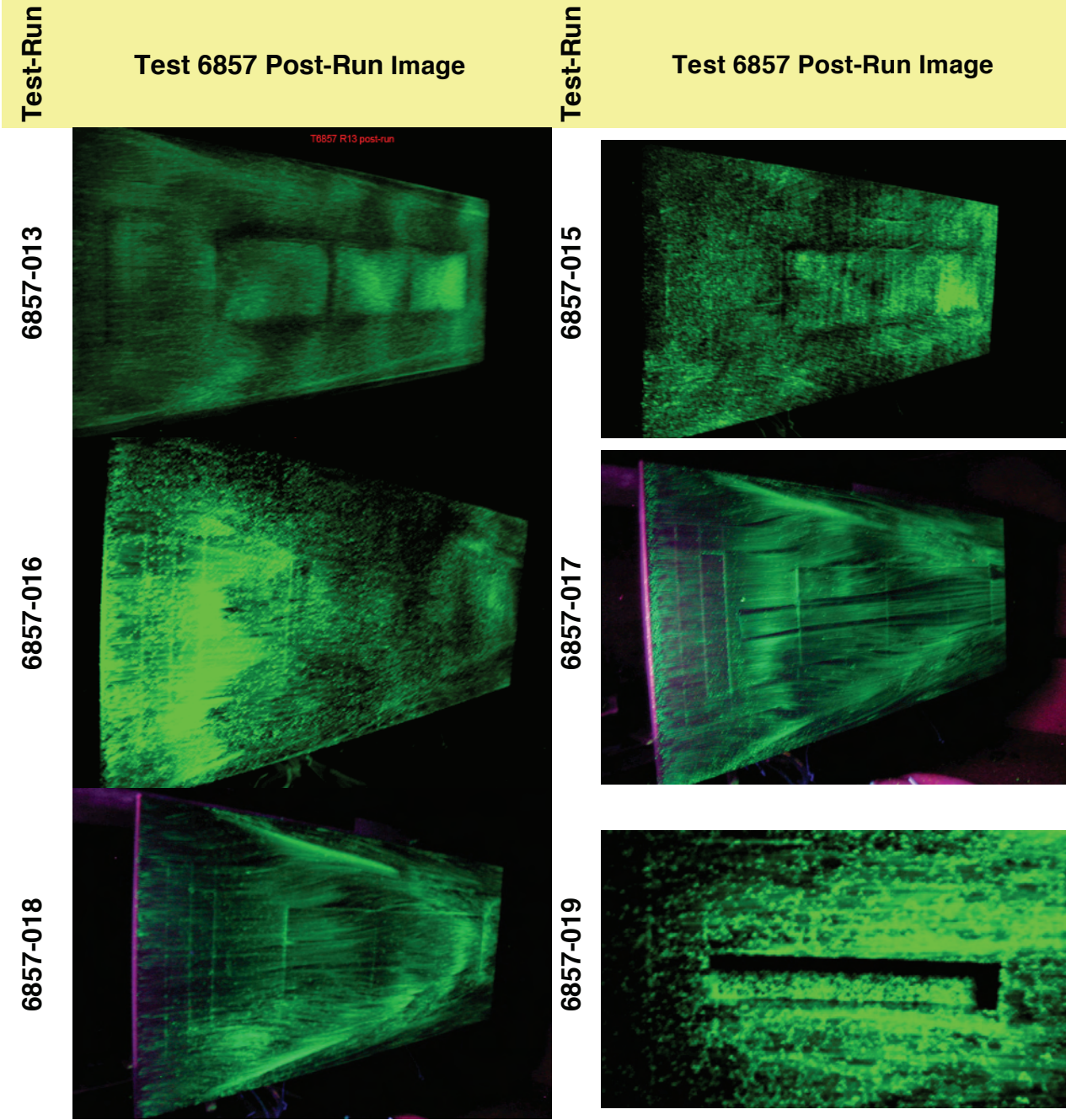


Figure 13.- Oil flow images for Test 6857.

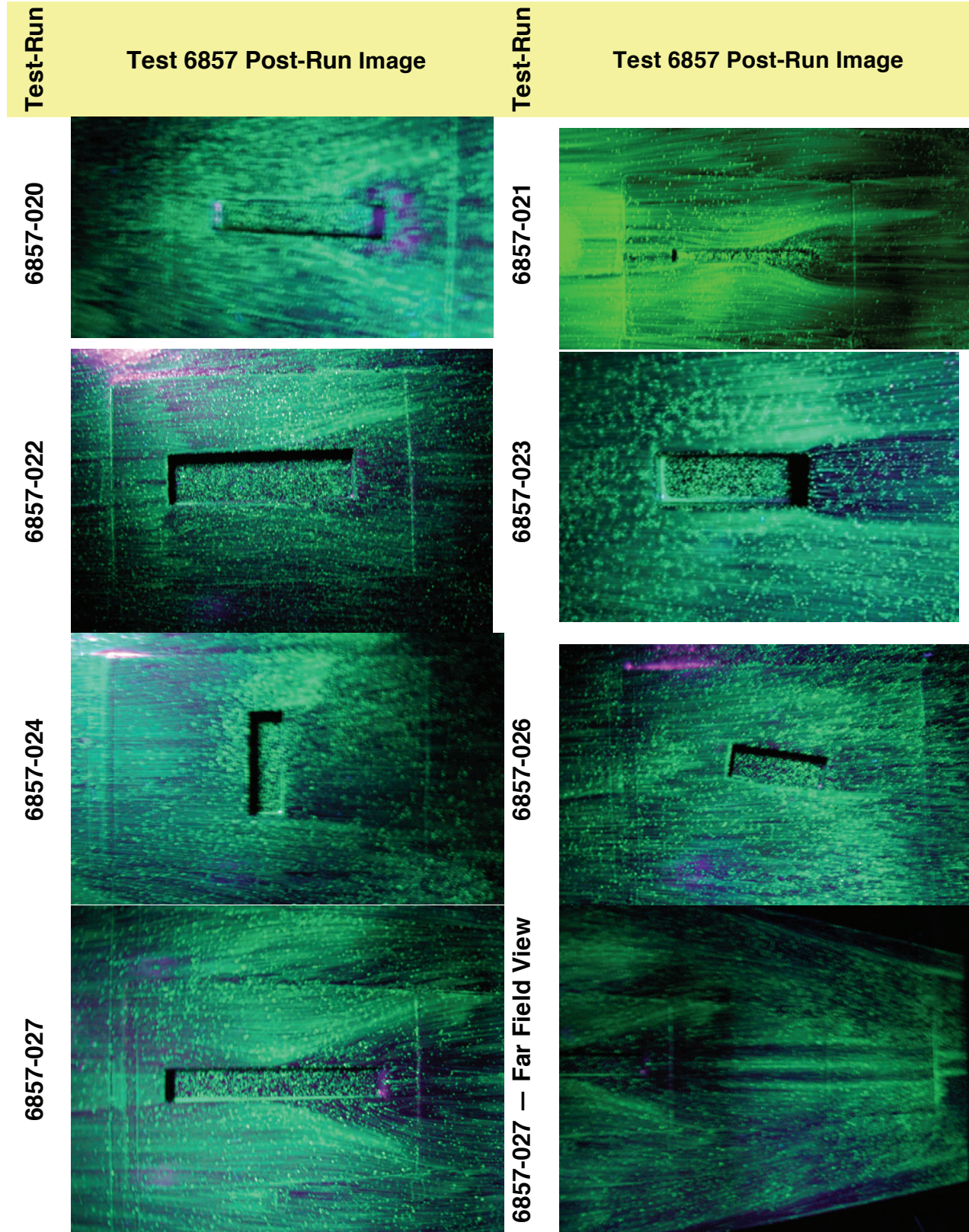
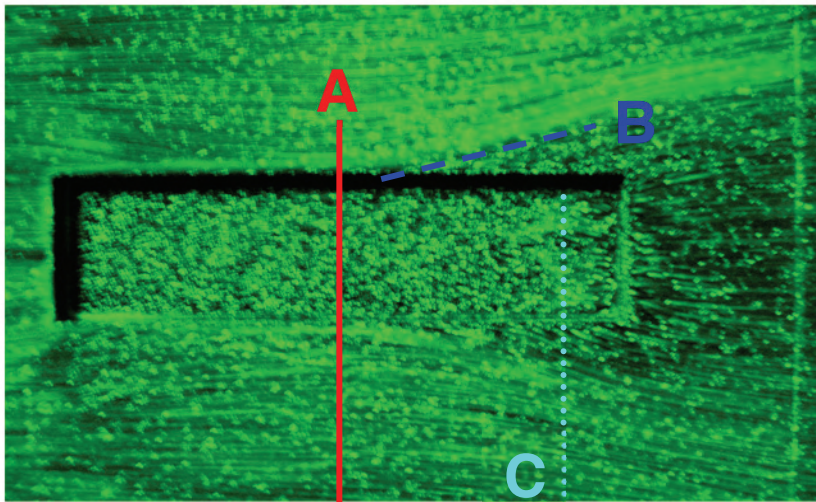
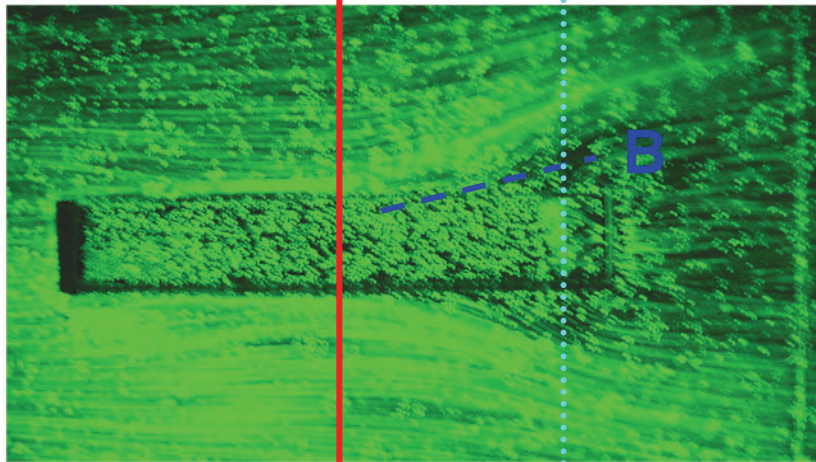


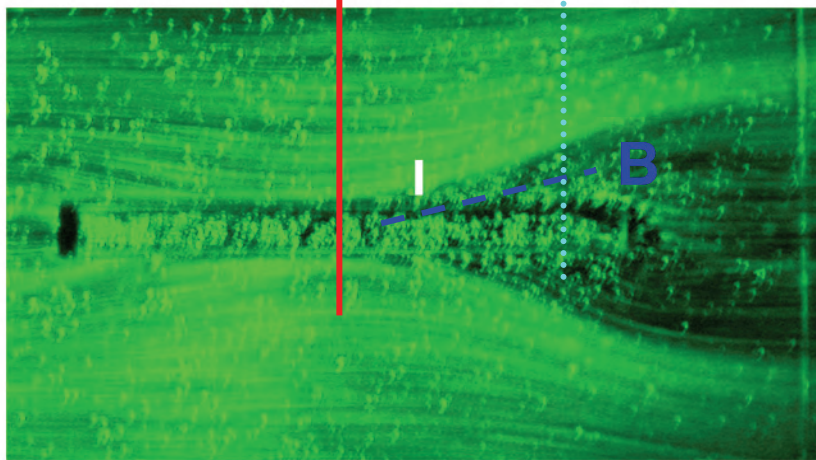
Figure 13.- Oil flow images for Test 6857 (Concluded).



**T6857**  
**R22**  
**W/H=3.6**



**T6857**  
**R20**  
**W/H=2.4**



**T6857**  
**R21**  
**W/H=1.2**

Figure 14.- Oil flow visualization of closed-cavity width effect -  $L/H=14$ ,  $H/\delta=1.1$ .

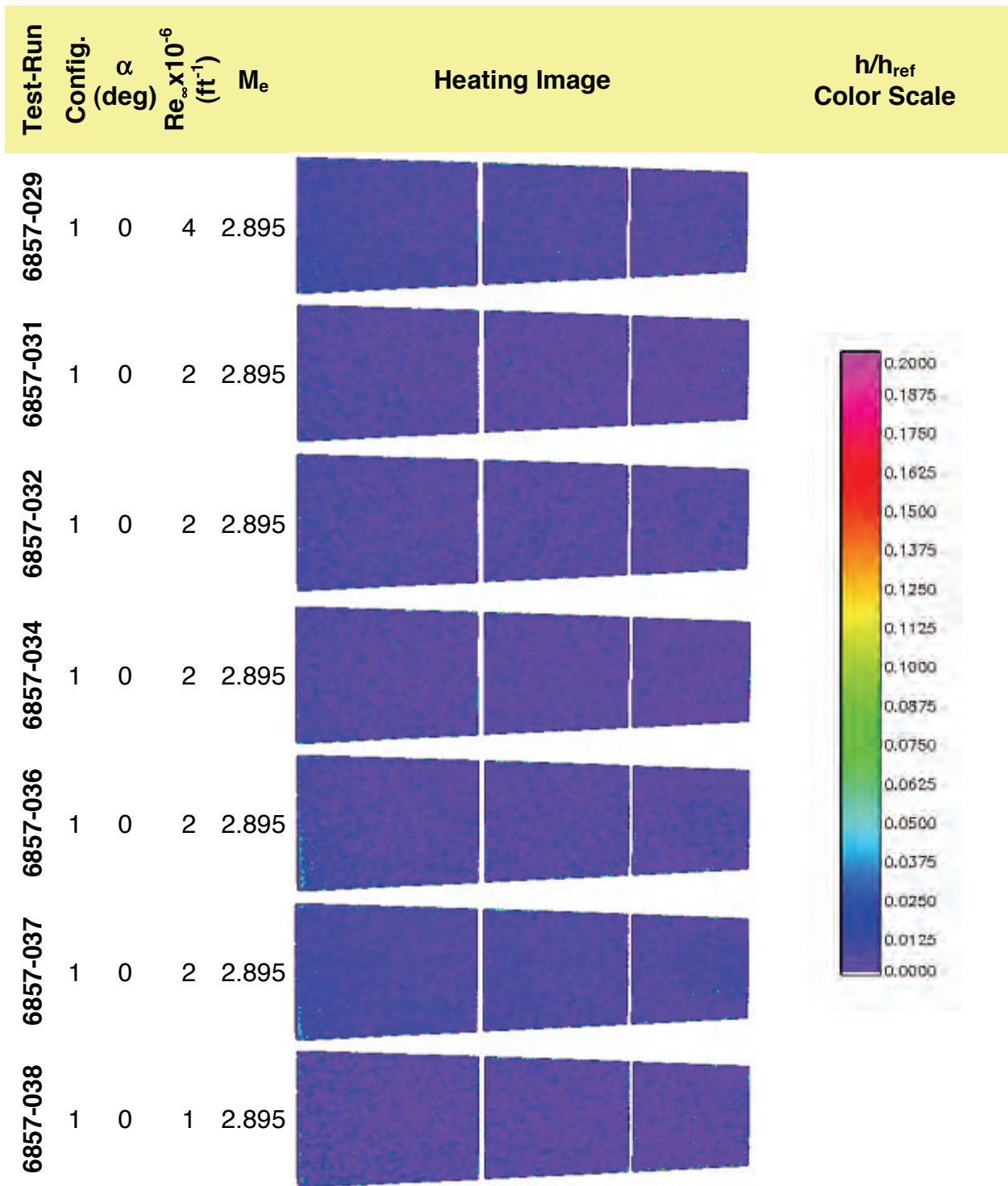


Figure 15.- Baseline heating runs for Test 6857.

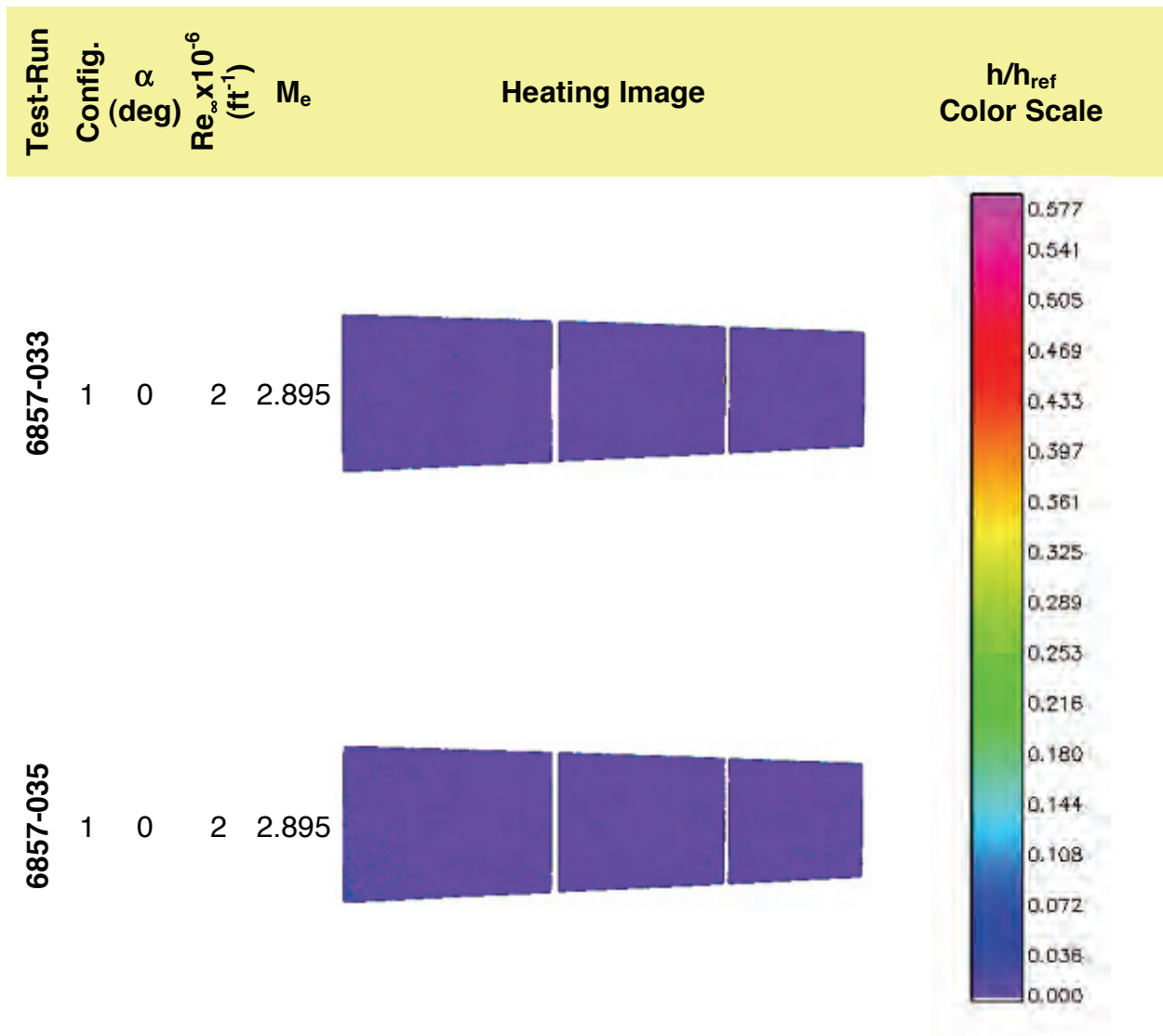


Figure 15.- Baseline heating runs for Test 6857 (Concluded).



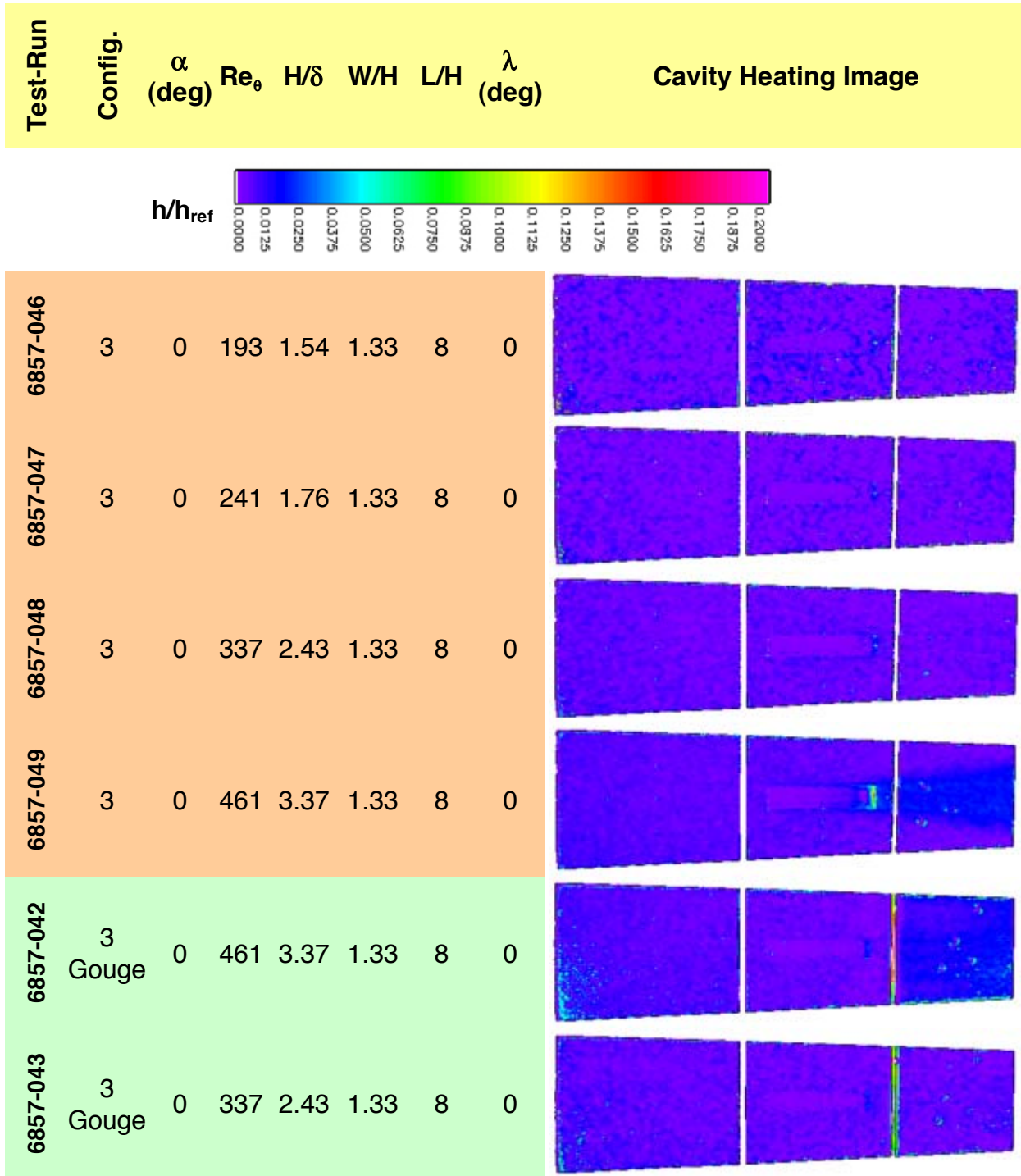


Figure 16.- Open flow cavity heating runs for Test 6857.

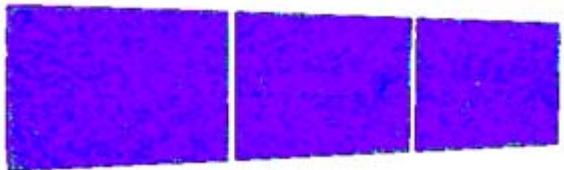
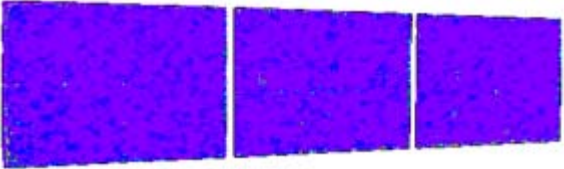
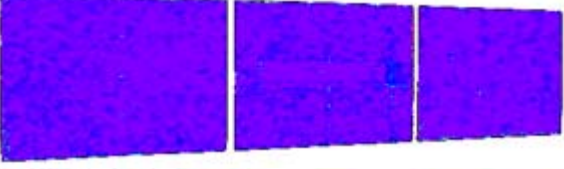





Test-Run	Config.	$\alpha$ (deg)	$Re_0$	H/ $\delta$	W/H	L/H	$\lambda$ (deg)	Cavity Heating Image
6857-044	3 Gouge	0	241	1.76	1.33	8	0	
6857-045	3 Gouge	0	193	1.54	1.33	8	0	
6857-050	3 Gap	0	241	1.76	1.33	8	0	
6857-051	3 Gap	0	337	2.43	1.33	8	0	
6857-052	3 Gap	0	461	3.37	1.33	8	0	
6857-057	3 Gap	0	241	1.76	1.33	8	0	
6857-058	3 Gap	0	337	2.43	1.33	8	0	
6857-059	3 Gap	0	461	3.37	1.33	8	0	

Figure 16.- Open flow cavity heating runs for Test 6857 (Continued).

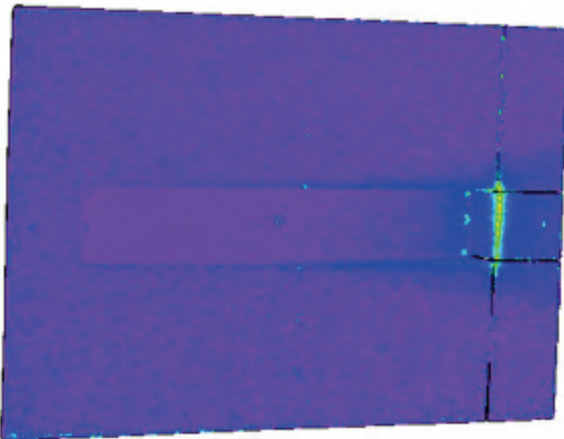
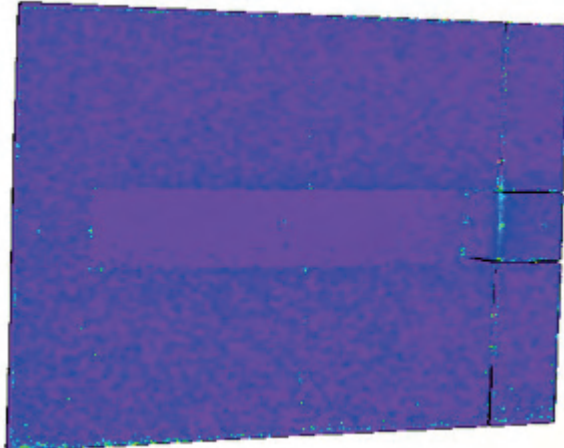
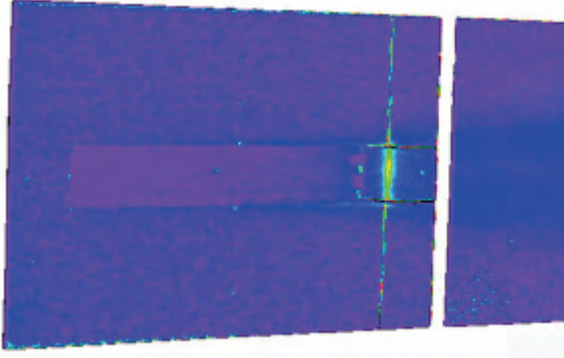
Test-Run	Config.	$\alpha$ (deg)	$Re_\theta$	$H/\delta$	$W/H$	$L/H$	$\lambda$ (deg)	Cavity Heating Image
6857-095	f 3 Gap	5	337	2.43	1.33	8	0	
6857-096	f 3 Gap	0	337	2.43	1.33	8	0	
6857-093	f 3 Gap	0	461	3.37	1.33	8	0	

Figure 16.- Open flow cavity heating runs for Test 6857 (Continued).

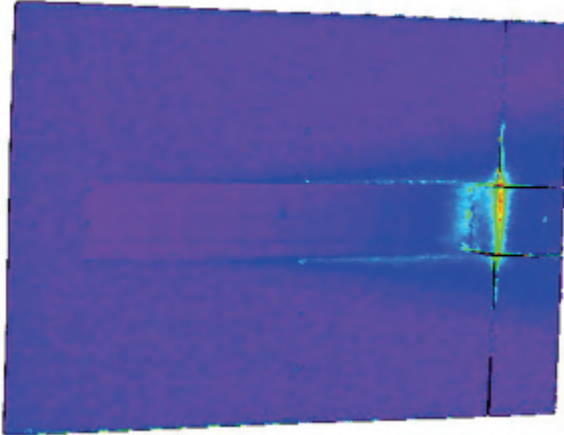
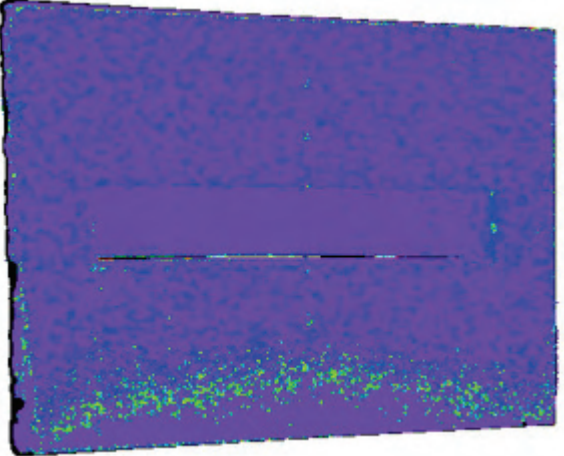
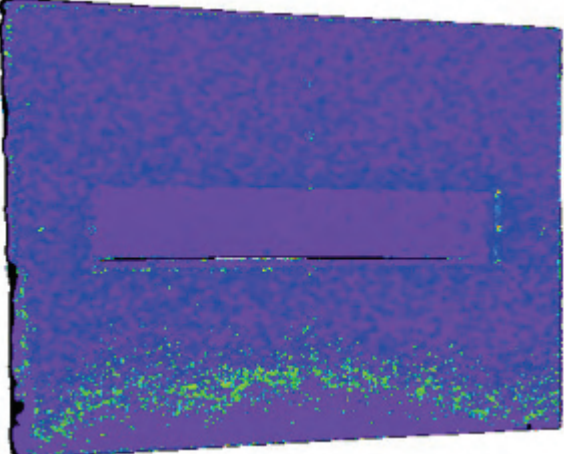
Test-Run	Config.	$\alpha$ (deg)	$Re_0$	$H/\delta$	$W/H$	$L/H$	$\lambda$ (deg)	Cavity Heating Image
6857-094 f	3 Gap	-5	461	3.37	1.33	8	0	
6857-102 f No Suction	3 Slot	0	241	1.76	1.33	8	0	
6857-103 f Suction Applied	3 Slot	0	241	1.76	1.33	8	0	

Figure 16.- Open flow cavity heating runs for Test 6857 (Continued).

Test-Run	Config.	$\alpha$ (deg)	$Re_0$	$H/\delta$	$W/H$	$L/H$	$\lambda$ (deg)	Cavity Heating Image
6857-106 f No Suction	3 Slot	0	461	3.37	1.33	8	0	
6857-105 f No Suction	3 Slot	-5	3.37	1.33	8	0		
6857-104 f Suction Applied	3 Slot	-5	461	3.37	1.33	8	0	

Figure 16.- Open flow cavity heating runs for Test 6857 (Concluded).

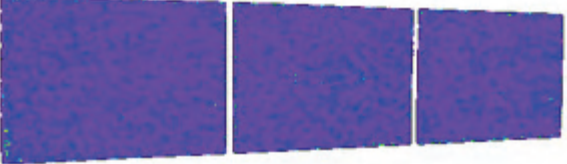


Test-Run	Config.	$\alpha$ (deg)	$Re_\theta$	$H/\delta$	$W/H$	$L/H$	$\lambda$ (deg)	Cavity Heating Image
6857-060	5	0	241	0.92	1.33	8	0	
6857-061	5	0	337	1.27	1.33	8	0	
6857-062	5	0	461	1.76	1.33	8	0	

Figure 16.- Open flow cavity heating runs for Test 6857 (Concluded).

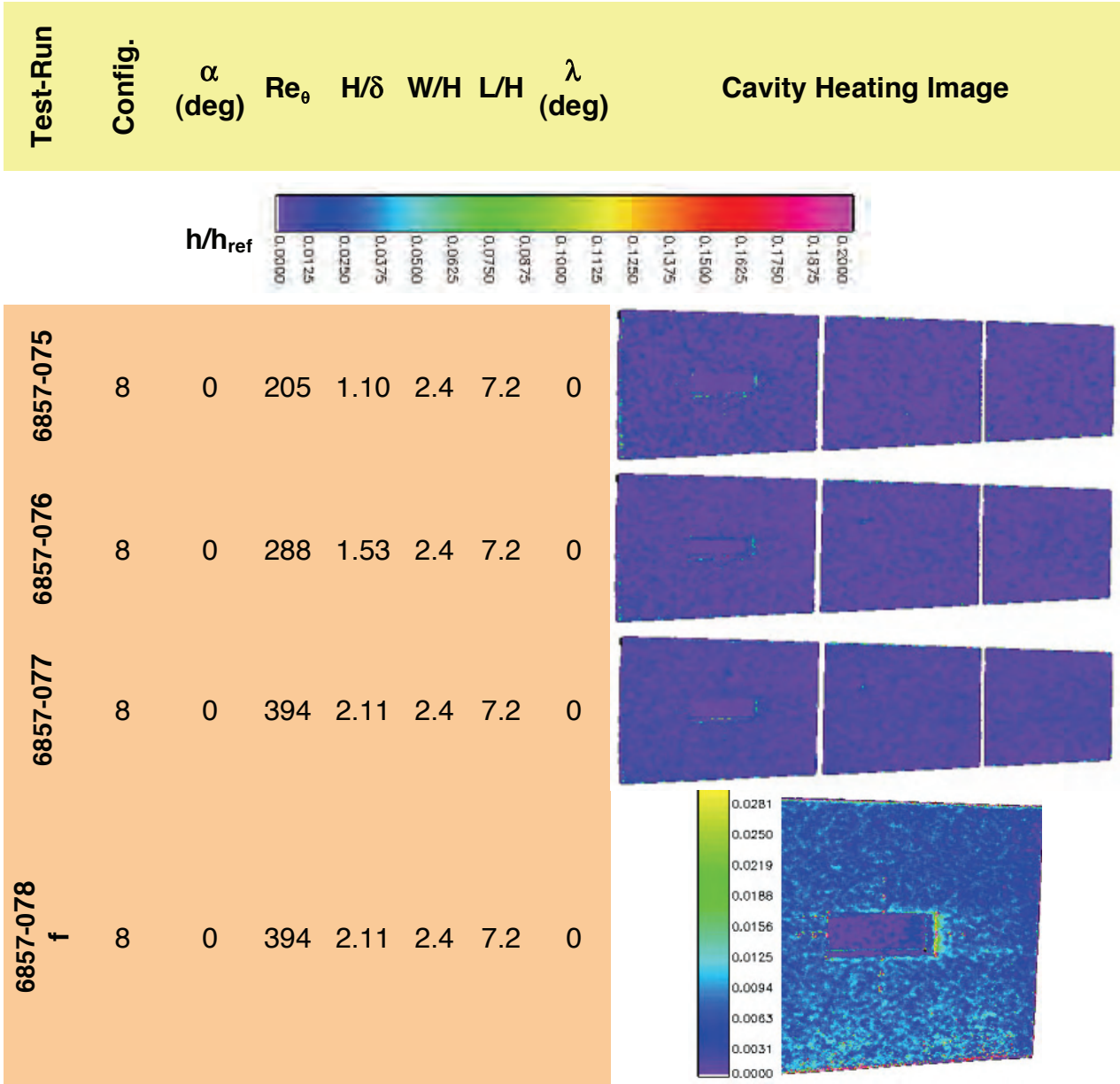


Figure 17.- Cavity alignment effect on open flow cavity heating for Test 6857.

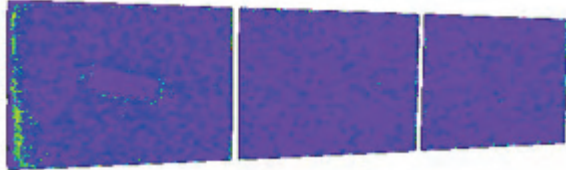
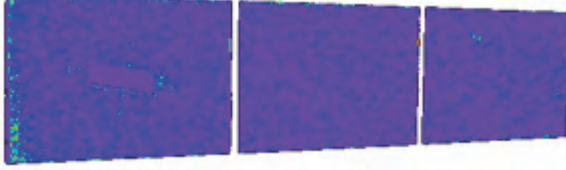

Test-Run	Config.	$\alpha$ (deg)	$Re_\theta$	$H/\delta$	$W/H$	$L/H$	$\lambda$ (deg)	Cavity Heating Image
6857-063	11	0	205	1.10	2.40	7.2	10	
6857-064	11	0	288	1.53	2.4	7.2	10	
6857-065	11	0	394	2.11	2.4	7.2	10	

Figure 17.- Cavity alignment effect on open flow cavity heating for Test 6857 (Concluded).



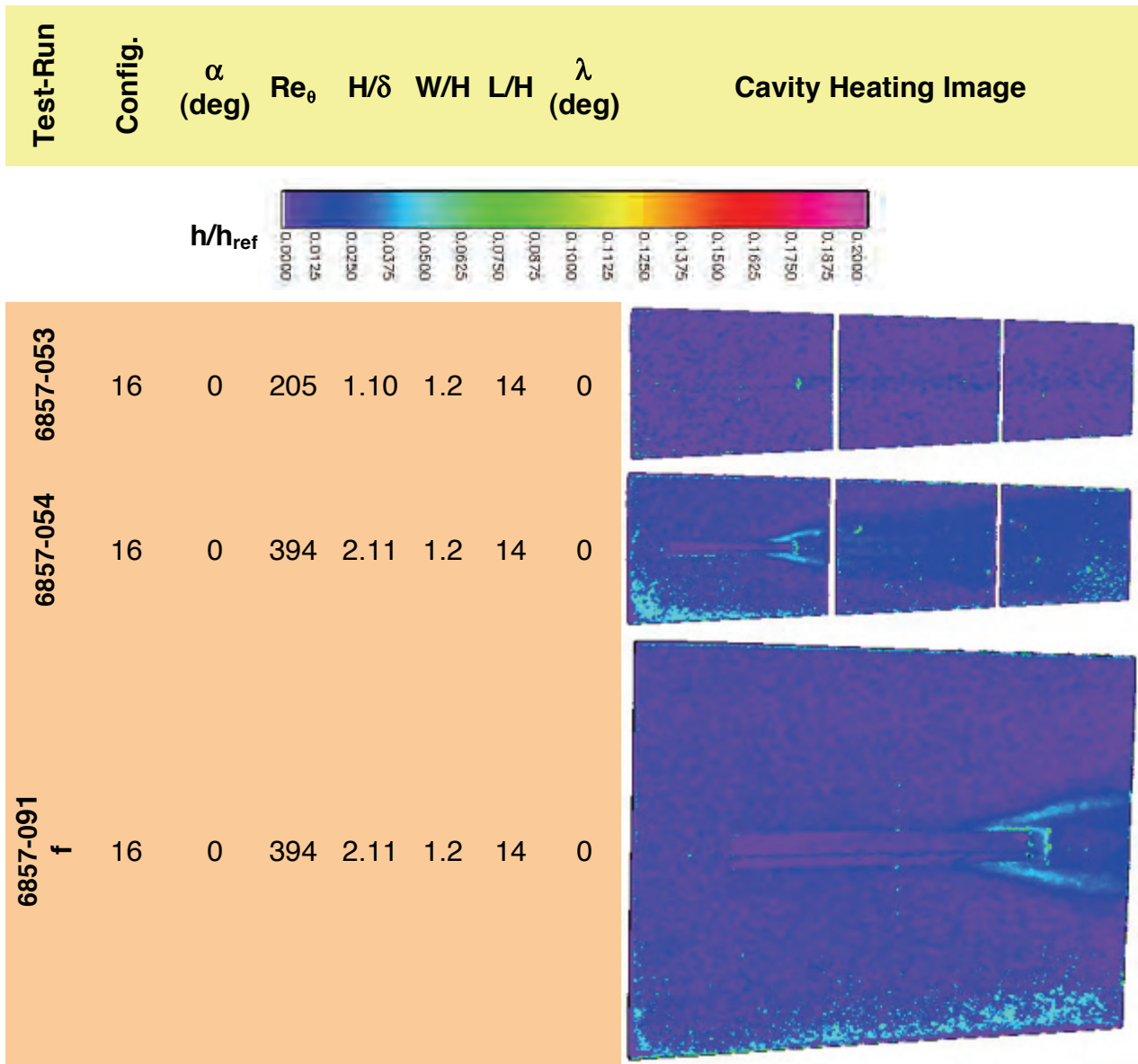


Figure 18.- Closed flow cavity heating runs for Test 6857.

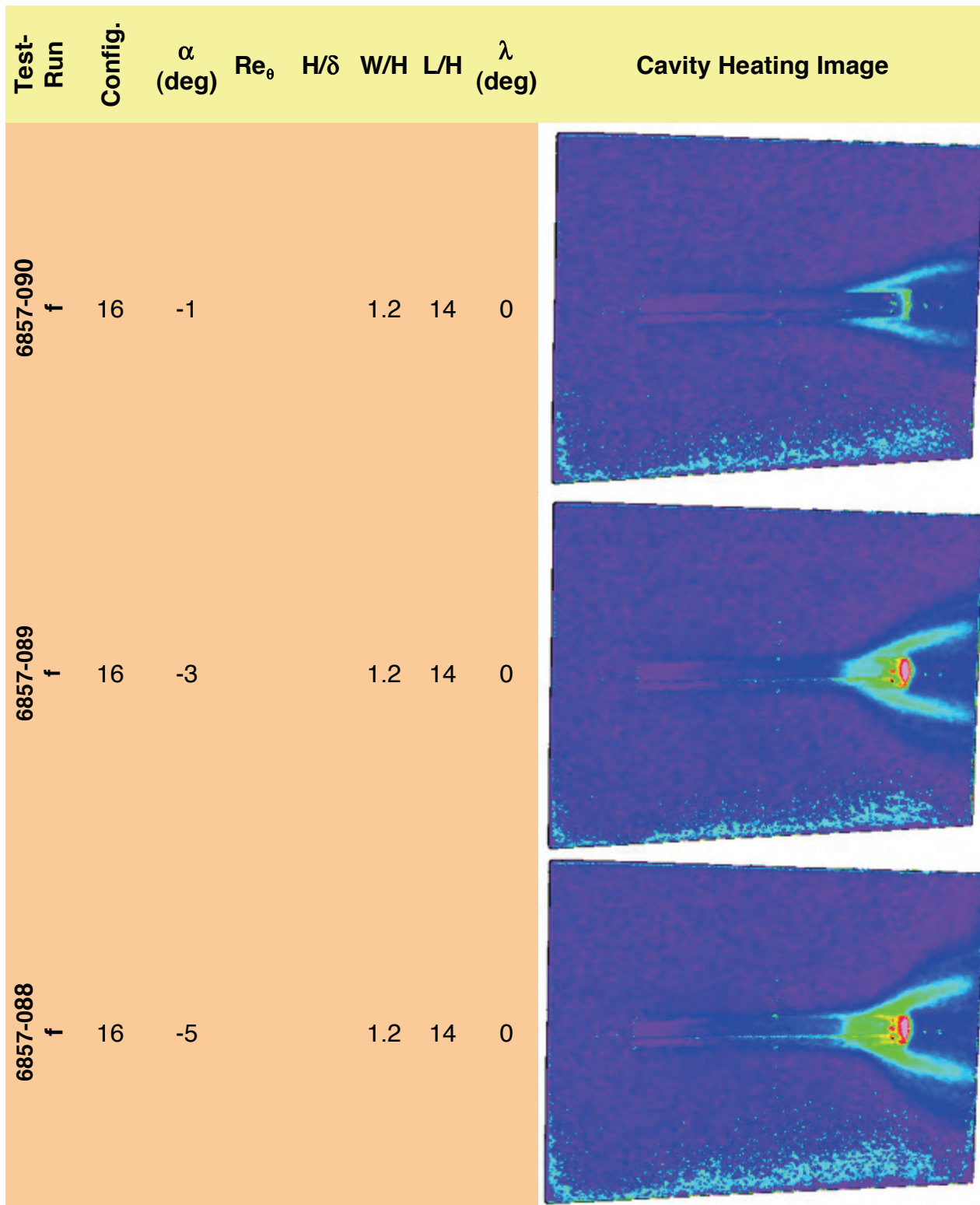


Figure 18.- Closed flow cavity heating runs for Test 6857 (Continued).

Test-Run	Config.	$\alpha$ (deg)	$Re_0$	$H/\delta$	$W/H$	$L/H$	$\lambda$ (deg)	Cavity Heating Image
6857-055	16	0	288	1.53	1.2	14	0	
6857-092 f	16	0	288	1.53	1.2	14	0	
6857-056	16	0	164	0.96	1.2	14	0	
6857-066	17	0	205	1.10	2.4	14	0	
6857-067	17	0	288	1.53	2.4	14	0	
6857-068	17	0	394	2.11	2.4	14	0	

Figure 18.- Closed flow cavity heating runs for Test 6857 (Continued).

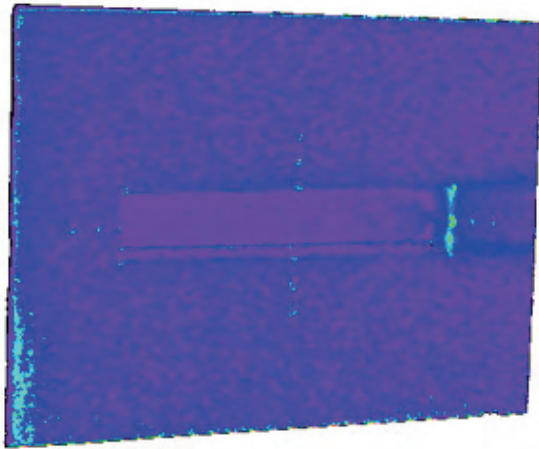
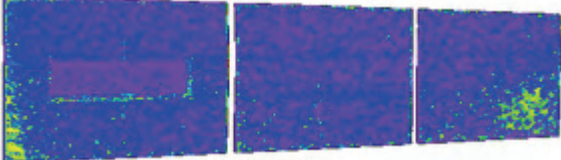
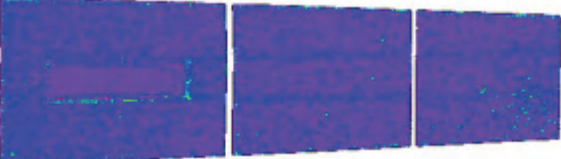
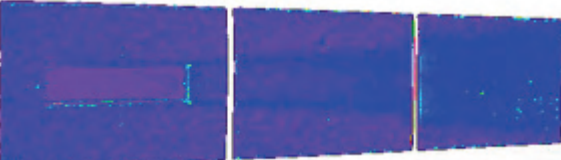
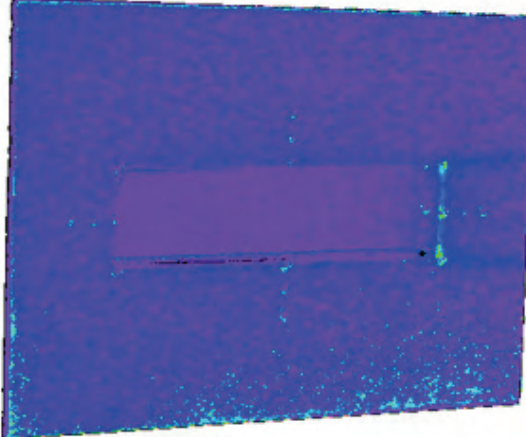
Test-Run	Config.	$\alpha$ (deg)	$Re_0$	$H/\delta$	W/H	L/H	$\lambda$ (deg)	Cavity Heating Image
6857-081 f	17	0	394	2.11	2.4	14	0	
6857-069	18	0	205	1.10	3.6	14	0	
6857-070	18	0	288	1.53	3.6	14	0	
6857-071	18	0	394	2.11	3.6	14	0	
6857-085 f	18	1			3.6	14	0	

Figure 18.- Closed flow cavity heating runs for Test 6857 (Continued).

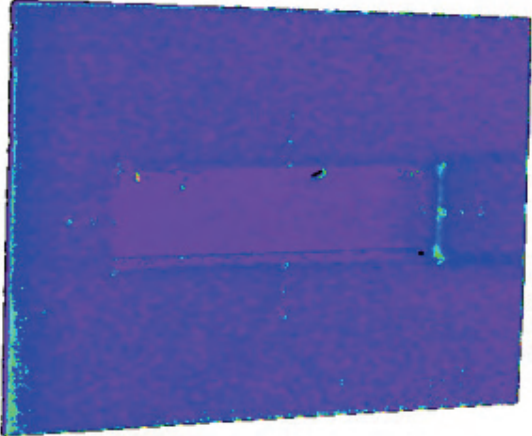
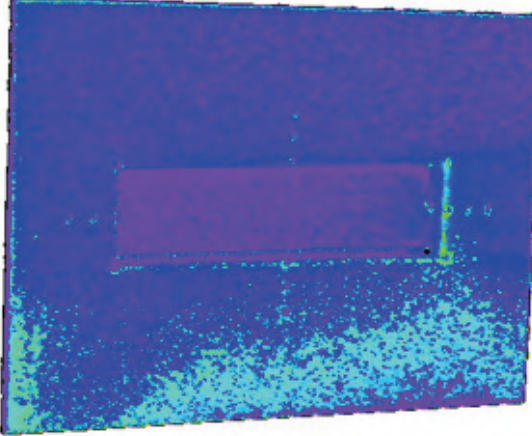
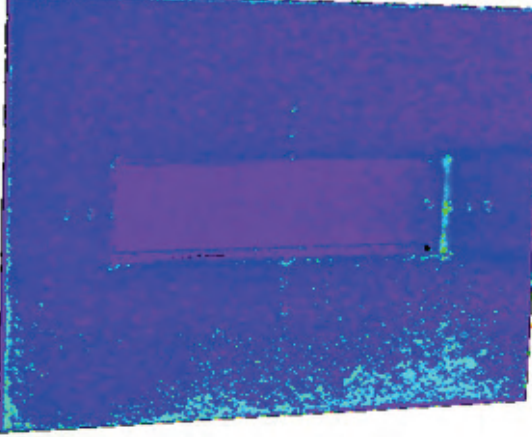
Test-Run	Config.	$\alpha$ (deg)	$Re_0$	$H/\delta$	$W/H$	$L/H$	$\lambda$ (deg)	Cavity Heating Image
6857-082 f	18	0	394	2.11	3.6	14	0	
6857-083 f	18	-1			3.6	14	0	
6857-084 f	18	-1			3.6	14	0	

Figure 18.- Closed flow cavity heating runs for Test 6857 (Continued).

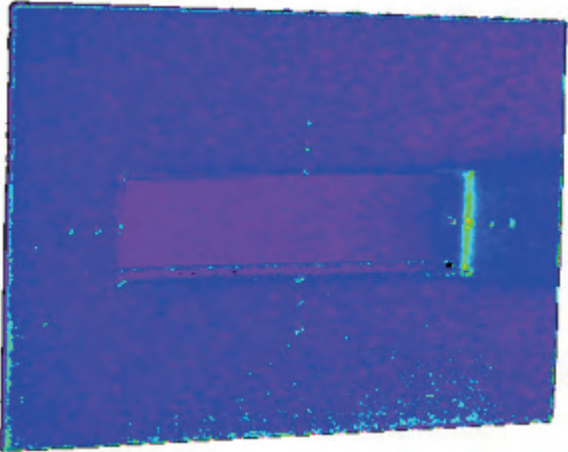
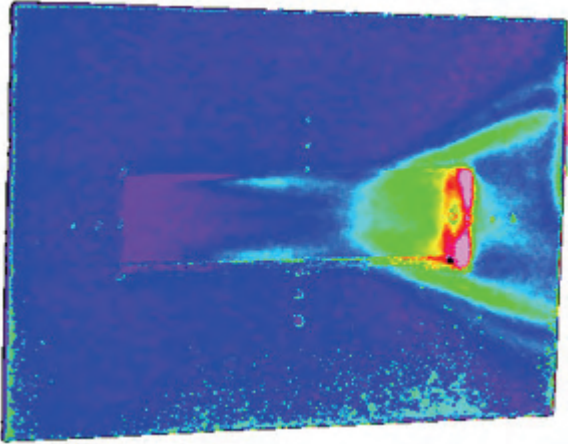
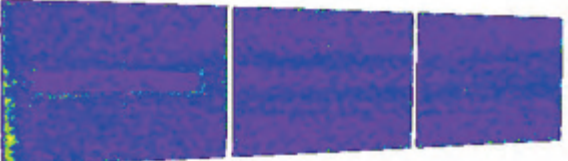
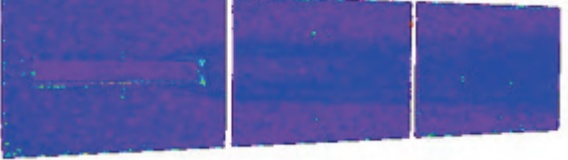
Test-Run	Config.	$\alpha$ (deg)	$Re_\theta$	$H/\delta$	$W/H$	$L/H$	$\lambda$ (deg)	Cavity Heating Image
6857-086 f	18	-3			3.6	14	0	
6857-087 f	18	-5			3.6	14	0	
6857-072	19	0	205	1.10	2.4	17	0	
6857-073	19	0	288	1.53	2.4	17	0	

Figure 18.- Closed flow cavity heating runs for Test 6857 (Continued).

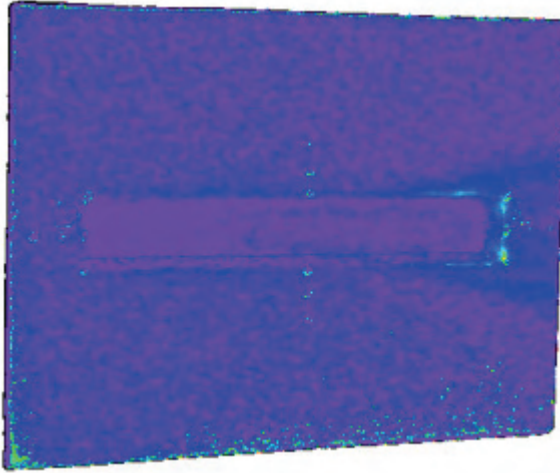
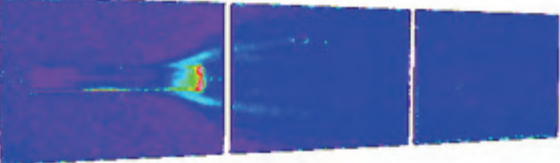
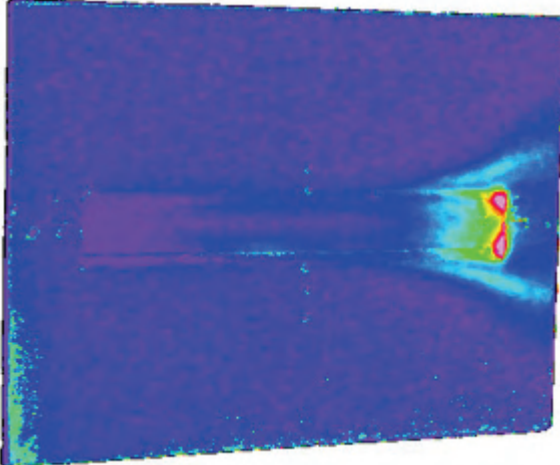
Test-Run	Config.	$\alpha$ (deg)	$Re_0$	$H/\delta$	$W/H$	$L/H$	$\lambda$ (deg)	Cavity Heating Image
6857-080 f	19	0	288	1.53	2.4	17	0	
6857-074	19	0	394	2.11	2.4	17	0	
6857-079 f	19	0	394	2.11	2.4	17	0	

Figure 18.- Closed flow cavity heating runs for Test 6857 (Concluded).

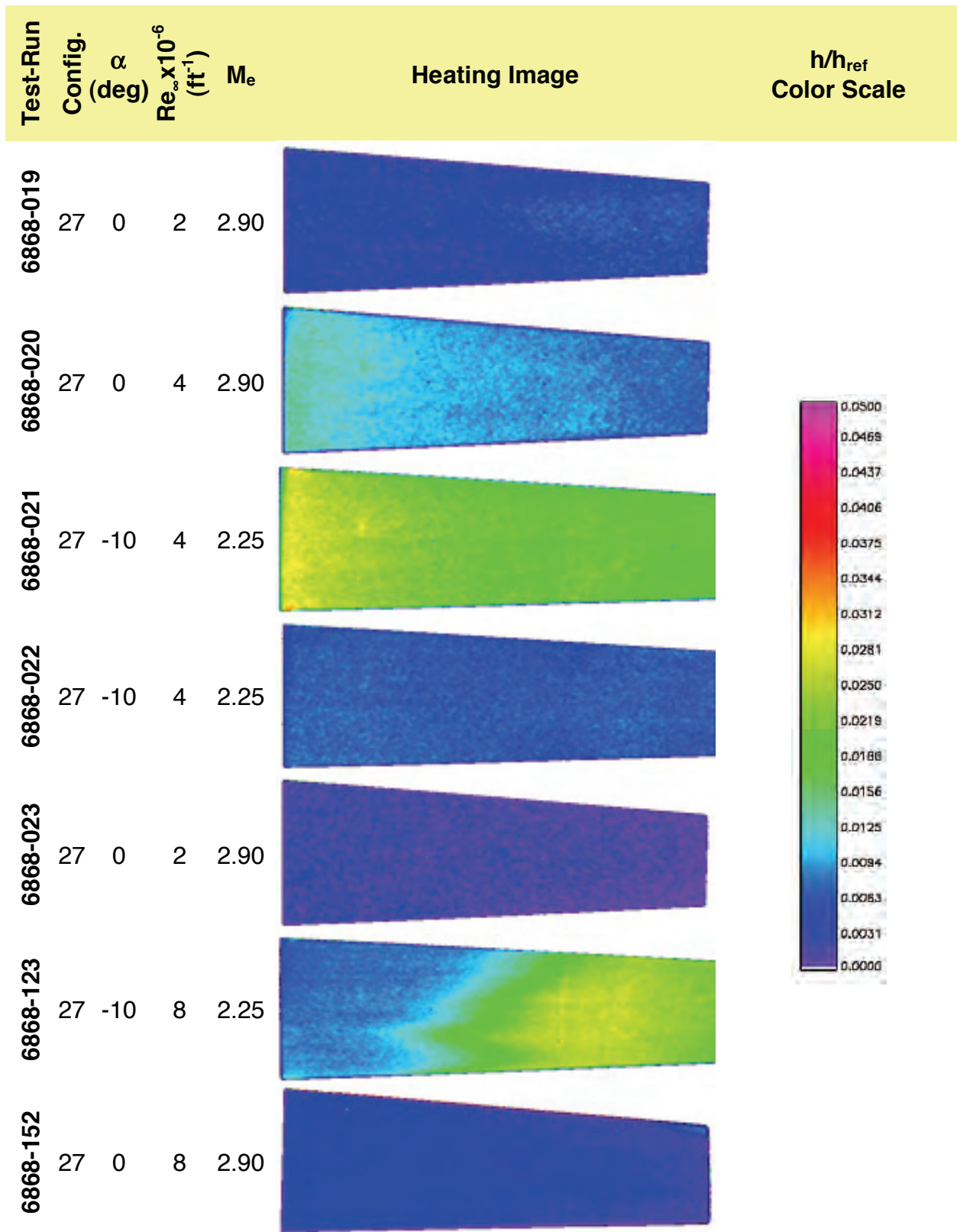


Figure 19.- Baseline heating runs for Test 6868.



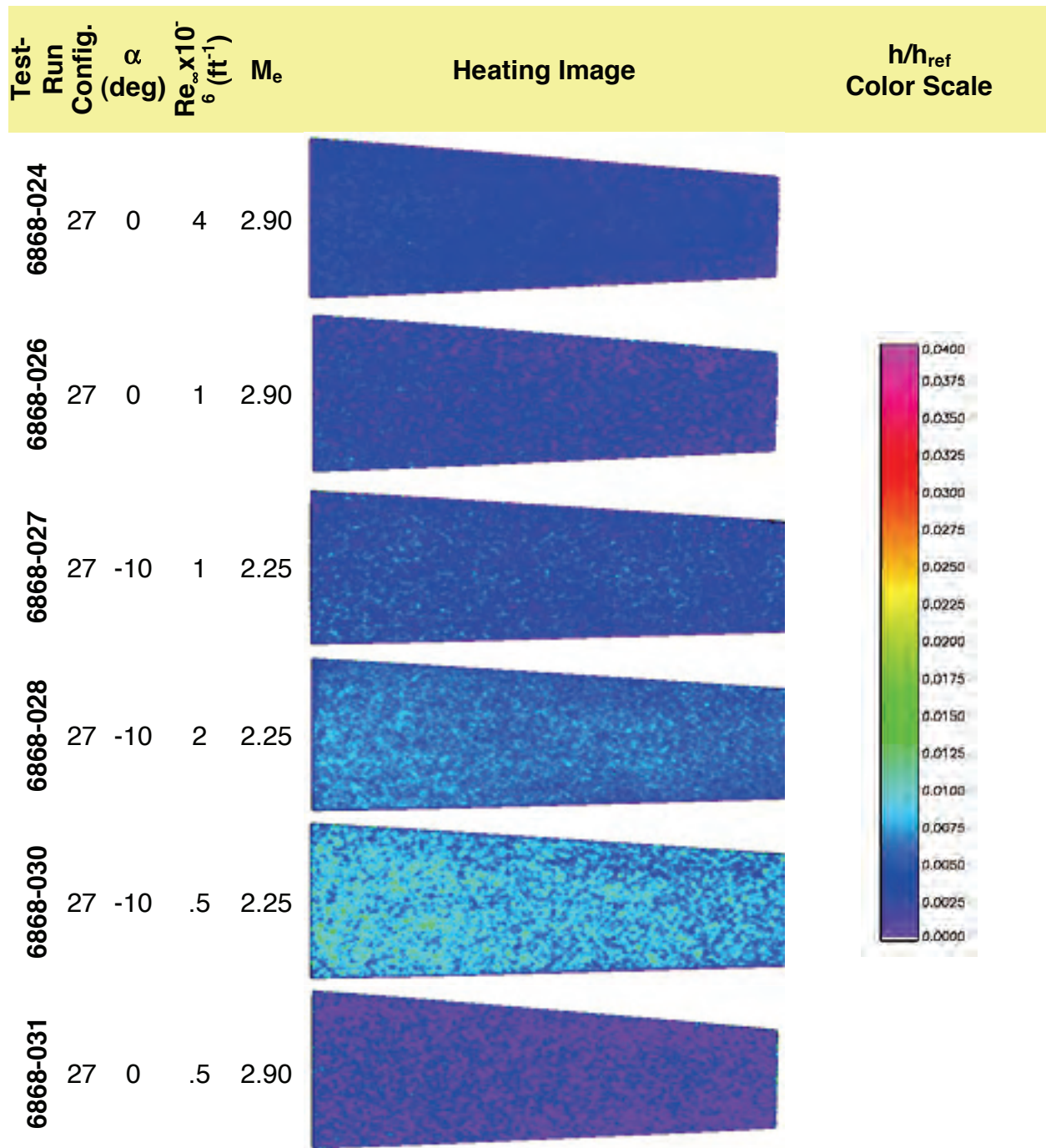


Figure 19.- Baseline heating runs for Test 6868 (Concluded).

Test-Run	Config.	$\alpha$ (deg)	$Re_\theta$	H/ $\delta$	W/H	L/H	$\lambda$ (deg)	Cavity Heating Image
----------	---------	-------------------	-------------	-------------	-----	-----	--------------------	----------------------



6868-017	5	0	346	1.57	1.3	8	0	
6868-131	9 s	0	288	1.1	2.4	7.2	0	
6868-132	9 s	-10			2.4	7.2	0	
6868-133	9 s	-10			2.4	7.2	0	

Figure 20.- Open (short) cavity heating runs for Test 6868.

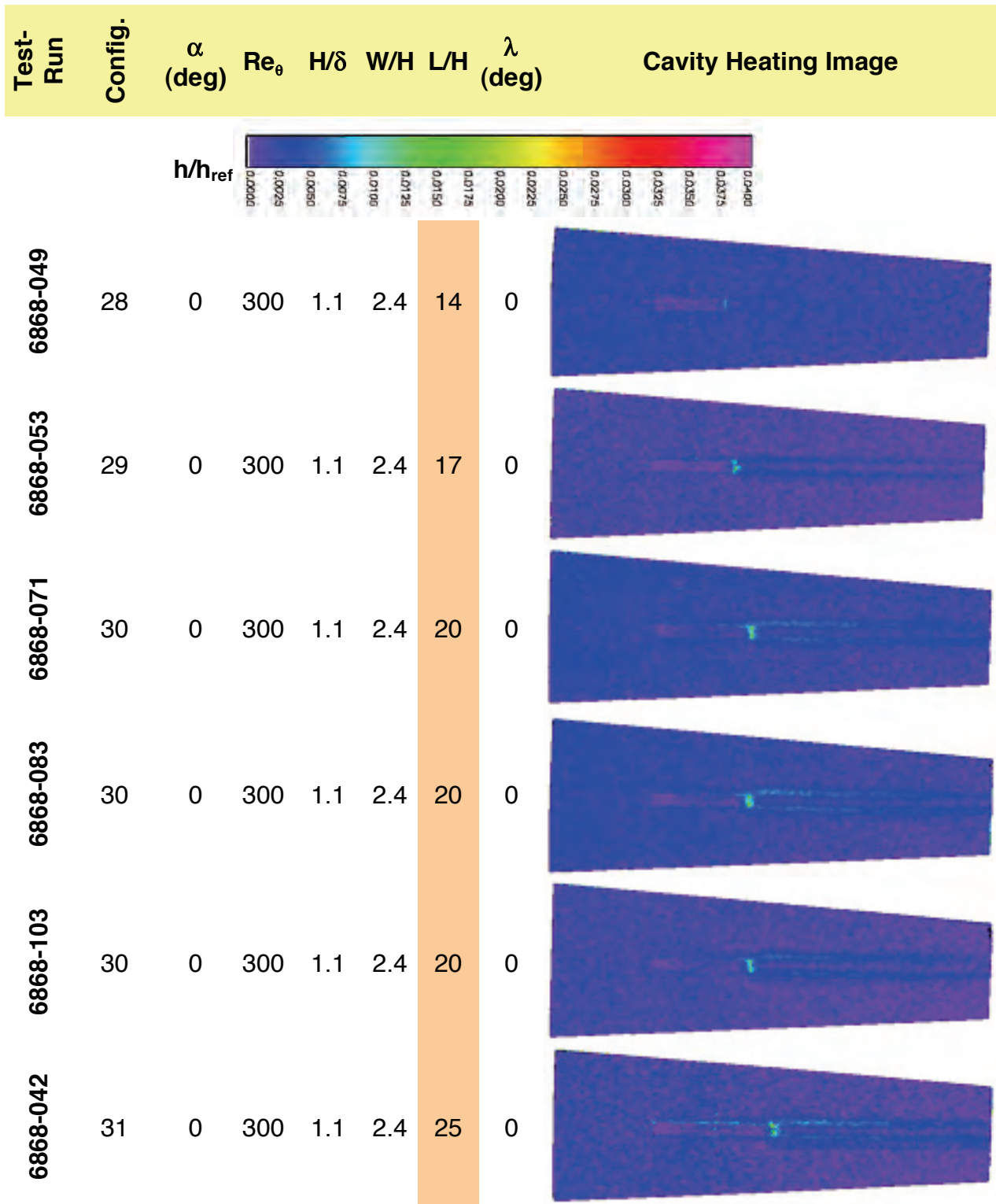


Figure 21.- Length effect on closed cavity heating for Test 6868 –  $Re_\theta=300$ ,  $H/\delta=1.1$ .

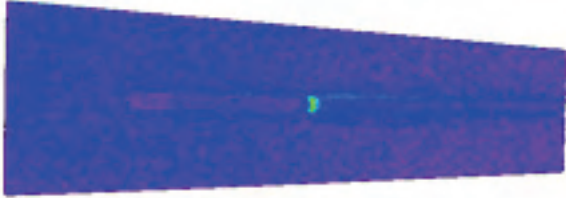

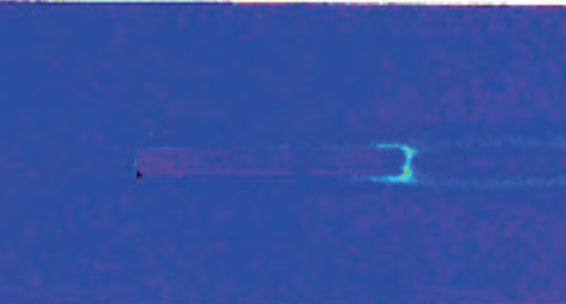
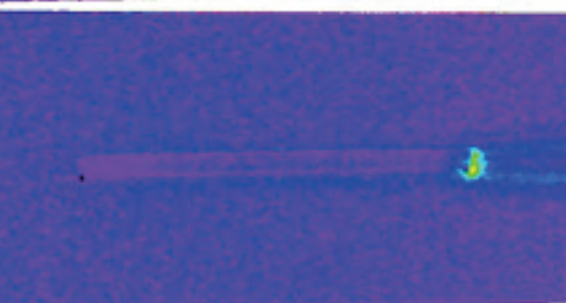
Test-Run	Config.	$\alpha$ (deg)	$Re_\theta$	$H/\delta$	$W/H$	$L/H$	$\lambda$ (deg)	Cavity Heating Image
6868-066	32	0	300	1.1	2.4	30	0	
6868-0140 f	28	0	300	1.1	2.4	14	0	
6868-0124 f	30	0	300	1.1	2.4	20	0	
6868-0128 f	32	0	300	1.1	2.4	30	0	

Figure 21.- Length effect on closed cavity heating for Test 6868 –  $Re_\theta=300$ ,  $H/\delta=1.1$  (Concluded).

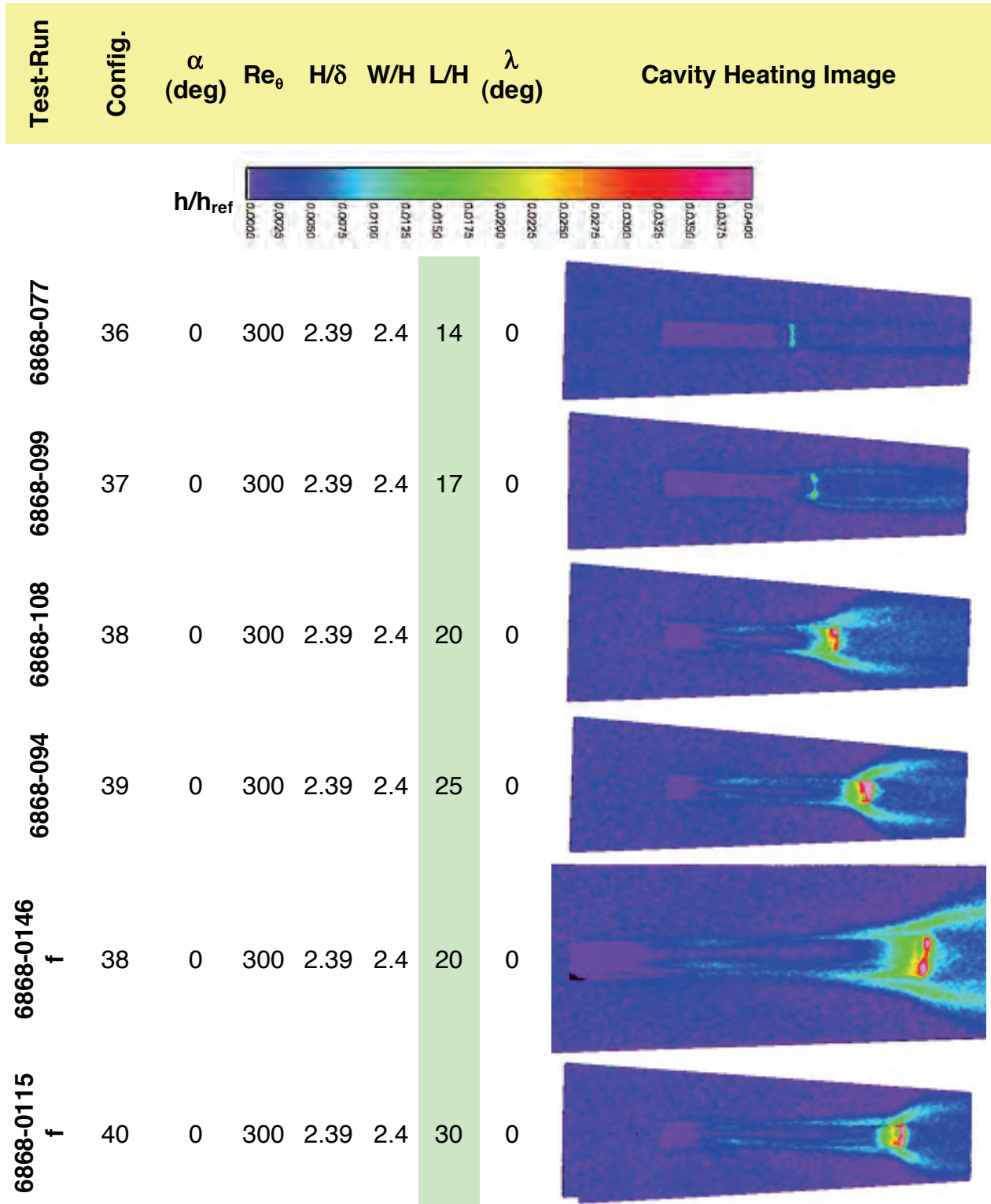


Figure 22.- Length effect on closed cavity heating for Test 6868 –  $Re_0=300$ ,  $H/\delta=2.39$ .

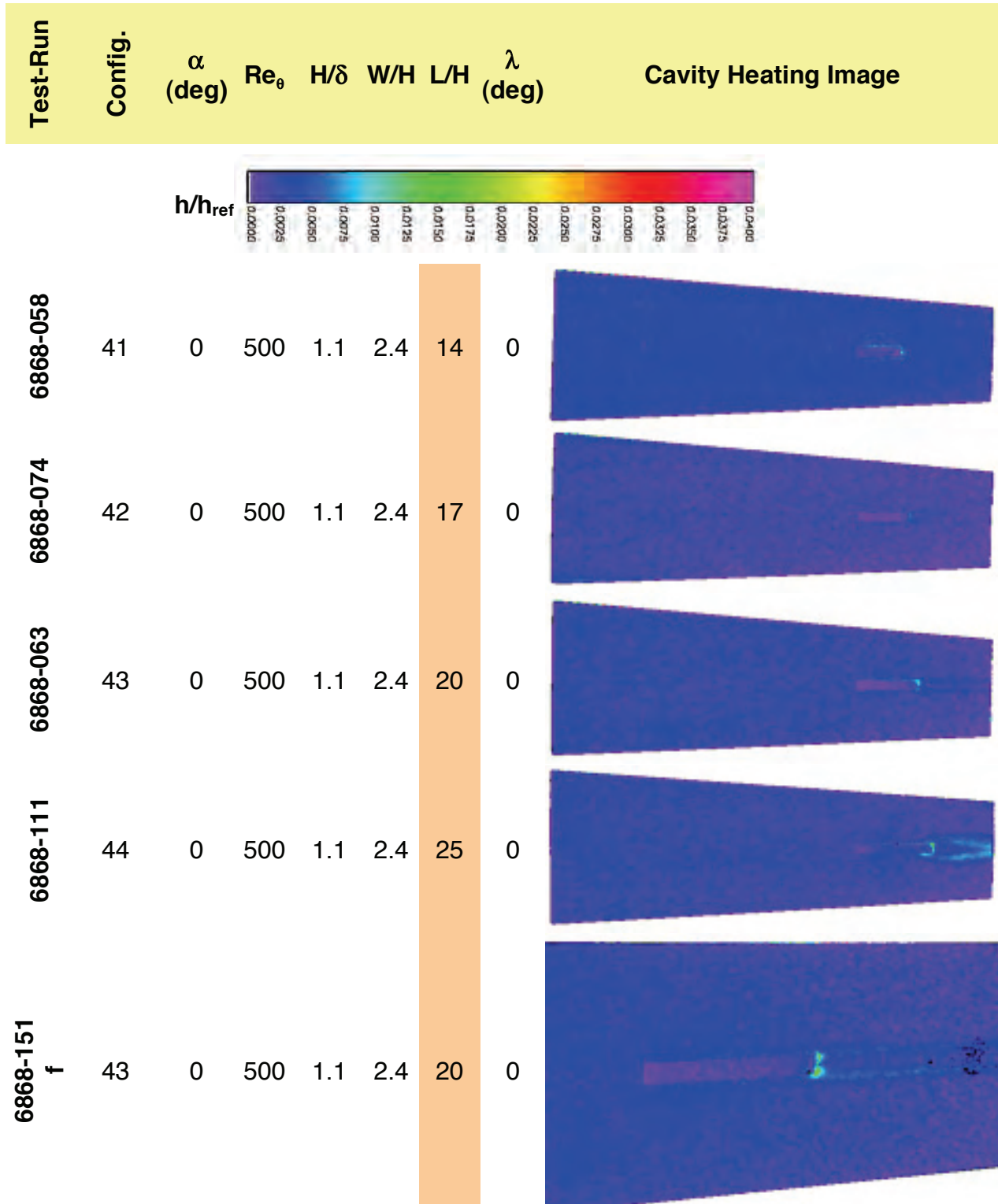


Figure 23.- Length effect on closed cavity heating for Test 6868 –  $Re_\theta=500$ ,  $H/\delta=1.1$ .

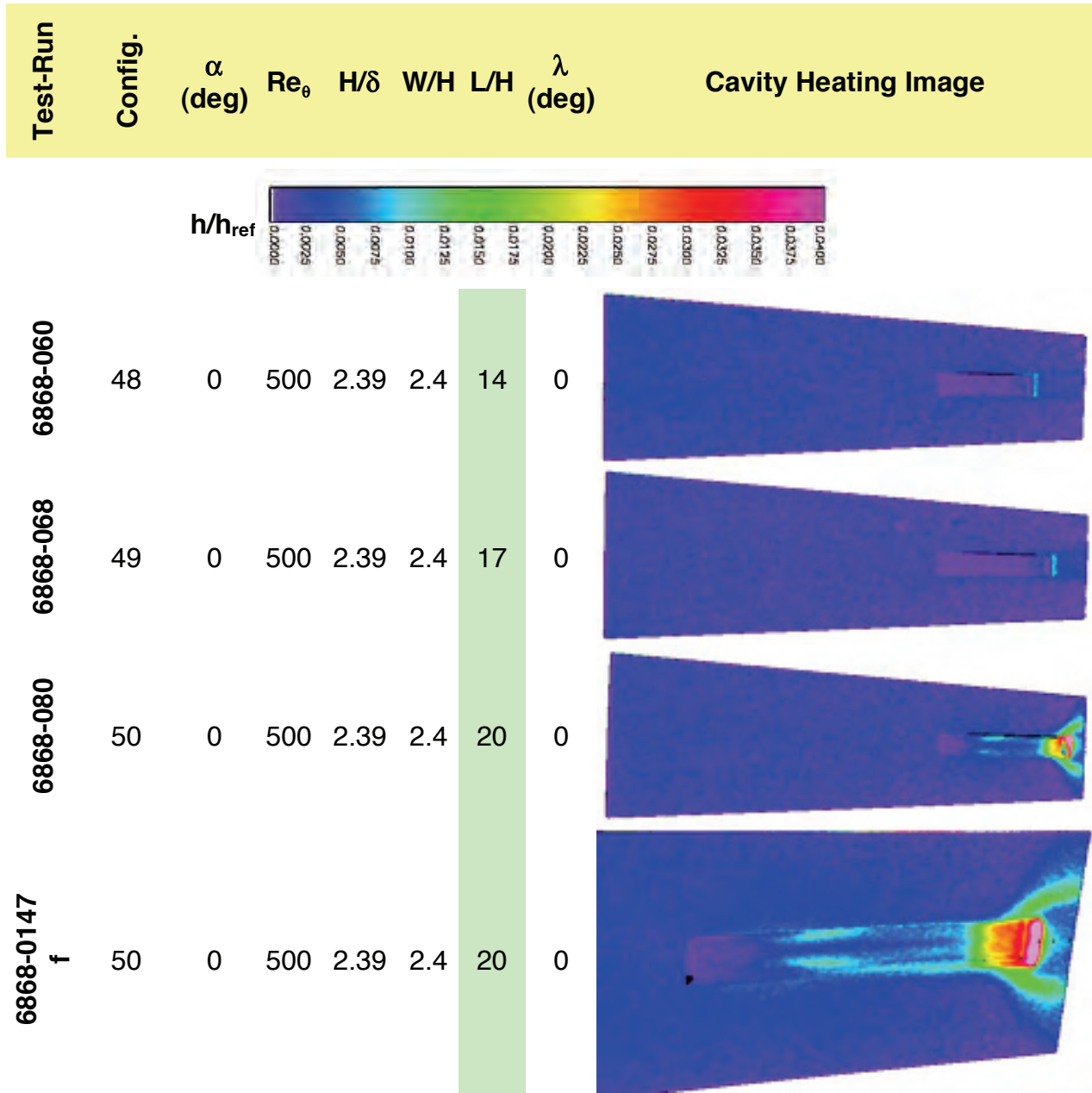


Figure 24.- Length effect on closed cavity heating for Test 6868 –  $Re_\theta=500$ ,  $H/\delta=2.39$ .

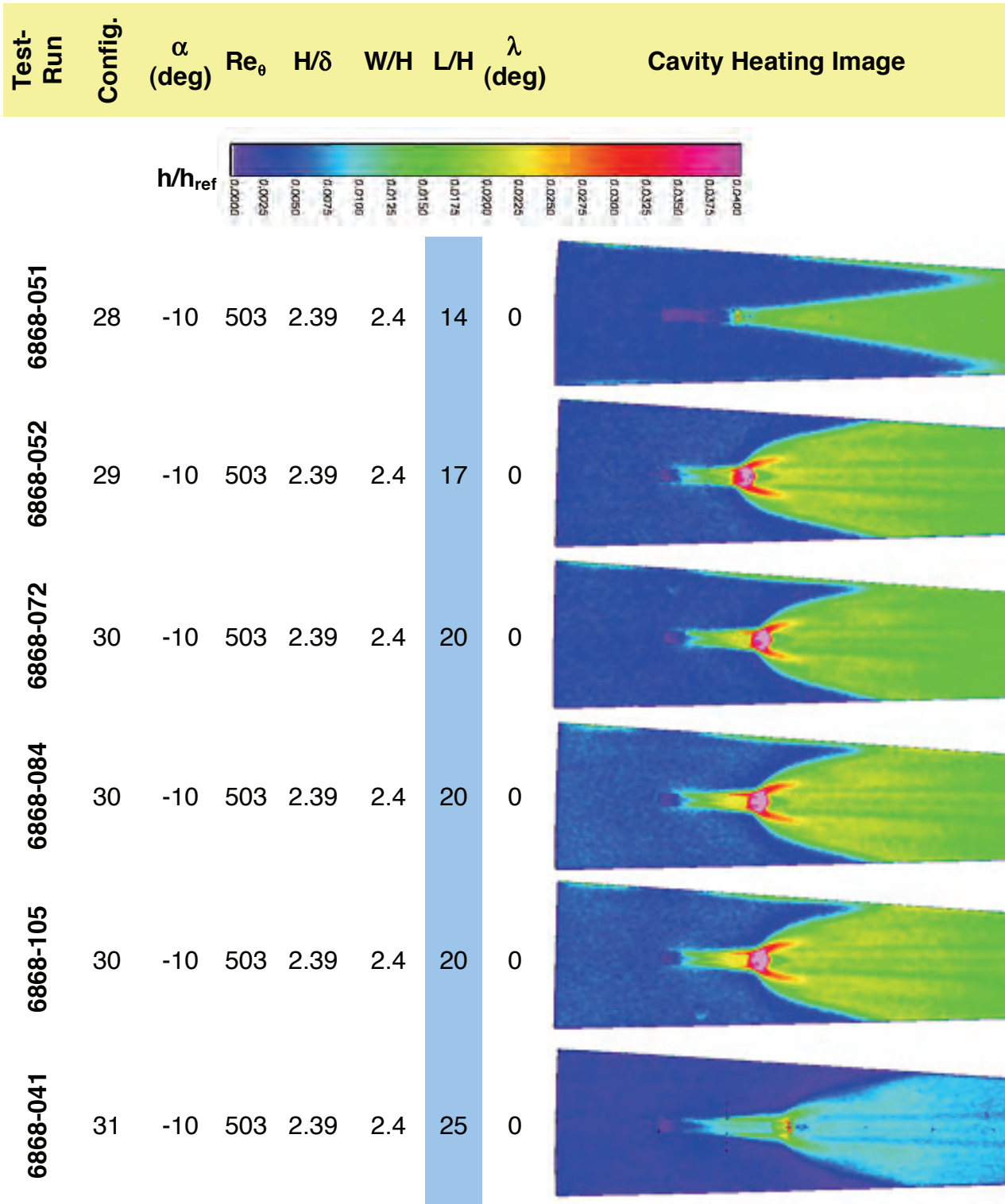


Figure 25.- Depth effect on closed cavity heating for Test 6868 –  $Re_\theta=503$ ,  $H/\delta=2.39$ .



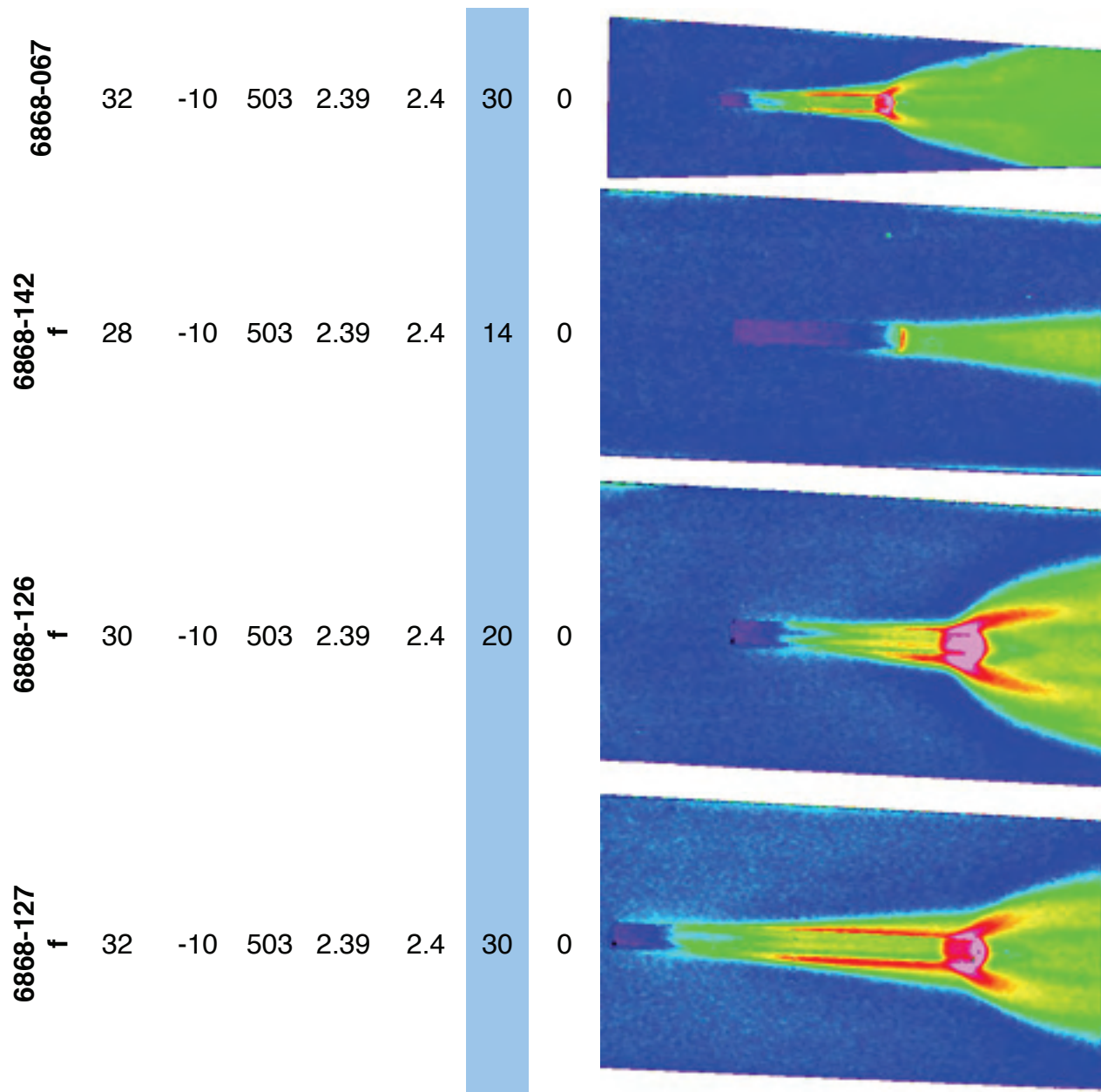


Figure 25.- Depth effect on closed cavity heating for Test 6868 –  $Re_0=503$ ,  $H/\delta=2.39$   
(Concluded).

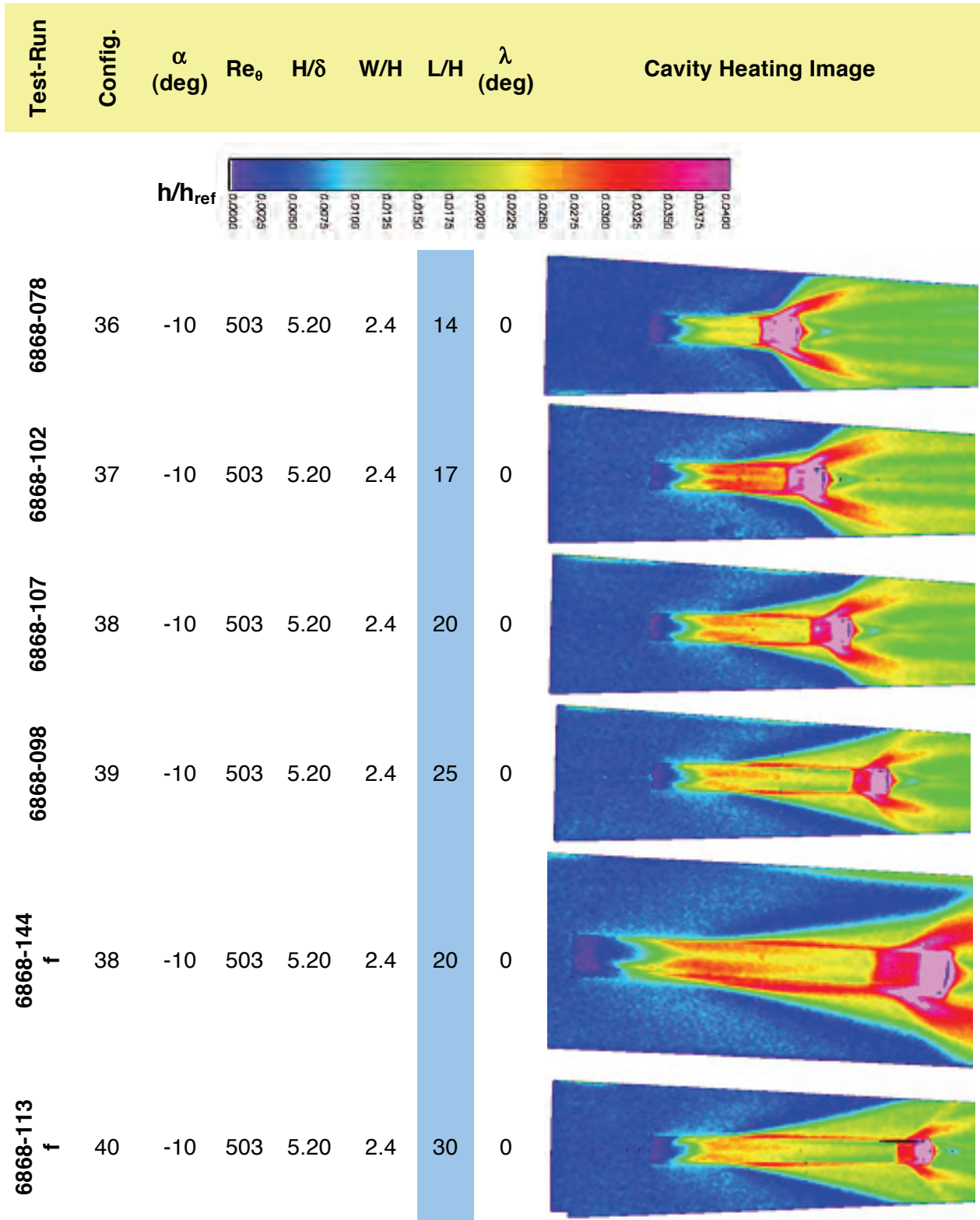


Figure 26.- Depth effect on closed cavity heating for Test 6868 –  $Re_\theta=503$ ,  $H/\delta=5.20$ .

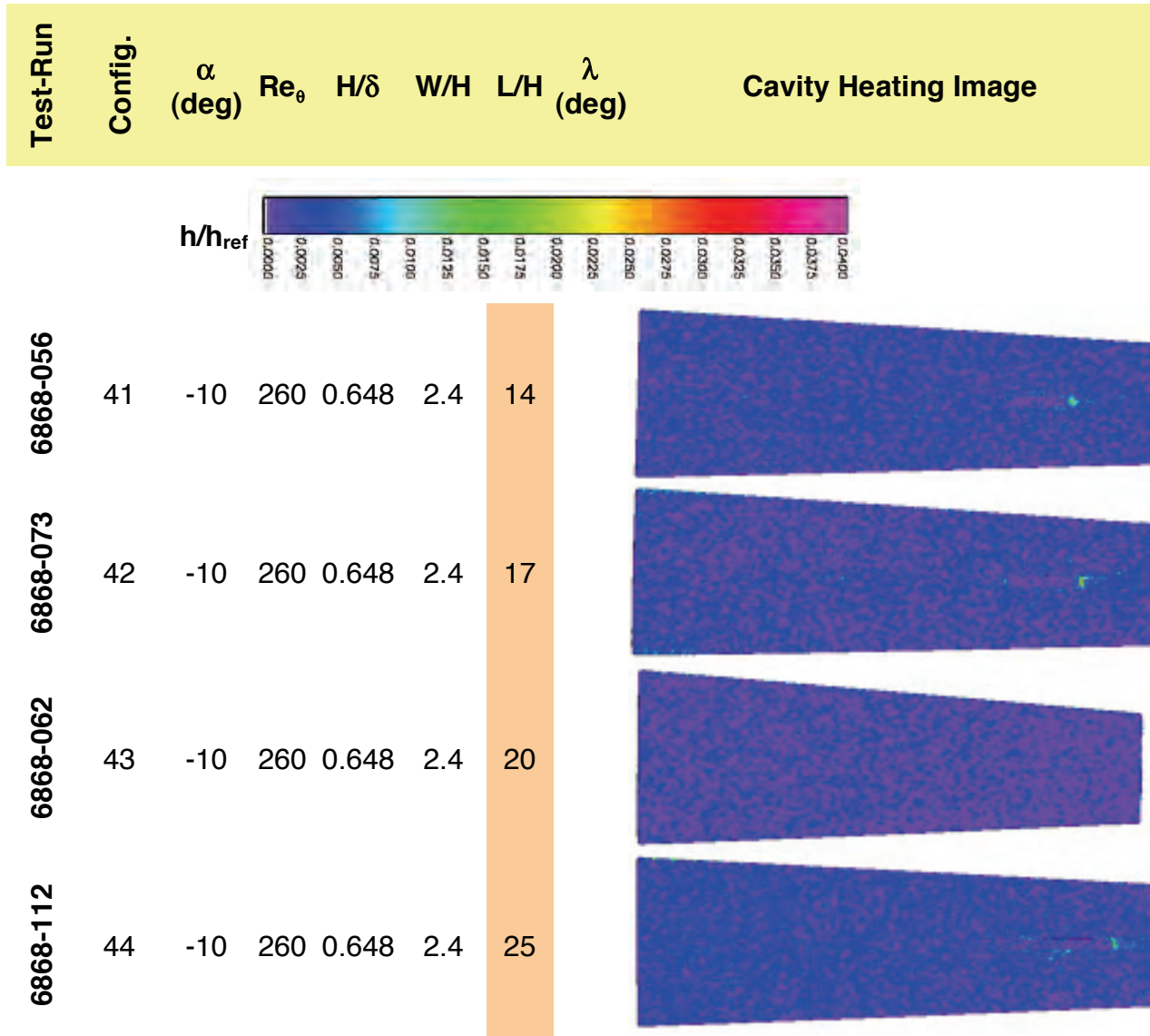


Figure 27- Depth effect on closed cavity heating for Test 6868 –  $Re_\theta=260$ ,  $H/\delta=0.65$ .

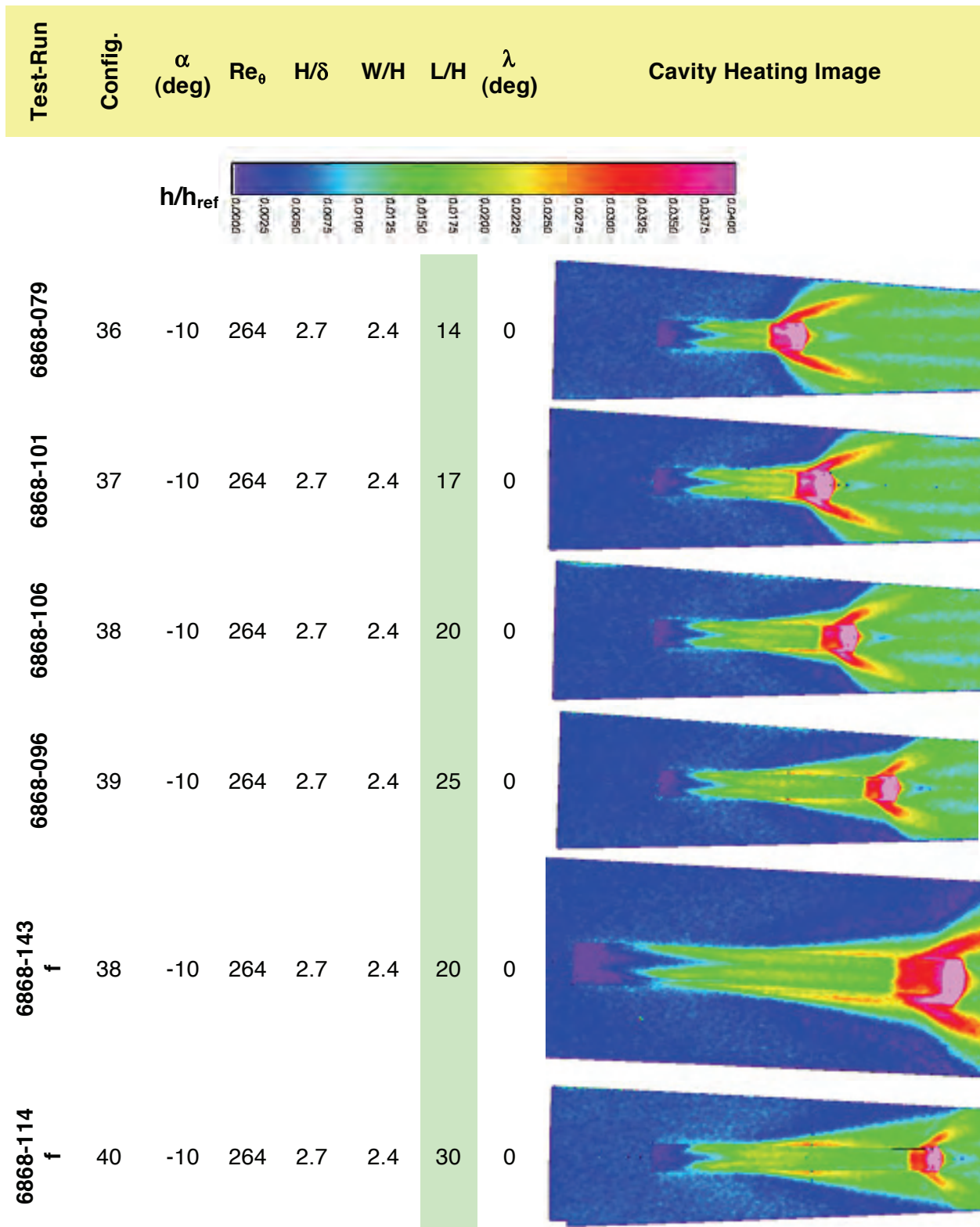


Figure 28.- Depth effect on closed cavity heating for Test 6868 –  $Re_0=260$ ,  $H/\delta=2.7$ .

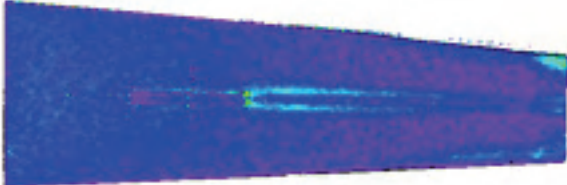
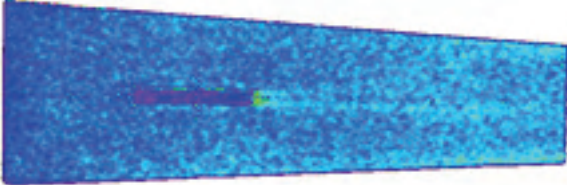
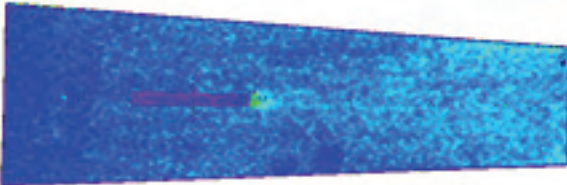
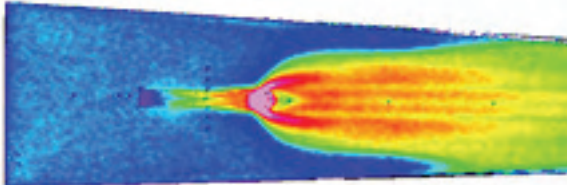
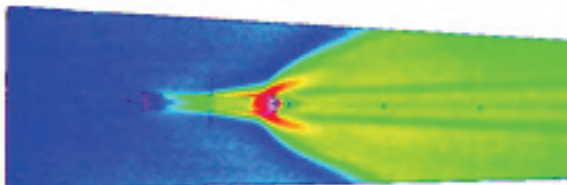
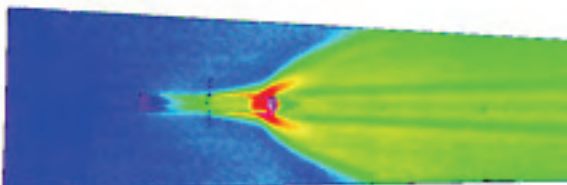
Test-Run	Config.	$\alpha$ (deg)	$Re_\theta$	$H/\delta$	$W/H$	$L/H$	$dp/dx$ ( $ft^{-1}$ )	Cavity Heating Image
6868-035	45 s	0	300	1.1	2.4	20	-0.005	
6868-037	46 s	0	300	1.1	2.4	20	0.005	
6868-045	47 s	0	300	1.1	2.4	20	0.011	
6868-036	45 s	-10	500	2.4	2.4	20	-0.005	
6868-038	46 s	-10	500	2.4	2.4	20	0.005	
6868-046	47 s	-10	500	2.4	2.4	20	0.011	

Figure 29.- Pressure gradient effect on closed cavities for Test 6868.

Test-Run	Config.	$\alpha$ (deg)	$Re_\theta$	$H/\delta$	$W/H$	$L/H$	$\lambda$ (deg)	Cavity Heating Image
6868-117	33 s	0	300	1.1	2.4	20	15	
6868-121	34 s	0	300	1.1	2.4	20	30	
6868-120	35 s	0	300	1.1	2.4	20	45	
6868-135 f	33 s	0	300	1.1	2.4	20	15	
6868-136 f	34 s	0	300	1.1	2.4	20	30	
6868-139 f	35 s	0	300	1.1	2.4	20	45	

Figure 30.- Cross flow effect on closed cavities for Test 6868 –  $Re_\theta=300$ ,  $H/\delta=1.1$ .

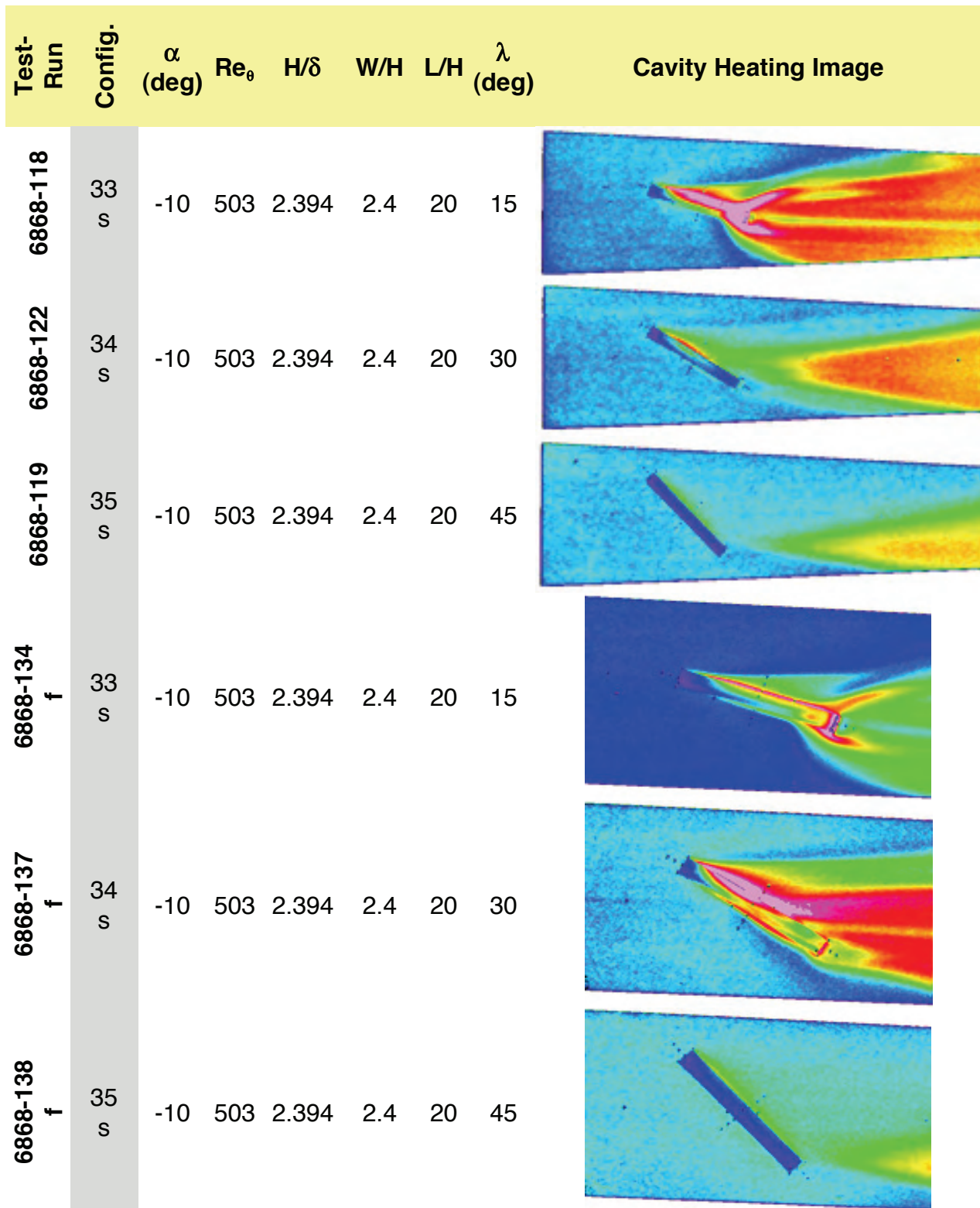


Figure 31.- Cross flow effect on closed cavities for Test 6868 –  $Re_0=500$ ,  $H/\delta=2.39$ .

## Appendix: Derivation of Pressure Gradient Surface Geometry

An inviscid approximation for a constant pressure gradient surface can be obtained using Modified Newtonian Theory (Anderson, 1989). Accordingly,

$$c_p = c_{p,\max} \sin^2 \theta$$

where for  $M \rightarrow \infty$

$$c_{p,\max} \rightarrow \left[ \frac{(\gamma+1)^2}{4\gamma} \right] \left[ \frac{4}{\gamma+1} \right]$$

For  $\gamma=1.4$ ,  $c_{p,\max} \rightarrow 1.839$ . Assuming small surface deflections, it follows that

$$c_p \approx c_{p,\max} \theta^2 = c_{p,\max} \left( \frac{dy}{dx} \right)^2$$

For a constant surface pressure gradient

$$\frac{d}{dx} \left( \frac{c_p}{c_{p,\max}} \right) = \frac{d}{dx} \left( \frac{dy}{dx} \right)^2 = a_0$$

Integration from  $x_0$  to  $x$  yields

$$y = \pm \left( \frac{2}{3a_0} \right) \left[ (a_0 x)^{3/2} \right]$$

after applying the boundary conditions  $y=y_0=0$  and  $(dy/dx)_0=0$  at  $x=x_0=0$ . The constant is given by

$$a_0 = \frac{1}{1.8} \frac{dC_p}{dx}$$

Three gradient surfaces were designed within the allowable constraints imposed by the original model design. The surfaces are described in the Figure A-1, along with the surface contour.



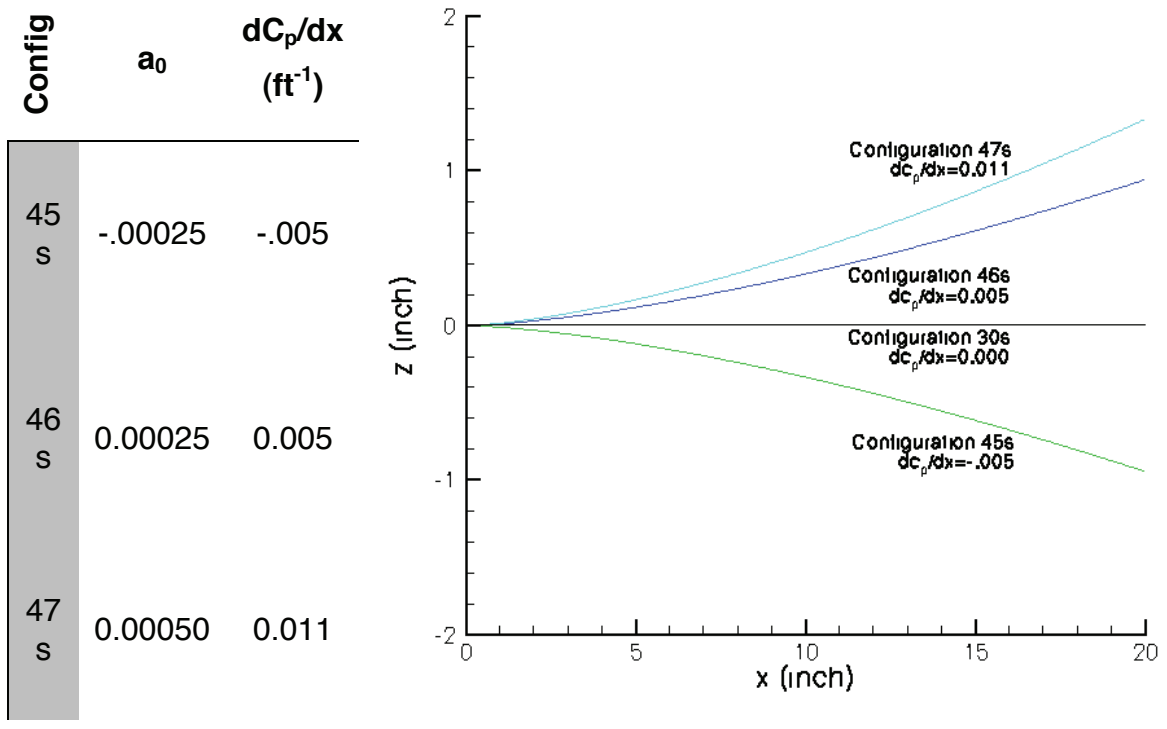


Figure A-1.- Pressure gradient surface definition.

**REPORT DOCUMENTATION PAGE**

*Form Approved  
OMB No. 0704-0188*

The public reporting burden for this collection of information is estimated to average 1 hour per response, including the time for reviewing instructions, searching existing data sources, gathering and maintaining the data needed, and completing and reviewing the collection of information. Send comments regarding this burden estimate or any other aspect of this collection of information, including suggestions for reducing this burden, to Department of Defense, Washington Headquarters Services, Directorate for Information Operations and Reports (0704-0188), 1215 Jefferson Davis Highway, Suite 1204, Arlington, VA 22202-4302. Respondents should be aware that notwithstanding any other provision of law, no person shall be subject to any penalty for failing to comply with a collection of information if it does not display a currently valid OMB control number.  
**PLEASE DO NOT RETURN YOUR FORM TO THE ABOVE ADDRESS.**

<b>1. REPORT DATE (DD-MM-YYYY)</b> 01-03 - 2011		<b>2. REPORT TYPE</b> Technical Memorandum		<b>3. DATES COVERED (From - To)</b>	
<b>4. TITLE AND SUBTITLE</b> Cavity Heating Experiments Supporting Shuttle Columbia Accident Investigation				<b>5a. CONTRACT NUMBER</b>	
				<b>5b. GRANT NUMBER</b>	
				<b>5c. PROGRAM ELEMENT NUMBER</b>	
<b>6. AUTHOR(S)</b> Everhart, Joel L.; Berger, Karen T.; Bey, Kim S.; Merski, N. Ronald; Wood, William A.				<b>5d. PROJECT NUMBER</b>	
				<b>5e. TASK NUMBER</b>	
				<b>5f. WORK UNIT NUMBER</b> 377816.06.03.03.08	
<b>7. PERFORMING ORGANIZATION NAME(S) AND ADDRESS(ES)</b> NASA Langley Research Center Hampton, VA 23681-2199				<b>8. PERFORMING ORGANIZATION REPORT NUMBER</b>  L-19292	
<b>9. SPONSORING/MONITORING AGENCY NAME(S) AND ADDRESS(ES)</b> National Aeronautics and Space Administration Washington, DC 20546-0001				<b>10. SPONSOR/MONITOR'S ACRONYM(S)</b>  NASA	
				<b>11. SPONSOR/MONITOR'S REPORT NUMBER(S)</b>  NASA/TM-2011-214528	
<b>12. DISTRIBUTION/AVAILABILITY STATEMENT</b> Unclassified - Unlimited Subject Category 34 Availability: NASA CASI (443) 757-5802					
<b>13. SUPPLEMENTARY NOTES</b>					
<b>14. ABSTRACT</b> The two-color thermographic phosphor method has been used to map the local heating augmentation of scaled idealized cavities at conditions simulating the windward surface of the Shuttle Orbiter Columbia during flight STS-107. Two experiments initiated in support of the Columbia Accident Investigation were conducted in the Langley 20-Inch Mach 6 Tunnel. Generally, the first test series evaluated open (length-to-depth less than 10) rectangular cavity geometries proposed as possible damage scenarios resulting from foam and ice impact during launch at several discrete locations on the vehicle windward surface, though some closed (length-to-depth greater than 13) geometries were briefly examined. The second test series was designed to parametrically evaluate heating augmentation in closed rectangular cavities. The tests were conducted under laminar cavity entry conditions over a range of local boundary layer edge-flow parameters typical of re-entry. Cavity design parameters were developed using laminar computational predictions, while the experimental boundary layer state conditions were inferred from the heating measurements. An analysis of the aeroheating caused by cavities allowed exclusion of non-breeching damage from the possible loss scenarios being considered during the investigation.					
<b>15. SUBJECT TERMS</b> Space Shuttle Columbia; Accident Investigation; Cavity; Fluids; Heating; Hypersonic; Phosphor Thermography					
<b>16. SECURITY CLASSIFICATION OF:</b>			<b>17. LIMITATION OF ABSTRACT</b>	<b>18. NUMBER OF PAGES</b>	<b>19a. NAME OF RESPONSIBLE PERSON</b>
<b>a. REPORT</b>	<b>b. ABSTRACT</b>	<b>c. THIS PAGE</b>			STI Help Desk (email: help@sti.nasa.gov)
U	U	U	UU	106	<b>19b. TELEPHONE NUMBER (Include area code)</b> (443) 757-5802